

Mixed Valency in Dinuclear Ruthenium Complexes
Bridged by Tetrazine- and Azo-Cyanamide Ligands

by

Fatemeh Habibagahi

A thesis submitted to the Faculty of Graduate and Postdoctoral
Affairs in partial fulfillment of the requirements for the degree of

Master of Science

in

Chemistry

Carleton University
Ottawa, Ontario

© 2014, Fatemeh Habibagahi

Abstract

The novel [Ru(II),Ru(II)] dinuclear complex $[\{\text{Ru}(\text{bpy})(\text{ttpy})\}_2(\mu\text{-tdpc})][\text{PF}_6]_2$, where ttpy: 4-(tert-butylphenyl)-2,2':6',2''-terpyridine, bpy: 2,2'-bipyridine and tdp²⁻ is 3,6-bis(phenylcyanamido)-1,2,4,5-tetrazine, was synthesized and characterized by elemental analysis, ¹H-NMR, IR and UV-Vis spectroscopies. Analysis of the cyclic voltammetry data combined with spectroelectrochemistry results indicates the [Ru(II),Ru(III)] complex is a weakly coupled Class II system. These results were compared against the properties of the strongly coupled Class II complex, $[\{\text{Ru}(\text{bpy})(\text{trpy})\}_2(\mu\text{-adpc})]^{3+}$, where trpy: 2,2':6',6''-terpyridine and adpc²⁻: 4,4'-azodi(phenylcyanamide). DFT calculations of the free ligands and mixed-valence complexes suggest that metal-metal coupling primarily occurs via the hole-transfer mechanism.

Two dinuclear complexes, $[\{\text{Ru}(\text{bpy})_2\}_2(\mu\text{-adpc})_2]$ and $[\{\text{Ru}(\text{bpy})_2(\text{dmsO})\}_2(\mu\text{-adpc})][\text{PF}_6]_2$ where dmsO: dimethylsulfoxide, were synthesized and characterized by elemental analysis, ¹H-NMR and UV-Vis spectroscopies. Spectroelectrochemistry studies showed delocalized metal-metal mixed-valence Class II description for $[\{\text{Ru}(\text{bpy})_2\}_2(\mu\text{-adpc})_2]^+$. The $[\{\text{Ru}(\text{bpy})_2(\text{dmsO})\}_2(\mu\text{-adpc})][\text{PF}_6]_2$ complex exhibits photo-induced Ru-S to Ru-O and thermal Ru-O to Ru-S linkage isomerism in DMSO solution. DFT calculations suggested the non-innocent behavior of phenylcyanamide ligand in both complexes.

Acknowledgements

First and foremost I would like to express my special appreciation and thanks to my research supervisor, Professor Robert J. Crutchley for his knowledgeable comments, remarks and engagement through this research work.

I would also like to thank my committee members Dr. Tim Patterson, Dr. Sean Barry and Dr. Maria DeRosa.

Financial support by Carleton University and Ontario Graduate Scholarships in Science and Technology (OGSST) is appreciated.

Thanks to the Crutchley's lab members, Diane Jodoin, Mohommad M. R. Choudhuri, Alexander L. Daniels and Logan Lubuk with whom I had enjoyable time. Thanks to Keith Bourque for his help with acquiring NMR data. Thanks to Tony O'Neil for help in instrument lab. Thanks to Jim Logan for his helps on setting the instruments and keeping the computers updated. Thanks to Susaritha Chandrabose, Tanya Rudd, and Peter Mosher for all the help at the Science Stores.

The everlasting encouragement of my dad and memory of my mother made this possible. Special thanks to my lovely sister, Arezoo, and her family for their support.

The greatest thanks and appreciates to my caring husband, Ramin, who I will be grateful forever for his love and support.

Table of Contents

Abstract.....	ii
Table of Contents	iv
List of Tables	viii
List of Figures.....	ix
List of Scheme	xiv
Contribution.....	xv
List of Abbreviations	xvi
Chapter 1: General Introduction	1
1.1 Mixed-valence Complexes	2
1.2 Metal-Metal Coupling	3
1.2.1 Experimental Measurement of Metal-Metal Coupling	6
1.2.2 Theoretical Calculation of Metal-Metal Coupling	7
1.3 Class II/III Identification:	10
1.3.1 Infrared spectroscopy	10
1.3.2 Theoretical calculation	15
1.4 Research strategies	17
Chapter 2: Mixed-valence Properties of a Dinuclear Ruthenium Complex Bridged by Bis(phenylcyanamido)tetrazine	20
2.1 Introduction	20
2.2 Experimental.....	21
2.2.1 Materials.....	21
2.2.2 Anhydrous Hydrazine	22
2.2.3 Synthesis of 3,6-Bis-(4-aminophenyl)-1,2-dihydro-1,2,4,5-tetrazine (1)	22

2.2.4	Synthesis of 3,6-bis(phenylcyanamido)-1,2,4,5-tetrazine·1.35H ₂ O (4)	23
2.2.5	Preparation of Tl _{1.75} tdpc (5)	24
2.2.6	Preparation of [{Ru(tpy)(bpy)} ₂ (μ-tdpc)][PF ₆] ₂ ·1.25H ₂ O (6)	25
2.3	Physical Measurements	26
2.3.1	Electrochemistry	26
2.3.2	Infrared, Electronic Absorption and NMR spectroscopies	26
2.3.3	IR- and UV-Vis-NIR Spectroelectrochemistry	27
2.3.4	Elemental Analyses	28
2.3.5	DFT Calculations	29
2.4	Results and Discussion	29
2.4.1	Synthesis	29
2.4.2	NMR Spectroscopy	33
2.4.3	IR-spectroscopy	37
2.4.4	Electronic Absorption Spectroscopy	40
2.4.5	Electrochemistry	43
2.4.6	Vis-NIR Spectroelectrochemistry	44
2.4.7	IR-spectroelectrochemistry	47
2.4.8	DFT Calculation	48
2.5	Conclusion	50
Chapter 3: Photo-linkage Isomerism in a Dinuclear DMSO Complex		51
3.1	Introduction	51
3.2	Experimental	54
3.2.1	Materials	54
3.2.2	Preparation of 4,4'-Azodianiline	54
3.2.3	Preparation of 4,4'-Azodi(phenylcyanamide), (adpcH ₂) (7)	55

3.2.4	Preparation of Tl_2adpc (8).....	56
3.2.5	Preparation of <i>cis</i> -bis(bipyridine)dichlororuthenium(II), $[Ru(bpy)_2Cl_2]$ (10).....	56
3.2.6	Preparation of $[\{Ru(bpy)_2\}_2(\mu-adpc)_2] \cdot (DMSO) \cdot 3(H_2O)$ (11).....	57
3.2.7	Preparation of $[\{Ru(bpy)_2(dmsO)\}_2(\mu-adpc)] [PF_6]_2 \cdot 3H_2O$ (12).....	57
3.3	Physical Measurements	58
3.3.1	Electrochemistry	58
3.3.2	Infrared, Electronic Absorption and NMR Spectroscopies.....	59
3.3.3	Vis-NIR and IR Spectroelectrochemistry	59
3.3.4	Elemental Analyses:.....	60
3.3.5	DFT Calculations:	60
3.4	Results and Discussions:	60
3.4.1	Synthesis of Ligand.....	60
3.4.2	Synthesis of complexes:.....	63
3.4.3	Infrared Spectroscopy:	64
3.4.4	1H -NMR spectroscopy	66
3.4.5	Electrochemistry	70
3.4.6	Electronic Absorption Spectroscopy.....	71
3.4.7	Vis-NIR Spectroelectrochemistry	73
3.4.8	IR Spectroelectrochemistry.....	75
3.4.9	DFT Calculation of Neutral and Singly Oxidized $[\{Ru(bpy)\}_2(\mu-adpc)_2]$ Complex.....	78
3.5	Results and Discussion of dinuclear $[\{Ru(bpy)_2(dmsO)\}_2(\mu-adpc)] [PF_6]_2$ complex: ...	81
3.5.1	Synthesis	81
3.5.2	Infrared Spectroscopy	82
3.5.3	1H -NMR Spectroscopy.....	83
3.5.4	Electronic Absorption Spectroscopy.....	88

3.5.5	Electrochemistry	90
3.5.6	DFT Calculation.....	91
3.6	Conclusion.....	93
Chapter 4: Conclusion and Future Work		95
4.1	Research Summary	95
4.2	Future Work.....	99
Appendices		101
Appendix A : Techniques.....		101
A.1	Preparation of Ag/ AgCl Reference Electrode	101
A.2	TBAH Preparation	102
Appendix B : NMR Spectra.....		103
B.1	3,6-bis-(4-aminophenyl)-1,2-dihydro-1,2,4,5-tetrazine (1).....	103
B.2	3,5-diamino-4-amino-1,2,4-triazol	104
B.3	H ₂ tdpc (4).....	105
B.4	[{Ru(tpy)(bpy)} ₂ (μ-tdpc)][PF ₆] ₂ (6).....	106
B.5	[{Ru(bpy) ₂ Cl ₂ }] (10).....	107
B.6	[{Ru(bpy) ₂ } ₂ (μ-adpc) ₂] (11).....	108
References:.....		109

List of Tables

Table 1 ^1H -NMR Chemical Shifts in $\text{DMSO-}d_6$	37
Table 2 Infrared Spectroscopy Data Performed as KBr discs.....	38
Table 3 Quantitative Electronic Absorption Spectral Data	41
Table 4 Cyclic Voltammetry Data for Dinuclear Ruthenium Complexes with tdpc^{2-} and adpc^{2-} Bridging Ligands	44
Table 5 300 MHz ^1H NMR Data in $\text{DMSO-}d_6$	67
Table 6 Electrochemical ^a Results for dianion adpc and its dinuclear ruthenium complex.	71
Table 7 Quantitative Electronic Absorption Spectral Data of Dianion adpc and Its Dinuclear Complexes in DMF	73
Table 8 Infrared Spectroscopy Data (KBr disc).....	82
Table 9 300 MHz ^1H NMR Data of $[\{\text{Ru}(\text{bpy})_2(\text{S-dms})\}_2(\mu\text{-adpc})][\text{PF}_6]_2$ in $\text{DMSO-}d_6$	84

List of Figures

Figure 1 Potential energy diagram for Class I (dash lines in both A and B), Class II (A) and Class III (B).....	3
Figure 2 Donor-acceptor interaction between donor solvent and ammine group.....	6
Figure 3 Different cyanamide resonance structures based on the ruthenium oxidation state.	11
Figure 4 Reduction of [III, III] complex, [$\{\text{Ru}(\text{NH}_3)_5\}_2(\mu\text{-Me}_2\text{dicyd})\][\text{PF}_6]_4$, to (A) mixed-valence [II, III] and (B) [II, II] in DMSO. ¹²	12
Figure 5 IR spectra representing reduction of [III, III] complex, [$\{\text{Ru}(\text{NH}_3)_5\}_2(\mu\text{-Me}_2\text{dicyd})\][\text{PF}_6]_4$, to [II, III] in acetonitrile. ¹²	13
Figure 6 IR-spectra showing the reduction of [III,III], [$\{\text{Ru}(\text{NH}_3)_5\}_2(\mu\text{-Me}_2\text{dicyd})\][\text{PF}_6]_4$ to (A) mixed-valence [II $\frac{1}{2}$, II $\frac{1}{2}$] and (B) [II,II] complex in Nitromethane. ¹²	14
Figure 7 calculated spin density for [$\text{Ru}(\text{Tp})(\text{dppe})(3\text{-Clpcyd})\]^+$ complex. ²⁶	16
Figure 8 spin density distribution of [$\{\text{Ru}(\text{NH}_3)_5\}_2(\mu\text{-dicyd})\]^3+$ (A) in vacuum, (B) in dielectric continuum and (C) with explicit electrostatic interactions. Green surfaces represent area with positive spin densities and yellow color is used for negative ones. The numbers in % show the atomic spin densities on each ruthenium centres. ²⁹	17
Figure 9 Structures of aromatic di(phenylcyanamide) dianion ligands, adpc ²⁻ : 4,4'-azodi(phenylcyanamide) dianion and tdpc ²⁻ : novel 3,6-bis(phenylcyanamido)-1,2,4,5-tetrazine dianion.....	18
Figure 10 OTTLE cell used for spectroelectrochemistry studies.	28

Figure 11 $^1\text{H-NMR}$ spectrum of 3,6-bis-(4-aminophenyl)-1,2-dihydro-1,2,4,5-tetrazine in DMSO- d_6 .	34
Figure 12 $^1\text{H-NMR}$ spectrum of 3,5-diamino-4-amino-1,2,4-triazol in DMSO- d_6 .	34
Figure 13 $^1\text{H-NMR}$ spectrum of H_2tdpc in DMSO- d_6 .	35
Figure 14 $^{13}\text{C-NMR}$ spectrum of H_2tdpc in DMSO- d_6 .	35
Figure 15 $^1\text{H-NMR}$ spectrum of $\text{Tl}_{1.75}\text{tdpc}$ in DMSO- d_6 . (Peaks at 7.2 and 8.4 ppm are due to impurities of protonated H_2tdpc).	36
Figure 16 $^1\text{H-NMR}$ spectrum of $[\{\text{Ru}(\text{tpy})(\text{bpy})\}_2(\mu\text{-tdpc})][\text{PF}_6]_2$ in DMSO- d_6 .	36
Figure 17 IR spectrum of H_2tdpc KBr pellet.	38
Figure 18 IR spectrum of $\text{Tl}_{1.75}\text{tdpc}$ KBr pellet.	39
Figure 19 IR spectrum of $[\{\text{Ru}(\text{tpy})(\text{bpy})\}_2(\mu\text{-tdpc})][\text{PF}_6]_2$ KBr pellet.	39
Figure 20 Electronic absorption spectrum of H_2tdpc (4) in acetonitrile.	41
Figure 21 Electronic absorption spectrum of H_2tdpc (4) in DMF.	42
Figure 22 Electronic absorption spectrum of $\text{Tl}_{1.75}\text{tdpc}$ (5) in DMF.	42
Figure 23 Electronic absorption spectrum of $[\{\text{Ru}(\text{tpy})(\text{bpy})\}_2(\mu\text{-tdpc})][\text{PF}_6]_2$ (6) in DMF.	43
Figure 24 Cyclic voltammogram of $[\{\text{Ru}(\text{tpy})(\text{bpy})\}_2(\mu\text{-tdpc})][\text{PF}_6]_2$ in DMF with 0.1 M tetrabutylammonium hexafluorophosphate, using platinum counter and working electrode, silver wire pseudo-reference (cobaltocene internal reference, $E^\circ = -0.589$ V versus NHE) at scan rate of 100mV/s.	44
Figure 25 Vis-NIR spectroelectrochemistry of $[\{\text{Ru}(\text{tpy})(\text{bpy})\}_2(\mu\text{-tdpc})][\text{PF}_6]_2$ (6) in DMF solution, 0.1 M TBAH. a) oxidation forming $[\{\text{Ru}(\text{tpy})(\text{bpy})\}_2(\mu\text{-tdpc})]^{3+}$ and b) partial oxidation to form $[\{\text{Ru}(\text{tpy})(\text{bpy})\}_2(\mu\text{-tdpc})]^{4+}$.	46

Figure 26 IR spectroelectrochemistry of [$\{\text{Ru}(\text{ttpy})(\text{bpy})\}_2(\mu\text{-tdpc})\][\text{PF}_6]_2$ (6) in DMF solution, 0.1 M TBAH showing oxidation to [$\{\text{Ru}(\text{ttpy})(\text{bpy})\}_2(\mu\text{-tdpc})\]^{3+}$	47
Figure 27 DFT calculated frontier molecular orbitals and energies of adpc^{2-} (8) and tdpc^{2-} (5).	49
Figure 28 Spin density distribution of [$\{\text{Ru}(\text{ttpy})(\text{bpy})\}_2(\mu\text{-tdpc})\]^{3+}$ (6).	49
Figure 29 Electrochemically induced linkage isomerism in Ru-sulfoxide complexes. ⁴⁶	51
Figure 30 Photo-induced linkage isomerism in ruthenium-sulfoxide complexes.	52
Figure 31 IR spectrum of adpcH_2 (7) (KBr disc).	64
Figure 32 IR spectrum of Tl_2adpc (8) salt (KBr disc).	65
Figure 33 IR spectrum of [$\{\text{Ru}(\text{bpy})_2\}_2(\mu\text{-adpc})_2$] (11) complex (KBr disc).	65
Figure 34 $^1\text{H-NMR}$ of 4,4'-azodianiline in DMSO-d_6	67
Figure 35 $^1\text{H-NMR}$ of adpcH_2 (7) in DMSO-d_6	68
Figure 36 $^1\text{H-NMR}$ of Tl_2adpc (8) in DMSO-d_6	68
Figure 37 $^1\text{H-NMR}$ of $\text{cis-}[\text{Ru}(\text{bpy})_2\text{Cl}_2]$ (10) in DMSO-d_6	69
Figure 38 $^1\text{H-NMR}$ of [$\{\text{Ru}(\text{bpy})_2\}_2(\mu\text{-adpc})_2$] (11) in DMSO-d_6	69
Figure 39 Cyclic voltammogram [$\{\text{Ru}(\text{bpy})_2\}_2(\mu\text{-adpc})_2$] in DMF with 0.1 M tetrabutylammonium hexafluorophosphate, using platinum counter and working electrode, silver wire pseudo-reference (cobaltocene internal reference, Cc/Cc^+) at scan rate of 100mV/s vs. NHE.	71
Figure 40 Electronic absorption spectrum of Tl_2adpc (8) in DMF.	72
Figure 41 Electronic absorption spectrum of [$\{\text{Ru}(\text{bpy})_2\}_2(\mu\text{-adpc})_2$] (11) in DMF.	72
Figure 42 OTTLE cell electronic spectra of [$\{\text{Ru}(\text{bpy})\}_2(\mu\text{-adpc})_2$] in DMF under increasing oxidation potentials (0.0 \rightarrow 0.65 V). 0.1 M TBAH; ITO (indium-tin oxide)	

coated glass served as working and counter electrodes; Ag/AgCl reference electrode(A)0.0 - 0.50 V; (B) 0.5-0.55 V; (C) 0.55-0.65 V.....	74
Figure 43 Metal-metal charge transfer band of [$\{\text{Ru}(\text{bpy})\}_2(\mu\text{-adpc})_2$] in DMF, smoothed data.	75
Figure 44 IR spectroelectrochemical oxidation of [$\{\text{Ru}(\text{bpy})\}_2(\mu\text{-adpc})_2$] to form [$\{\text{Ru}(\text{bpy})\}_2(\mu\text{-adpc})_2$] ⁺ and [$\{\text{Ru}(\text{bpy})\}_2(\mu\text{-adpc})_2$] ²⁺ in DMF, 0.1 M TBAH. 0.0 - 0.85 V vs. Ag / AgCl.....	77
Figure 45 DFT calculation of orbital energies and selected molecular orbitals of [$\{\text{Ru}(\text{bpy})\}_2(\mu\text{-adpc})_2$] (11).....	79
Figure 46 Spin density distribution of [$\{\text{Ru}(\text{bpy})_2\}_2(\mu\text{-adpc})_2$] ⁺	80
Figure 47 Spin density distribution of [$\{\text{Ru}(\text{tpy})(\text{bpy})\}_2(\mu\text{-adpc})$] ³⁺ . ⁵¹	80
Figure 48 IR spectrum of [$\{\text{Ru}(\text{bpy})_2(\text{S-dmsO})\}_2(\mu\text{-adpc})$][PF ₆] ₂ complex(KBr disc). ..	83
Figure 49 IR spectrum of [$\{\text{Ru}(\text{bpy})_2(\text{O-dmsO})\}_2(\mu\text{-adpc})$][PF ₆] ₂ complex(KBr disc)...	83
Figure 50 The numbering scheme used to assign the proton chemical shifts.	84
Figure 51 ¹ H-NMR of [$\{\text{Ru}(\text{bpy})_2(\text{S-dmsO})\}_2(\mu\text{-adpc})$][PF ₆] ₂ (12) in DMSO-d ₆ , two inset figures are the peaks for methyl groups of dmsO ligand.	85
Figure 52 ¹ H NMR spectra of [$\{\text{Ru}(\text{bpy})_2(\text{S-dmsO})\}_2(\mu\text{-adpc})$][PF ₆] ₂ complex in dmsO-d ₆ , initial S-isomer.	86
Figure 53 ¹ H NMR spectra of [$\{\text{Ru}(\text{bpy})_2(\text{dmsO})\}_2(\mu\text{-adpc})$][PF ₆] ₂ complex in dmsO-d ₆ , after 1 hour irradiation.	87
Figure 54 ¹ H NMR spectra of [$\{\text{Ru}(\text{bpy})_2(\text{dmsO})\}_2(\mu\text{-adpc})$][PF ₆] ₂ complex in dmsO-d ₆ , after 2 hours irradiation.....	87
Figure 55 Electronic absorption spectrum of [$\{\text{Ru}(\text{bpy})_2(\text{S-dmsO})\}_2(\mu\text{-adpc})$][PF ₆] ₂	88

Figure 56 Photo-induced S→O isomerization of $[\{\text{Ru}(\text{bpy})_2(\text{dms})\}_2(\mu\text{-adpc})]^{2+}$ in DMSO solution.	89
Figure 57 Thermal relaxation of photo-induced S → O isomer of $[\{\text{Ru}(\text{bpy})_2(\text{dms})\}_2(\mu\text{-adpc})]^{2+}$	90
Figure 58 Cyclic voltammogram $[\{\text{Ru}(\text{bpy})_2(\text{dms})\}_2(\mu\text{-adpc})][\text{PF}_6]_2$ in DMSO with 0.1 M tetrabutylammonium hexafluorophosphate, using platinum counter and working electrode, silver wire pseudo-reference (cobaltocene internal reference, $E^\circ = -0.589$ V versus NHE) at scan rate of 100mV/s.	91
Figure 59 DFT calculation of orbital energies and selected molecular orbitals of $[\{\text{Ru}(\text{bpy})_2(\text{dms})\}_2(\mu\text{-adpc})][\text{PF}_6]_2$ (12).	92
Figure 60 Spin density distribution of $[\{\text{Ru}(\text{bpy})_2(\text{dms})\}_2(\mu\text{-adpc})]^{3+}$ (12).	92
Figure 61 $^1\text{H-NMR}$ spectrum of 3,6-bis-(4-aminophenyl)-1,2-dihydro-1,2,4,5-tetrazine in DMSO- d_6	103
Figure 62 $^1\text{H-NMR}$ spectrum of 3,5-diamino-4-amino-1,2,4-triazol in DMSO- d_6	104
Figure 63 $^1\text{H-NMR}$ spectrum of H_2tdpc in DMSO- d_6	105
Figure 64 $^1\text{H-NMR}$ spectrum of $[\{\text{Ru}(\text{ttpy})(\text{bpy})\}_2(\mu\text{-tdpc})][\text{PF}_6]_2$ in DMSO- d_6	106
Figure 65 $^1\text{H-NMR}$ of $\text{cis-}[\text{Ru}(\text{bpy})_2\text{Cl}_2]$ in DMSO- d_6	107
Figure 66 $^1\text{H-NMR}$ of $[\{\text{Ru}(\text{bpy})_2\}_2(\mu\text{-adpc})_2]$ in DMSO- d_6	108

List of Scheme

Scheme 1 Hole- (Orange) and Electron- (Blue) Transfer Superexchange Mechanism	4
Scheme 2 Synthesis of 3,5-Diamino-4-amino-1,2,4-triazol and 3,6-Bis-(4-aminophenyl)- 1,2-dihydro-1,2,4,5-tetrazine.	30
Scheme 3 Proposed Mechanism of 1,2-Dihydotetrazine to 4-Aminotriazol Recycling by Bentiss et al. ³³	31
Scheme 4 Synthesis Procedure of H ₂ tdpc.	32
Scheme 5 Protonated, Monoprotonated and Deprotonated Forms of tdpc Ligand.	40
Scheme 6 Synthesis of 4,4'-Azodianiline.....	61
Scheme 7 Preparation of 4,4'-Azodiphenylcyanamide (7).....	62

Contribution

Results from Chapter 2 have been published. “Mixed-Valence Properties of a Dinuclear Ruthenium Complex Bridged by Bis(phenylcyanamido)tetrazine. Fatemeh Habibagahi, Robert J. Crutchley. *Can. J. Chem.* **2014**, 92 (11) 1081–1085”

List of Abbreviations

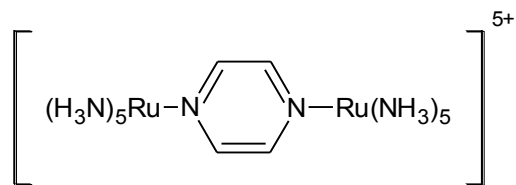
ΔG_c	Free energy of comproportionation
adpc ²⁻	4,4'-azodi(phenylcyanamide)
azodicyd	4,4'-azodi(phenylcyanamide)
B3LYP	Beck three parameter hybrid exchange and Lee-Yang-Parr correlation functionals
bpy	2,2'-bipyridine
Co	Cobaltocene
COSY	Correlated spectroscopy
CNS	Creutz, Newton and Sutin
CV	Cyclic voltammetry
dicyd ²⁻	1,4-dicyanamide benzene dianion
DFT	Density functional theory
DMF	<i>N,N'</i> -dimethylformamide
DMSO	Dimethylsulfoxide
EPR	Electron Paramagnetic Resonance
E_{op}	LMCT band energy
E_{IT} (or λ)	Energy of the intervalence transition
f	Oscillator strength
Fc	Ferrocene
$H_{MM'}$	Metal-metal coupling element
$H_{LM'}$	Metal-ligand coupling element
H_{ad}	Acceptor-donor coupling element (Hush model)
$H_{MM'}$	Metal-metal coupling element (CNS model)
HOMO	Highest occupied molecular orbital
IR	Infra-red

IT	Intervallence transition
IVCT	Intervallence charge transfer
K_c	Comproportionation constant
k_{SO}	Redox-induced S→O isomerization rate
k_{OS1}	Thermal O→S back reaction rate
k_{OS2}	Redox-induced O→S back reaction rate
LMCT	Ligand-to-metal charge transfer
LUMO	Lowest unoccupied molecular orbital
MLCT	Metal-to-ligand charge transfer
MMCT	Metal-to-metal charge transfer
NHE	Normal hydrogen electrode
NIR	Near-infrared
NMR	Nuclear magnetic resonance
OTTLE	Optically transparent thin layer electrode
pcyd ⁻	Phenylcyanamide
Py	Pyridine
Pz	Pyrazine
SOMO	Singly occupied molecular orbital
TBAH	Tetrabutylammonium hexafluorophosphate
tdpc ²⁻	3,6-bis-(4-phenylcyanamide)-1,2,4,5-tetrazine
tpy	2,2':6',2''-terpyridine
ttpy	4-(<i>tert</i> -butylphenyl)-2,2':6',2''-terpyridine
vis-NIR	Visible-Near-infrared
λ_{outer}	Outer-sphere reorganizational energy

Chapter 1: General Introduction

Researchers around the world are attempting to synthesize single molecules which operate as electronic devices to improve the speed of information processing and communications as well as decreasing the size of devices.¹ Possible molecular devices are those with flexible structures that can reversibly change between two or more stable states. These devices can be used to control electricity (molecular electronic switches),^{1,2} to control light (molecular photonic devices), to think and calculate (molecular computers), to transmit signals in desired directions and also in biological systems such as ion channels for signal transduction and so on.¹ Other molecular devices can be based on electro-chromic materials which can be organic, inorganic, polymeric and also mixed-valence complexes. In response to a changing electric field, these compounds change their absorption of electromagnetic radiation (their color changes) and have been used as switchable windows and mirrors, electromagnetic shutters and so on.³

Conductor or semi-conductor molecules have been used as molecular switches. Building blocks of these devices are molecules with both oxidizing and reducing moieties such as mixed-valence complexes or complexes of redox active metals with non-innocent ligands. These complexes are capable of long-range intramolecular electron transfer.⁴ The archetypical example is the Creutz-Taube ion,



whose mixed-valence properties have been extensively examined using a comprehensive range of physical methods.

1.1 Mixed-valence Complexes

According to Robin and Day's classification, mixed-valence complexes are divided into three different groups depending on the degree of coupling (the magnitude/ extent of delocalization) between metal centres.⁴ For Class I complexes, there is no coupling between metal centres and the properties of the complexes are the same as individual metal centres. For Class II complexes, coupling between metal centres are weak and the properties of the metal centres are mixed. Importantly, Class II complexes possess an intervalence absorption band. This is a charge-transfer electronic transition from the donor-metal centre to the acceptor-metal centre. For Class III complexes the coupling is extremely large and because of this, there is no barrier to thermal electron transfer between metal centres. In this delocalized state the odd electron is shared equally between metal centres and this gives rise to partial oxidation state.^{4,5} A new Class of mixed-valence complexes, Class II-III, has been proposed by Meyer and coworkers⁶. This group of complexes shows both localized and delocalized behaviors.

The degree of metal-metal coupling can be described using potential energy diagrams.⁵ Figure 1 shows the representing parabolas for symmetric mixed-valence M-L-M complex. The left-hand parabolas in both diagrams *A* and *B* represent the potential energy surface for Donor-L-Acceptor and the right-hand ones show Acceptor-L-Donor, where L is the bridging ligand. The metal-metal charge transfer energy is shown as E_{IT} , H represents metal-metal coupling element, ΔG_r is a measure of

metal-metal interaction known as the free-energy of resonance exchange and ΔG_{th} is the thermal electron transfer energy barrier.

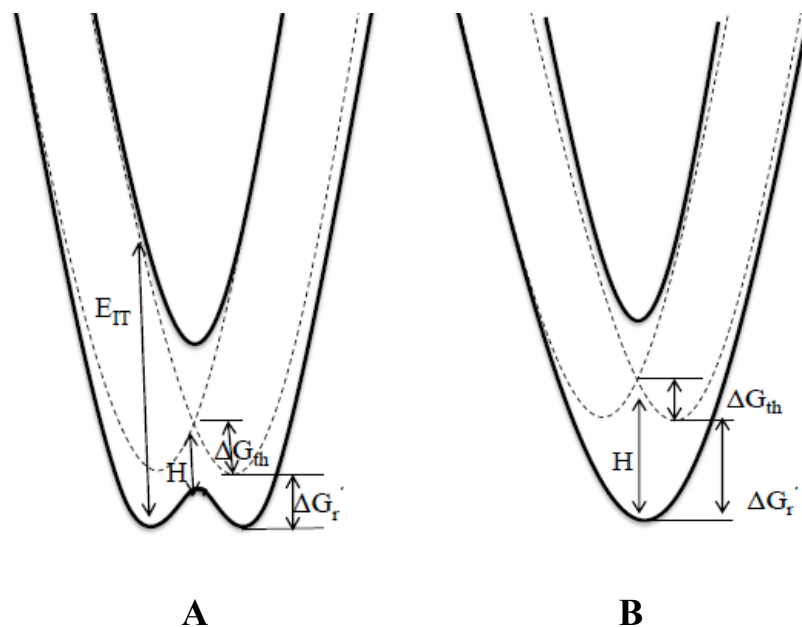


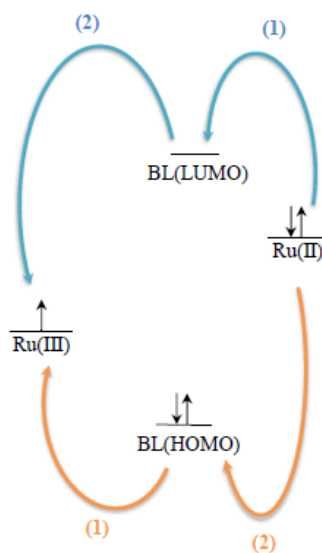
Figure 1 Potential energy diagram for Class I (dash lines in both **A** and **B**), Class II (**A**) and Class III (**B**)

1.2 Metal-Metal Coupling

Metal-metal coupling can occur through direct overlap of metal orbitals or through superexchange.⁷ In superexchange the electron transfer between two metal centers occurs through the bridging ligand's frontier orbitals, highest occupied molecular orbital (HOMO) or the lowest unoccupied molecular orbital (LUMO). Electron transfer via HOMO is known as hole-transfer while the second one is known as electron transfer. As is shown in Scheme 1 for a mixed-valence ruthenium complex the hole transfer pathway involves transfer of an electron from the bridging ligand's HOMO to the acceptor ruthenium centre (Ru(III)) $d\pi$ orbital which follows by an electron transfer from donor ruthenium centre (Ru(II)) to the ligands HOMO. Basically in this method a hole

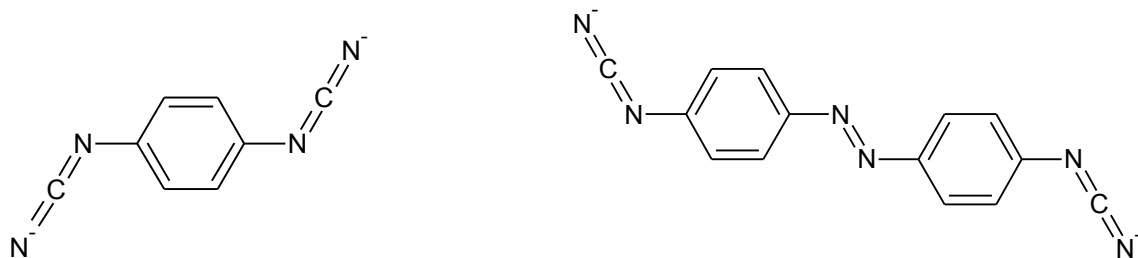
moves from the acceptor to donor orbitals. The electron transfer superexchange pathway is mediated by ligand's LUMO orbital. In a mixed-valence system based on the energy and symmetry match of metal centres with bridging ligand's frontier orbitals one or both of the superexchange pathways can occur.⁸

Scheme 1 Hole- (Orange) and Electron- (Blue) Transfer Superexchange Mechanism



Among different classes of [Ru(II)-Ru(III)] mixed-valence systems are dimers with π -acceptor bridging ligands such as pyrazine.⁴ In this Class of complexes electron transfer superexchange dominates coupling between metal centres. Dimers with π -donor and π -acceptor multidentate bridging ligands such as triazol⁹ anions have been reported to mediate metal-metal coupling via both, hole and electron transfer, pathways.

Studies on different phenylcyanamide ligands such as 1,4-dicyanamidobenzene,¹⁰⁻¹³ 4,4'-azodiphenylcyanamide¹⁴ and their respective derivatives has shown wide range of coupling between metal centres.



These ligands and the substituted variations of them are π -donors. Extension of the π -acceptor wave function of Ru(III) to π -HOMO of these bridging ligands allows superexchange through hole transfer pathway.

The π -interactions between metal centre and bridging ligand in mixed-valence complexes mostly depends on the inner and outer-sphere perturbation of the complex, which is in direct relation with spectator ligands.¹⁵ Previous studies on ruthenium mixed-valence complexes in Crutchley's group has shown replacement of a strong σ -donor ligand such as amine with a weaker σ -donor or even with a π -acceptor ligands such as pyridine and bipyridine stabilizes Ru- $d\pi$ orbitals. This increases the overlap between bridging ligand's π -HOMO and $d\pi$ orbitals of ruthenium which in fact increase the metal-metal coupling via the hole transfer mechanism.¹¹

The interaction of donor solvent molecules with spectator ligands, usually acceptor ones such as ammine, is the other common effective factor on metal-metal coupling which is known as outer-sphere perturbation. According to this interaction the electron density transfers to the ruthenium centre (see Figure 2). The final result of this interaction is a decrease of metal-metal coupling because of destabilization of Ru- $d\pi$ orbital.¹⁶

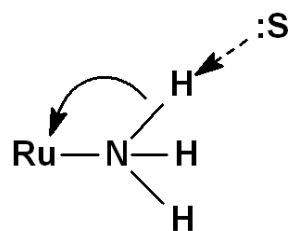
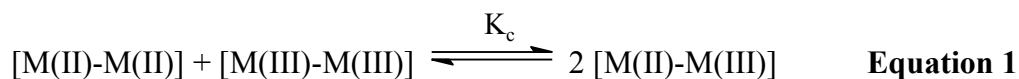


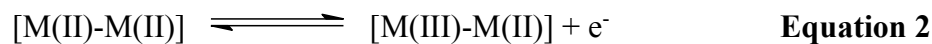
Figure 2 Donor-acceptor interaction between donor solvent and ammine group.

1.2.1 Experimental Measurement of Metal-Metal Coupling

A measure of metal-metal coupling in mixed valence complexes can be obtained experimentally through the comproportionation constant (K_c), which is the equilibrium constant of the following reaction:¹⁷



That is the summation of the reactions in equations 2 and 3.



The value of K_c determined from electrochemistry data for the mixed-valence system as:

$$\Delta G_c = -nF\Delta E = -RT \ln K_c \quad \text{Equation 4}$$

where ΔE is the separation between two redox couple for metal centres, $\Delta E = E_{M2} - E_{M1}$, F is faraday constant, n is the number of electrons in the half reaction, R is the gas constant and T is temperature in Kelvin.

Six different factors,^{11,18,19} shown in equation 5, contribute with ΔG_c :

$$\Delta G_c = \Delta G_s + \Delta G_e + \Delta G_i + \Delta G_{ex} + \Delta G_r + \Delta G_{IP} \quad \text{Equation 5}$$

As ΔG_s represents the statistical distribution of the comproportionation equilibrium, ΔG_e is used as the electrostatic repulsion factor of the two like charged metal centres, ΔG_i relates to the inductive effect of competing coordination of bridging ligand by the metal centres, ΔG_{ex} is the symbol for antiferromagnetic exchange factor that stabilizes the reactant, ΔG_r is the free energy of resonance exchange (the only representative factor for metal-metal coupling in this equation), and finally ΔG_{IP} represents the ion-pairing effect on the comproportionation constant. In order to measure the free energy of resonance exchange the other 5 factors in the equation 5 must be factored out.

1.2.2 Theoretical Calculation of Metal-Metal Coupling

Two theoretical models have been developed in order to compare the experimental results of metal-metal coupling with, the Hush model²⁰ and Creutz, Newton, and Sutin (CNS) model.²¹ Experiments has shown the Hush model is more useful to demonstrate weakly coupled Class II complexes and the CNS model has been more accurate for demonstration of the strongly coupled Class II mixed-valence systems.

The Hush model uses the information derived from intervalence charge transfer of the complex in Muliken-Hush equation (equation 6) to calculate the coupling between metal centres in a mixed-valence complex.

$$H_{ad} = \frac{2.06 \times 10^{-2}}{r} \left(\epsilon_{\max} \cdot \Delta \nu_{1/2} \cdot E_{IT} \right)^{1/2} \quad \text{Equation 6}$$

In this model coupling factor between two metal centres is shown as H_{ad} for coupling between acceptor-donor centres, r is the distance between these centres which is usually derived from crystallography data of the complex, ϵ_{\max} is the molar absorptivity of at the intervalence band, E_{IT} is the energy of at intervalence band maximum and $\Delta \nu_{1/2}$ is the bandwidth of the intervalence band at half height. Using equation 7 the Hush model can predict the MMCT band width for symmetric systems:

$$\Delta \nu_{1/2} = (2310 \nu_{\max})^{1/2} \quad \text{Equation 7}$$

The CNS model²¹ explains the metal-metal coupling in the strongly coupled mixed-valence systems by using different pathways of superexchange, electron- and hole-transfer. The metal-metal coupling element, as is presented in equation 8, in CNS model is shown by $H_{MM'}$ where M and M' represent the two metal centres (M as the acceptor and M' for the donor centre) in the mixed-valence system:

$$H_{MM'} = \frac{H_{ML} H_{M'L}}{2\Delta E_{ML}^{eff}} + \frac{H_{LM} H_{LM'}}{\Delta E_{LM}^{eff}} \quad \text{Equation 8}$$

The first part in the CNS model (equation 8) counts for electron-transfer pathway as it counts for metals to ligand electronic contributions (H_{ML} and $H_{M'L}$) and the second part is the hole-transfer factor which is based on ligand to metal contributions (H_{LM} and $H_{LM'}$). ΔE_{ML} and ΔE_{LM} are the reduced MLCT and LMCT band energies respectively and may be calculated from:

$$\Delta E_{ML} = \left[0.5 \left(\frac{1}{E_{MLCT}} + \frac{1}{E_{MLCT} - E_{MMCT}} \right) \right]^{-1}$$

$$\Delta E_{LM} = \left[0.5 \left(\frac{1}{E_{LMCT}} + \frac{1}{E_{LMCT} - E_{MMCT}} \right) \right]^{-1}$$

The ligand-metal coupling elements can be calculated from metal-to-ligand or ligand-to-metal charge transfer band properties using

$$H_{ML} \text{ or } H_{LM} = \frac{303(E_{LMCT} \times f)^{1/2}}{r} \quad \text{Equation 9}$$

where E_{LMCT} is the LMCT band energy at ϵ_{max} in cm^{-1} , f is the oscillator strength of the LMCT band and r is the transition dipole moment length in \AA . This equation predicts that the magnitude of ligand-to-metal or metal-to-ligand charge transfer is proportional to the square root of LMCT or MLCT band oscillator strength, respectively.

For phenylcyanamide mixed-valence systems it has been shown that hole-transfer is the dominant pathway of superexchange. Furthermore for ruthenium (II) complexes it is impossible to measure the H_{ML} therefore the first part of the CNS equation will be ignored. To simplify the calculations an assumption can be used as $H_{LM}=H_{LM'}$.¹¹ These will end to the final equation as:

$$H_{MM'} = \frac{H_{LM}^2}{\Delta E_{LM}^{eff}} \quad \text{Equation 10}$$

Therefore calculation of the metal-metal coupling element can be achieved using spectroscopic parameters for ligand-to-metal charge transfer in equation 10.

Using the equation 11 for Class II mixed-valence complexes the metal-metal coupling relates to the free energy of resonance exchange:

$$\Delta G_r' = H^2 / E_{IT} \quad \text{Equation 11}$$

where $H=H_{ad}$ or $H_{MM'}$ used in Hush and CNS models, respectively.

1.3 Class II/III Identification:

1.3.1 Infrared spectroscopy

The fastest rate of electron transfer in mixed-valence complexes occurs in barrierless Class III systems which theoretical studies suggest to be as fast as the nuclear frequency factor (10^{12} - 10^{13} s⁻¹). Therefore one of the most experimentally tractable convenient spectroscopic methods to indicate Class III behavior would be the one with the time scale on the order of 10^{-13} s⁻¹. As the timescale for infrared spectroscopy is 10^{-11} to 10^{-13} this method is an appropriate one.

Understanding of the IR spectroscopy of mixed-valence complexes bridged by phenylcyanamide ligands requires an understanding of the resonance structure of the cyanamide group. The properties of the phenylcyanamide ligands are well-known.^{11,14,22-25} Previous studies on phenylcyanamide ligands have shown planar structure of cyanamide group with phenyl ring which is ideal for the strong π -interaction between them.^{22,24,26-28} The vibrational spectrum of the protonated phenylcyanamide group shows an intense absorption band at 2250 cm⁻¹. Upon deprotonation of the cyanamide group the resonance structures caused by delocalization of electrons on the π -system shifts this peak

to lower frequencies, in the range of 2100 to 2150 cm^{-1} , based on the contributions of the resonance forms. As showed in Figure 3 oxidation state of the metal centre affects this contribution.

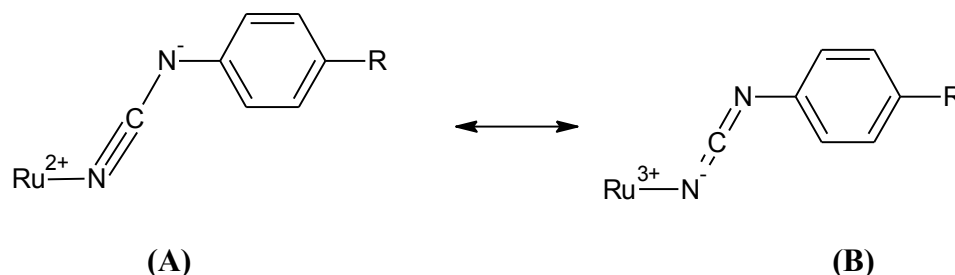


Figure 3 Different cyanamide resonance structures based on the ruthenium oxidation state.

In Ru(II) complexes with this group of ligands strong triple bond between carbon and terminal nitrogen in nitrile group (resonance structure form (A) in Figure 3) results in high energy $\nu(\text{NCN})$ band. As for complexes with Ru(III) metal centres, as showed in part (B) Figure 3, weaker double bond in carbodiimide structure of the cyanamide group shifts the $\nu(\text{NCN})$ vibrational band to lower energies.

To illustrate how IR spectroscopy can be used to distinguish between valence trapped and delocalized states, consider the complex $[\{\text{Ru}(\text{NH}_3)_5\}_2(\mu\text{-Me}_2\text{dicyd})][\text{PF}_6]_4$ where Me_2dicyd is 2,5-dimethyl-1,4-dicyanamidobenzene dianion. Previous studies showed the magnitude of metal-metal coupling in this complex changes in different solvents. Figure 4 to Figure 6 show the IR-Spectra of three different mixed valency state of the complex.¹²

Figure 4 shows the infrared spectroelectrochemistry for systems with little coupling between metal centres, as $[\{\text{Ru}(\text{NH}_3)_5\}_2(\mu\text{-Me}_2\text{dicyd})][\text{PF}_6]_4$ in DMSO. At the

first point the spectrum of the complex consists just one $\nu(\text{NCN})$ vibrational band at 2130 cm^{-1} (Figure 4 part A).

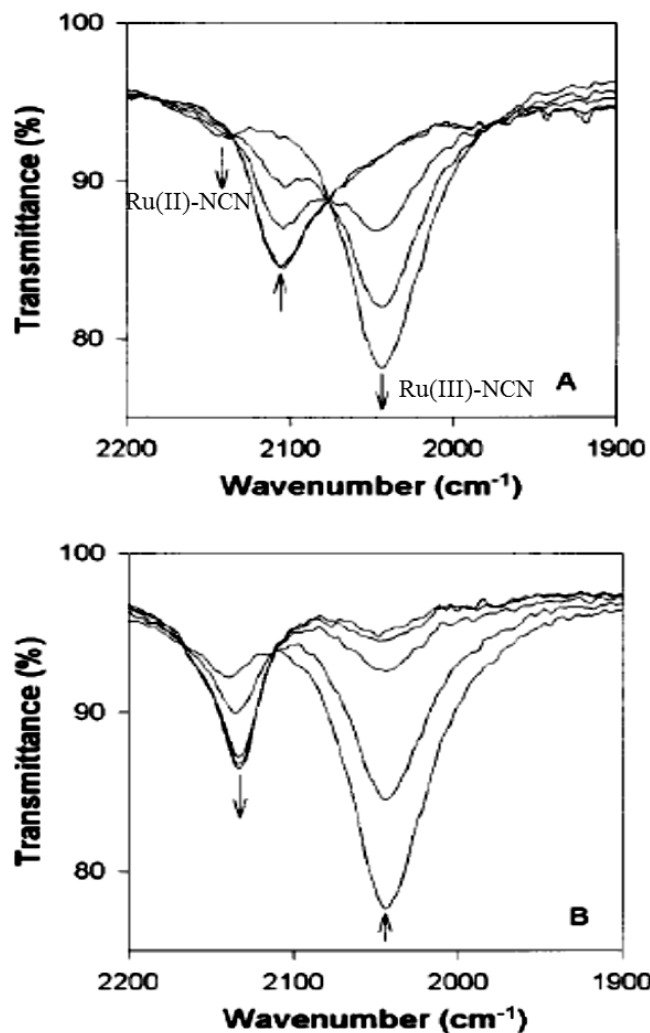


Figure 4 Reduction of [III, III] complex, $[\{\text{Ru}(\text{NH}_3)_5\}_2(\mu\text{-Me}_2\text{dicyd})][\text{PF}_6]_4$, to (A) mixed-valence [II, III] and (B) [II, II] in DMSO.¹²

Upon reduction of the [III,III] system to mixed-valence [II,III] complex (part A Figure 4) two new $\nu(\text{NCN})$ bands will appear, an intense band at lower energies (2040 cm^{-1}) and a weak band at higher energies (2160 cm^{-1}) which is in consistent with one metal centre at

2+ oxidation state and the other one at 3+, respectively (part A in Figure 4). As is seen little coupling between metal centres in the mixed-valence state results in two different $\nu(\text{NCN})$ bands. Further reduction to [II, II] complex results in decrease of the intensity of the band at 2160 cm^{-1} and increase of the intensity of the band at 2040 cm^{-1} which confirms form A resonance structure showed in Figure 3 for the Ru(II)-phenylcyanamide complex.¹²

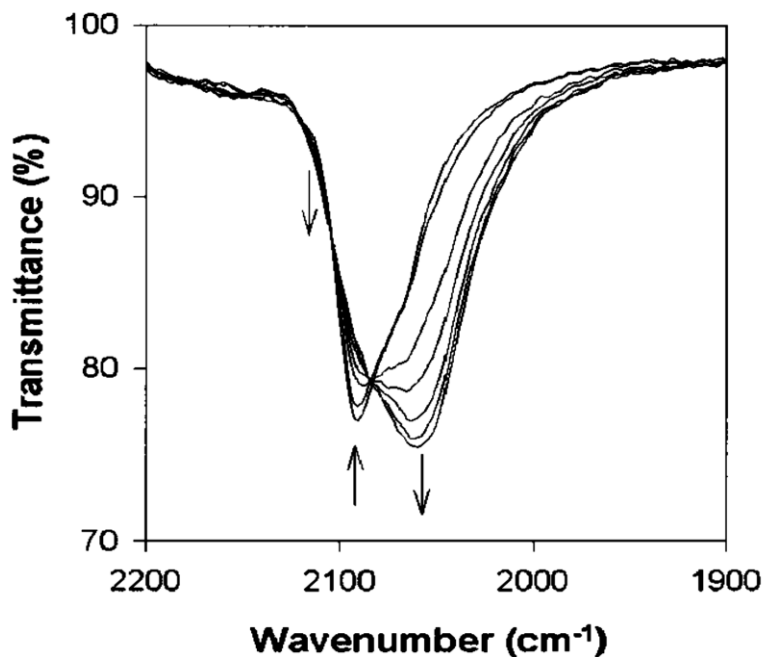


Figure 5 IR spectra representing reduction of [III, III] complex, $[\{\text{Ru}(\text{NH}_3)_5\}_2(\mu\text{-Me}_2\text{dicyd})][\text{PF}_6]_4$, to [II, III] in acetonitrile.¹²

Increase in the coupling degree between metal centres in the mixed-valence system results in the peak broadening. As showed in Figure 5 the initial $\nu(\text{NCN})$ band in the Ru(III,III) complex broadened upon reduction to the mixed-valence Ru(II,III) system in acetonitrile. This broadening coincided with the shift to lower energies (shift from

2100 cm^{-1} to 2060 cm^{-1}). These properties are consistent with the Class II-III (intermediate between localized and delocalized) case.

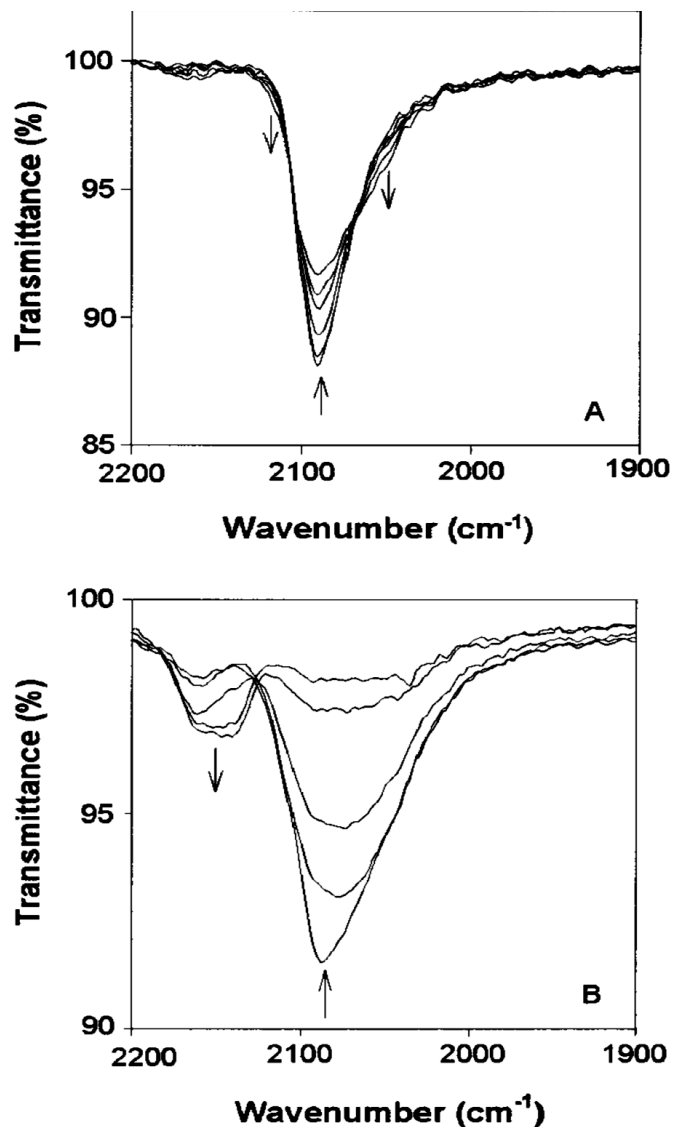


Figure 6 IR-spectra showing the reduction of $[\text{III}, \text{III}]$, $[\{\text{Ru}(\text{NH}_3)_5\}_2(\mu\text{-Me}_2\text{dicyd})][\text{PF}_6]_4$ to (A) mixed-valence $[\text{II}^{1/2}, \text{II}^{1/2}]$ and (B) $[\text{II}, \text{II}]$ complex in Nitromethane.¹²

Infrared spectra of the complex in nitromethane (Figure 6) showed characteristics of Class III mixed-valence systems. Strong coupling between metal centres results in 2.5+ oxidation states for both ruthenium centres. This new oxidation state generates an

equilibrium between two resonance structures showed in Figure 3 therefore just one $\nu(\text{NCN})$ peak would be expected in the infrared spectrum(see Figure 6). This behavior in compare with Class II-III systems (Figure 5) shows reduced broadening and no shift of the $\nu(\text{NCN})$ peak. Further reduction to Ru(II,II) complex results in the shift of $\nu(\text{NCN})$ peak to higher energies arises from Ru(II) bound to cyanamide group (resonance form A in Figure 3).

Studies on ruthenium complexes with phenylcyanamide ligands in Crutchley's group showed strong coupling between metal centres in dicyd²⁻ (1,4-dicyanamidobenzene)¹⁰⁻¹³ and adpc²⁻ (4,4'-azodiphenylcyanamide)¹⁴ complexes.

1.3.2 Theoretical calculation

Quantum mechanical calculation is often used as supporting evidence for experimental results. This method deals with the total charge density and is one of the suitable methods of analyzing the spin density in transition metal complexes.

DFT calculations on a group of $[\text{Ru}(\text{Tp})(\text{dppe})(\text{R-pcyd})]^+$, where dppe = ethylenebis(diphenylphosphine), Tp^- = hydrotris(pyrazol-1-yl)borate, R-pcyd = substituted phenylcyanamide ligands, complexes showed different redox activity of the phenylcyanamide ligands in the mixed-valence state of the complex.²⁶ Data analysis showed relations between the donor strengths of these ligands and their non-innocent behavior, as for the complex with 3-Clpcyd ligand the spin density mostly localized on

the ligand (Figure 7) where for the Cl₅pcyd species localization is predicted mainly metal-centered.

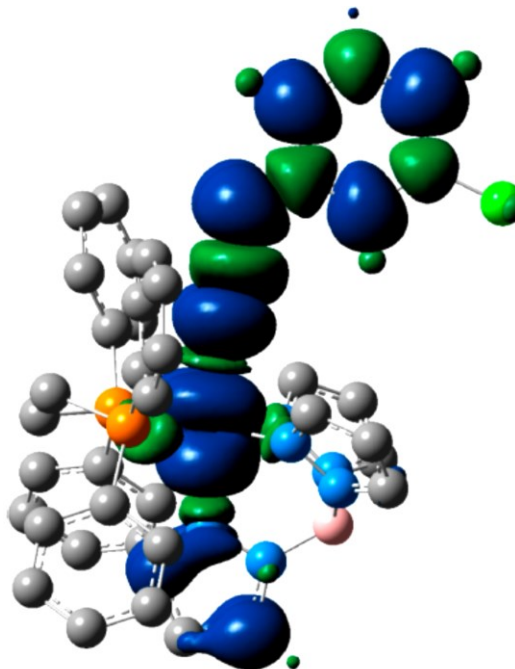


Figure 7 calculated spin density for $[\text{Ru}(\text{Tp})(\text{dppe})(3\text{-Clpcyd})]^+$ complex.²⁶

The accuracy of DFT calculation depends on the nature of the basis set and calculation functions which often requires optimization based on the correlation with experimental results. For instance NMR and EPR studies on $[\text{Ru}(\text{NH}_3)_5(\text{pcyd})]^{2+}$ and $[\{\text{Ru}(\text{NH}_3)_5\}_2(\mu\text{-dicyd})]^{3+}$ complexes showed Ru(III) metal-centered spin density while the DFT calculation suggested spin density mostly on cyanamide ligands. Introducing solvents properties perturbed the spin density slightly (Figure 8) while simulating the polar solvent-solute interactions by using an explicit electrostatic model showed the most effect on the calculated spin density.²⁹

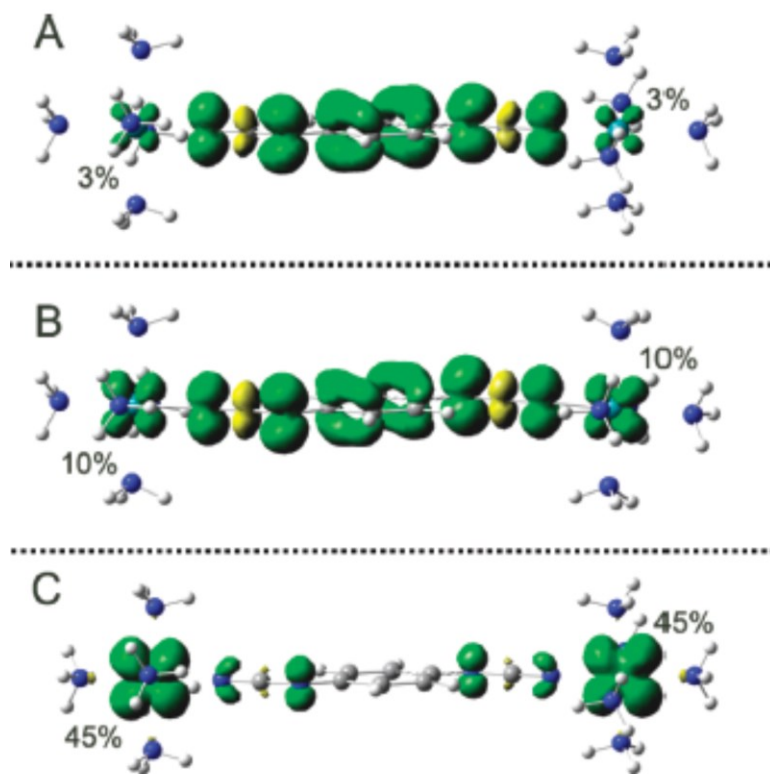


Figure 8 spin density distribution of $[\{\text{Ru}(\text{NH}_3)_5\}_2(\mu\text{-dicyd})]^{3+}$ (A) in vacuum, (B) in dielectric continuum and (C) with explicit electrostatic interactions. Green surfaces represent area with positive spin densities and yellow color is used for negative ones. The numbers in % show the atomic spin densities on each ruthenium centres.²⁹

1.4 Research strategies

For the last 3 decades Crutchley's group has worked on the coordination chemistry of different families of phenylcyanamide complexes. In order to synthesize complexes with the application as molecular devices and switches the electronic nature of the inner- and the outer-sphere of these complexes have been tuned in different ways.

In presence of π -acid metals, dianion phenylcyanamide ligands show σ - and π -donor properties. Based on the oxidation state of the metal centre cyanamide groups will possess one of the structures shown in Figure 3. It has been observed for binding to a

ruthenium (III) metal centre, the cyanamide group possesses mainly resonance form B while for binding to Ru(II) resonance form A is dominant.^{22,28} As has been stated before for mixed-valence systems these differences can be recognized using infrared spectroscopy.

Figure 9 shows the dianion forms of the two different diphenylcyanamide ligands used in this research in order to synthesize three different dinuclear ruthenium complexes.

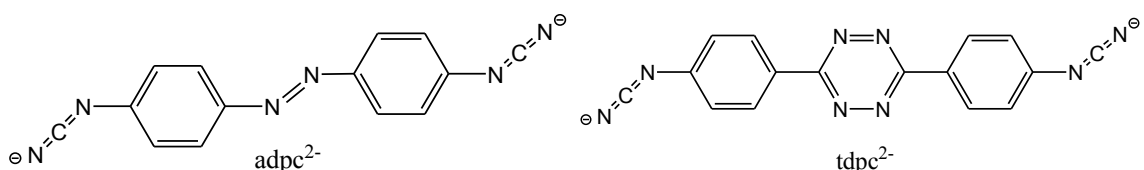


Figure 9 Structures of aromatic di(phenylcyanamide) dianion ligands, adpc²⁻: 4,4'-azodi(phenylcyanamide) dianion and tdpc²⁻: novel 3,6-bis(phenylcyanamido)-1,2,4,5-tetrazine dianion.

Chapter 2 describes the synthesis and characterization of the neutral and anionic form of the novel H₂tdpc bridging ligand and its dinuclear ruthenium complex [$\{\text{Ru}(\text{ttpy})(\text{bpy})\}_2(\mu\text{-tdpc})\][\text{PF}_6]_2$ where ttpy is 4-(tert-butylphenyl)-2,2':6',2''-terpyridine and bpy is 2,2'-bipyridine.³⁰ Investigations on the oxidation and electronic properties of this complex have been done using cyclic voltammetry, IR and UV-Vis spectroelectrochemistry. The results have been compared with analogue cyanamide complex [$\{\text{Ru}(\text{trpy})(\text{bpy})\}_2(\mu\text{-adpc})\][\text{PF}_6]_2$, where trpy is 2,2':6',6''-terpyridine, and the theoretical calculations. In chapter 3 another dinuclear ruthenium complex bridged by adpc²⁻, [$\{\text{Ru}(\text{bpy})\}_2(\mu\text{-adpc})_2$], is synthesized and used as precursor in the synthesis

procedure of $[\{\text{Ru}(\text{bpy})(\text{dmsO})\}_2(\mu\text{-adpc})][\text{PF}_6]_2$. The mixed valency of the precursor complex has been examined using IR and UV-Vis spectroelectrochemistry as well as cyclic voltammetry. The dinuclear $[\{\text{Ru}(\text{bpy})(\text{dmsO})\}_2(\mu\text{-adpc})][\text{PF}_6]_2$ complex has been examined for linkage isomerism of dmsO ligand using UV-Vis spectroscopy and cyclic voltammetry methods.

The chemical structures of the products have been characterized using $^1\text{H-NMR}$, IR and UV-Vis spectroscopies.

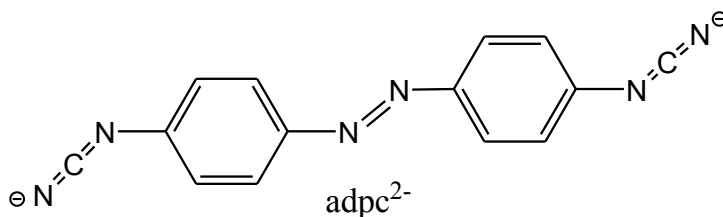
Chapter 2: Mixed-valence Properties of a Dinuclear Ruthenium Complex Bridged by Bis(phenylcyanamido)tetrazine

2.1 Introduction

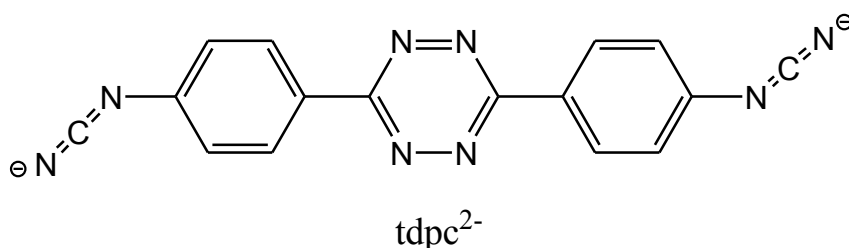
Electronic coupling between two metal centres in mixed-valence complexes alters with the nature of bridging ligand. Different classes of bridging ligands have been previously examined and their effect on metal-metal coupling in mixed-valence complexes have been studied such as π -acid bridging ligands for instance pyrazine and 4,4'-bipyridine.⁴

For ruthenium in 2+ and 3+ oxidation states bound to a π -acid bridging ligand, the electron transfer superexchange arises via lowest unoccupied molecular orbital of the bridging ligand. In Crutchley's group, studies on the anionic π -donors phenylcyanamide bridging ligands such as 1,4-dicyanamidobenzene have showed that metal-metal coupling occurs via hole-transfer superexchange and depends on the coupling of metal $d\pi$ - orbitals with the highest occupied molecular orbital (HOMO) of bridging ligand.¹¹

In earlier studies on phenylcyanamide bridging ligands another class of these ligands had been studied in which the donor phenylcyanamide group is bounded to the acceptor azo group as 4,4'-azo-diphenylcyanamido dianion adpc^{2-} .¹⁴



DFT calculation on this new class of ligands showed HOMO and LUMO are both delocalized over the entire molecule and that they are in close energy match with $d\pi$ donor and acceptor orbitals by which superexchange can occur through electron- and hole-transfer mechanisms. In order to explore more about the effect of acceptor groups of donor-acceptor-donor bridging ligands on the metal-metal coupling, the azo group has been replaced with tetrazine, a stronger acceptor. In the present research the novel 3,6-bis(phenylcyanamido)-1,2,4,5-tetrazine dianion (tdpc^{2-}) bridging ligand has been synthesized and characterized.



Tetrazine is predicted to be a stronger acceptor than the azo group and should have the effect of stabilizing this ligand's HOMO and LUMO. The effect of this perturbation on mixed-valence properties will be explored.

2.2 Experimental

2.2.1 Materials

Glacial acetic acid ($\leq 99.7\%$, ACS reagent grade, Anachemia), ammonium thiocyanate (Sigma-Aldrich), 4-aminobenzonitrile (Sigma-Aldrich), hydrazine hydrate (Sigma-Aldrich), benzoyl chloride (99%, Sigma-Aldrich), triethyl amine (99.5%, Fluka), lead(II) acetate trihydrate (ACS reagent grade, 99+%, Aldrich), thallium (I) acetate ($\geq 99\%$, Sigma-Aldrich) (**Caution: highly toxic! Danger of cumulative effect**),

Ammonium hexafluorophosphate (99.5%, Alfa Aesar), ruthenium trichloride hydrate (99.9%, Alfa Aesar), 2,2'-bipyridine (Reagent plus, $\geq 99\%$, Sigma-Aldrich), dimethyl sulfoxide (anhydrous, $\geq 99.5\%$, Sigma-Aldrich) and dimethylformamide DMF (Caledon) were used as received. The reagent complex, $[\text{Ru}(\text{ttpy})(\text{bpy})(\text{Cl})][\text{PF}_6]$ and 4-(*tert*-butylphenyl)-2,2':6',2''-terpyridine (ttpy) were synthesized as reported previously.¹³

2.2.2 Anhydrous Hydrazine

A literature procedure was followed with modification.³¹ Under argon 50 g of NaOH pellets were ground to a powder and then added to 110 mL of hydrazine monohydrate. The sealed mixture was stirred for 20 h and then filtered under argon. The filtrate was distilled at 70 °C under reduced pressure into two fractions. The first fraction of 20 mL was discarded and the second fraction of 50 mL was used for the next step.

2.2.3 Synthesis of 3,6-Bis-(4-aminophenyl)-1,2-dihydro-1,2,4,5-tetrazine (1)

A literature procedure was followed with modification.³² 2 g of 4-aminobenzonitrile (17 mmol) was dissolved in 10 mL anhydrous hydrazine under argon. The solution was then heated to 100-105 °C with stirring. After 18 h, the reaction mixture was cooled to room temperature, precipitating the yellow product which was filtered off and washed with methanol, water and methanol and allowed to dry under argon. Yield: 0.77 g (34%). ¹H-NMR (300 MHz, DMSO-*d*₆): 5.48 (4H, singlet), 6.53 (4H, doublet), 7.47 (4H, doublet), 8.51 (2H, singlet) ppm in agreement with literature. Mpt: 259-262 °C (lit. Mpt. 261°C).³²

Increase in the temperature (even just with 10 degrees) results in white needle crystals of 3,5-diamino-4-amino-1,2,4-triazol.³³ Yield: 1.9 g (84%) ¹H-NMR (300 MHz, DMSO-d₆): 5.46(4H, singlet), 5.96 (2H, singlet), 6.64 (4H, doublet), 7.67 (4H, doublet) ppm which is in agreement with literature.³³ Mpt: 224-228 (lit. Mpt: 225-227 °C).

2.2.4 Synthesis of 3,6-bis(phenylcyanamido)-1,2,4,5-tetrazine·1.35H₂O (4)

Under argon, ammonium thiocyanate (1.125 g, 15 mmol) was dissolved in 10 mL refluxing acetone. To this gently refluxing solution was added dropwise an acetone solution of benzoylchloride (1.7 mL, 15 mmol in 10 mL of acetone), precipitating ammoniumchloride as the reaction proceeded. After the addition was complete, the reaction mixture was refluxed for a further 15 min under argon. A solution of 3,6-bis(4-aminophenyl)-1,2-dihydro-1,2,4,5-tetrazine (2 g, 7.5 mmol) in 120 mL of hot acetone was then added dropwise to the refluxing reaction mixture and the reaction mixture refluxed for 3 hours. The reaction mixture was poured into 700 mL distilled water with stirring, precipitating the brownish-orange thiourea **2** (Scheme 4) which was filtered and washed with distilled water. Under argon, the still wet **2** was added to 200 mL 2 M NaOH and the mixture boiled for 5 min. The now clear-orange solution was cooled down to 60 °C and 5.6 g (15 mmol) of lead acetate in 20 mL distilled water was added. Black PbS formed immediately and after 5 min of stirring, the PbS was Büchner filtered from the red filtrate which was cooled in a suction flask immersed in an ice/salt bath. Addition of 25 mL glacial acetic acid to the filtrate precipitated the dark-red 3,6-bis(phenylcyanamido)-dihydro-1,2,4,5-tetrazine **3** which was filtered, washed with water and dried under argon. Yield: 2.14 g of crude. The crude **3** was dissolved in a 100 mL

aqueous solution of 6% hydrogen peroxide and heated in an oil bath at 60 °C for 2 hours during which time red H₂tdpc (**4**) precipitated. The crude **4** was dissolved in 800 mL of hot acetone and then filtered from insoluble impurities. The filtrate was evaporated to a red powder which was then recrystallized from 500 mL (2:1) hot acetone : water, affording red dendritic crystals of **4**. Yield: 1.0 g (43%). Anal. Calcd for C₁₆H_{11.7}N₈O_{1.35}: C, 56.75; H, 3.78; N, 33.09. Found: C, 57.11; H, 3.68; N, 32.69. IR: $\nu(\text{NCN})$ 2228 cm⁻¹. ¹H NMR (300 MHz, DMSO-*d*₆): 10.81 (2H, broad singlet), 8.50 (4H, doublet), 7.25 (4H, doublet) ppm. ¹³C NMR (300 MHz): 163, 143.21, 130, 126.48, 116.28, 111.72 ppm. Mpt: 288-291 °C.

2.2.5 Preparation of Tl_{1.75}tdpc (**5**)

To a solution of **4** (0.4 g, 1.27 mmol) in 150 mL of boiling 2 : 1 acetone/water was added thallium acetate (0.7 g, 2.5 mmol) in 50 mL 2 : 1 acetone/water followed by 1.5 mL triethylamine. The reaction mixture was boiled for 5 min and then chilled to -20 °C. Fine black crystals of Tl_{1.75}tdpc formed which were filtered and washed with water and acetone. Yield: 0.47 g, 51%. Anal. Calcd for C₁₆H₈N₈Tl_{1.75}: C, 28.68; H, 1.20; N, 16.73. Found: C, 28.88; H, 1.30; N, 16.44. IR: $\nu(\text{NCN})$ 2124.5 cm⁻¹. ¹H NMR (300 MHz, DMSO-*d*₆): 8.03 (4H, doublet), 6.72 (4H, doublet) ppm. The presence of **4** which co-precipitated with its thallium salt was confirmed by ¹H NMR. The near insolubility of the thallium salt prevented further purification.

2.2.6 Preparation of $\{[\text{Ru}(\text{ttpy})(\text{bpy})]_2(\mu\text{-tdpc})\}[\text{PF}_6]_2 \cdot 1.25\text{H}_2\text{O}$ (6)

$[\text{Ru}(\text{ttpy})(\text{bpy})\text{Cl}][\text{PF}_6]$ (0.33 g, 0.4 mmol) and $\text{Ti}_{1.75}\text{tdpc}$ (0.18 g, 0.25 mmol) were dissolved in 150 mL of DMF under inert atmosphere, and the deep red-purple solution was refluxed for 60 hours. The dark-brown reaction mixture was then chilled to $-20\text{ }^\circ\text{C}$ and filtered using a fine frit and Celite® powder to remove fine white TiCl and unreacted $\text{Ti}_{1.75}\text{tdpc}$. The filtrate was then concentrated to 20 mL by rotary evaporation, and 600 mL diethyl ether was used to precipitate crude product. After cooling the ether solution for an hour at $-20\text{ }^\circ\text{C}$, the product was collected by suction filtration (0.28 g). The crude product was purified by chromatography. In a typical experiment 0.2 g of the crude complex was dissolved in 15 mL of 1:1 acetonitrile/toluene which was filtered and loaded onto a 30 cm x 3 cm chromatography column containing 200 g grade III alumina (Brockmann 1, weakly acidic, 150 mesh). Two bands containing starting material and mononuclear complex were eluted first with 1:1 acetonitrile/toluene. The third band containing desired complex was eluted using 2:1 acetonitrile/ toluene and the eluate evaporated to dryness using rotary evaporation. Recrystallization was achieved by the slow diffusion of diethyl ether into a saturated solution of complex in DMF. Yield: 0.17 g (37%). Anal. Calcd. for $\text{Ru}_2\text{C}_{86}\text{H}_{72.5}\text{O}_{1.25}\text{N}_{18}\text{P}_2\text{F}_{12}$: C, 55.23; H, 3.91; N, 13.48. Found: C, 54.92; H, 3.88; N, 13.46. IR: $\nu(\text{NCN})$ 2176 cm^{-1} . ^1H NMR (300 MHz, DMSO-d_6): 9.68 (d, 2H), 9.25 (s, 4H), 9.00 (dd, 6H), 8.72 (d, 2H), 8.45 (t, 2H), 8.24 (d, 4H), 8.18 (t, 6H), 7.94 – 7.83 (m, 6H), 7.77 (d, 4H), 7.72 (d, 4H), 7.57 (d, 2H), 7.52 – 7.46 (t, 4H), 7.18 (t, 2H), 6.17 (d, 4H) ppm.

2.3 Physical Measurements

2.3.1 Electrochemistry

Cyclic voltammetry studies were performed in DMF solution using a Metrohm Autolab potentiostat/galvanostat PGSTAT30. As electrochemical cell a double jacketed container with an internal volume of 15 mL with Teflon cap to hold three electrodes and argon bubbler was used. Three electrode system containing a platinum disk as working electrode, a platinum wire as auxiliary electrode and a silver/silver chloride wire as quasi-reference electrode was used. All electrodes were cleaned manually and polished with 1- μ m diamond polish after and before each set of scans. 0.1 M solution of TBAH was used as supporting electrolyte. Argon gas was used to degas the solution for 10-15 minutes before recording the scans. All CV experiments were recorded under slow flow of argon on the solution. In order to record the CV background 0.1 V/s scan rate was used. Ferrocene ($E^\circ = 0.665$ V versus NHE)³⁴ was used as the internal reference.

2.3.2 Infrared, Electronic Absorption and NMR spectroscopies

A Bomem Michelson 120 FTIR spectrometer was used to record the infrared spectra of KBr disc of the samples which were corrected for background air.

Quantitative Electronic absorption spectra were collected using Cary 3 instrumentation and two matching quartz cell with length path of 1 cm. In order to set the baseline both cells containing the solvent were used. To collect the spectra of the sample both cells placed in the instrument, one contained solvent for baseline correction and the other one contained the sample solution.

^1H -NMR spectra of the samples were recorded using Bruker AMX-400 NMR or Bruker 300 Ultra Shield spectrometers with respect to TMS at 0.00 ppm. 5-10 mg of the samples in 1 mL deuterated solvent in a Norell XR-55 NMR tube was used for each sample.

2.3.3 IR- and UV-Vis-NIR Spectroelectrochemistry

All spectroelectrochemistry examinations were performed using OTTLE cell (Optically Transparent Thin Layer Electrode) (Figure 10) at room temperature. Similar to Hartl design³⁵ the cell consists of two polyethylene spacers in between two CaF_2 plates. Two 0.1 mm platinum wires each in contact with a piece of gold foil (500 line/inch, 60% transmittance, Buckbee Mears) were used as counting and worker electrodes and an Ag/AgCl wire was used as reference electrode. Electrodes were fitted in between the two layers of polyethylene spacer. The electrode wires were connected to tin coated copper wires to which the current would apply through the alligator clips. The sample in 0.1M TBAH solution was first filtered through 0.45 μm (μm) Millipore filters (syringe filters) and then introduced to the cell using 2 mL Luer-lock syringes via the cell's inlet and outlet ports. To insure the beam (IR or UV-Vis) passes only through the working electrode the top layer of the cell in front of the other two electrodes were masked using electrical tape (part 4 Figure 10). BAS CV-27 voltammograph was used to control the applied voltage and the electrochemistry of the solution was observed via Varian Cary 5 UV-Vis-NIR and Bohem Michelson 120 FTIR spectrophotometers. Prior to apply the voltage on complexes the background spectra were collected and the baseline was set using the electrolyte and solvent. Followed by the scan of the actual sample in the range

of 1900- 2300 cm^{-1} for IR and 450- 2500 nm for UV-Vis studies. Positive potentials were applied in order to generate the Ru(III) species. In order to monitor the reversibility of the redox processes, after each increase in positive potential and spectral data collection, the potential was returned to zero potential and the spectrum collected to demonstrate recovery of the starting complex's spectrum.

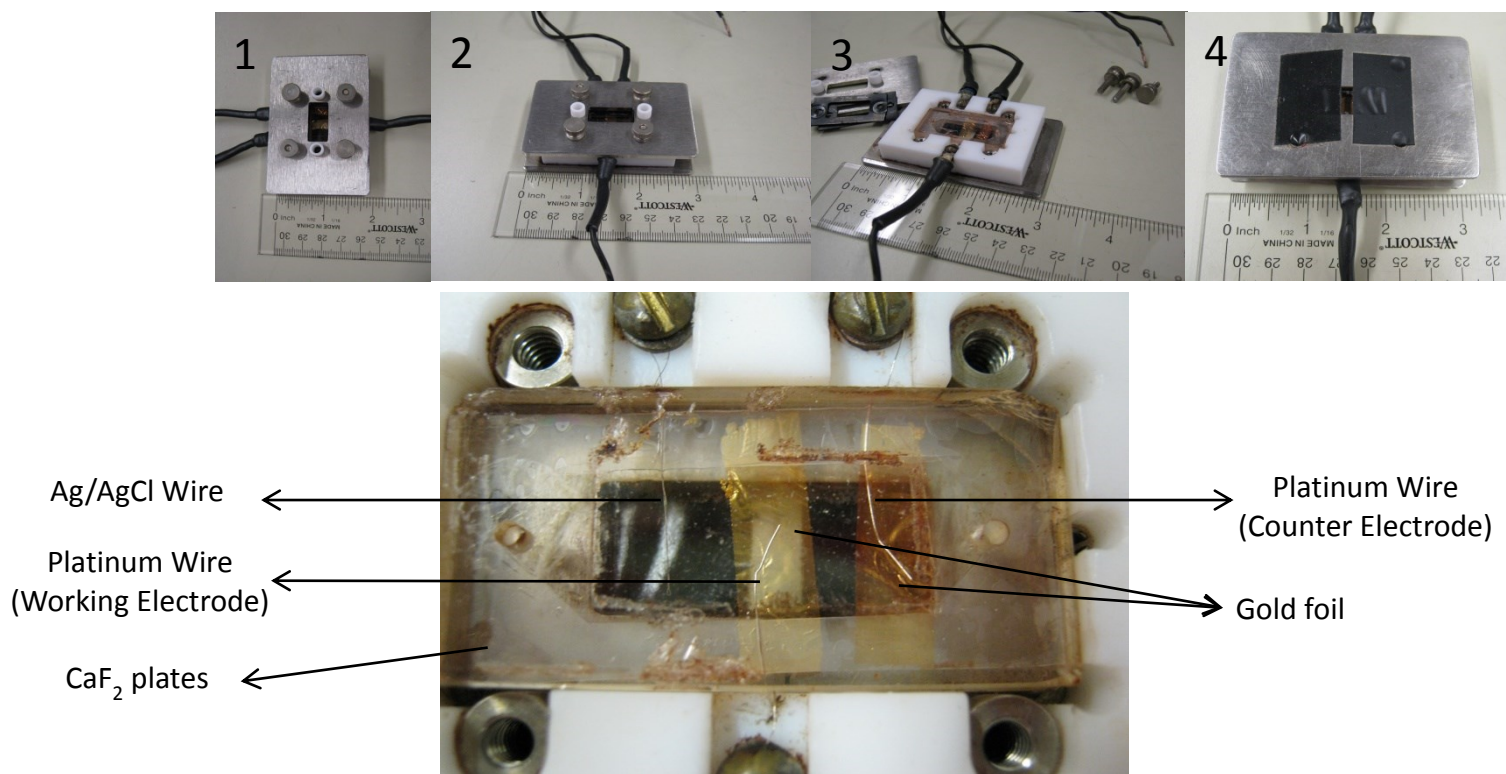


Figure 10 OTTLE cell used for spectroelectrochemistry studies.

2.3.4 Elemental Analyses

All elemental analyses were performed by Canadian Microanalytical Services, Ltd. in Delta, B. C., Canada

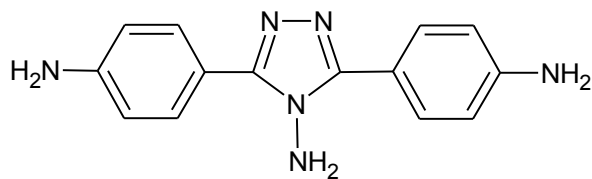
2.3.5 DFT Calculations

Gas-phase hybrid HF-DFT SCF calculations of equilibrium geometry, MOs, orbital energies and spin density distributions were performed with Wave function Inc., Spartan'14 Parallel program package, using the B3LYP/6-31G* model.

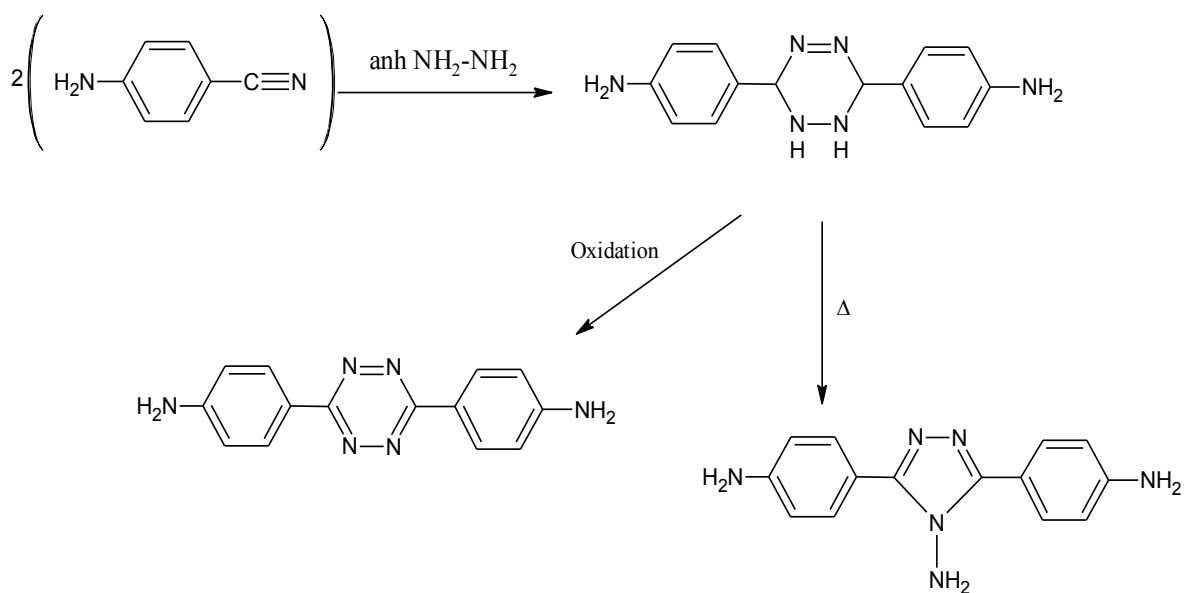
2.4 Results and Discussion

2.4.1 Synthesis

The steps used to prepare H₂tdpc(**4**) are shown in Scheme 4. The synthesis of the diamine (**1**) in 34% yield was significantly less than that reported in the literature (65%) and could probably be improved by a more effective preparation of anhydrous hydrazine. Also according to previous studies³⁶ on different substituted 1,4-dihydropyridazine compounds and actual experiment on 3,6-Bis-(4-aminophenyl)-1,2-dihydro-1,2,4,5-tetrazine higher temperature (as shown in Scheme 3) results in rearrangement of 6 member ring to 5 member white needle crystalline 3,5-diamino-4-amino-1,2,4-triazol compound.

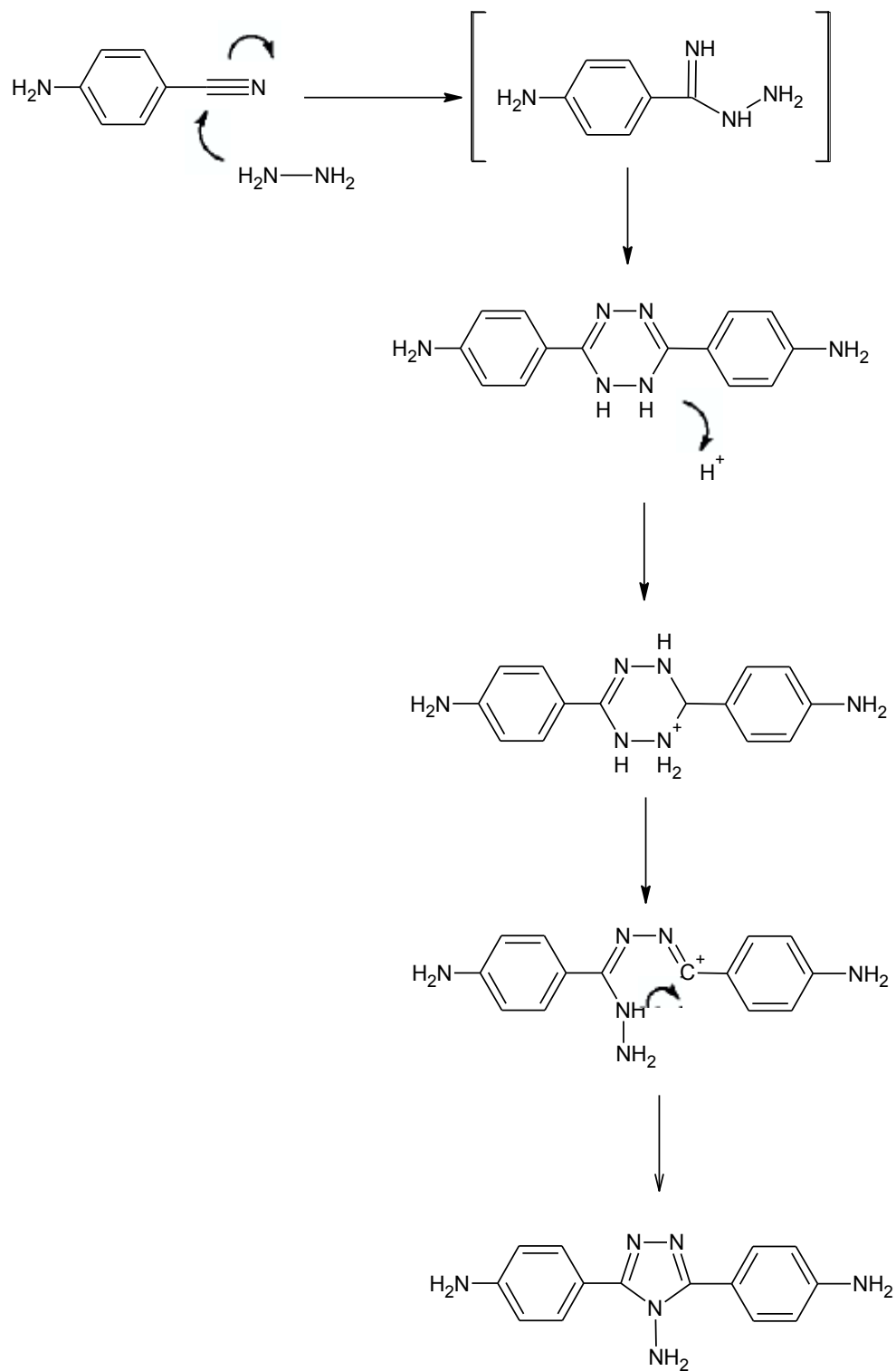


Scheme 2 Synthesis of 3,5-Diamino-4-amino-1,2,4-triazol and 3,6-Bis-(4-aminophenyl)-1,2-dihydro-1,2,4,5-tetrazine.

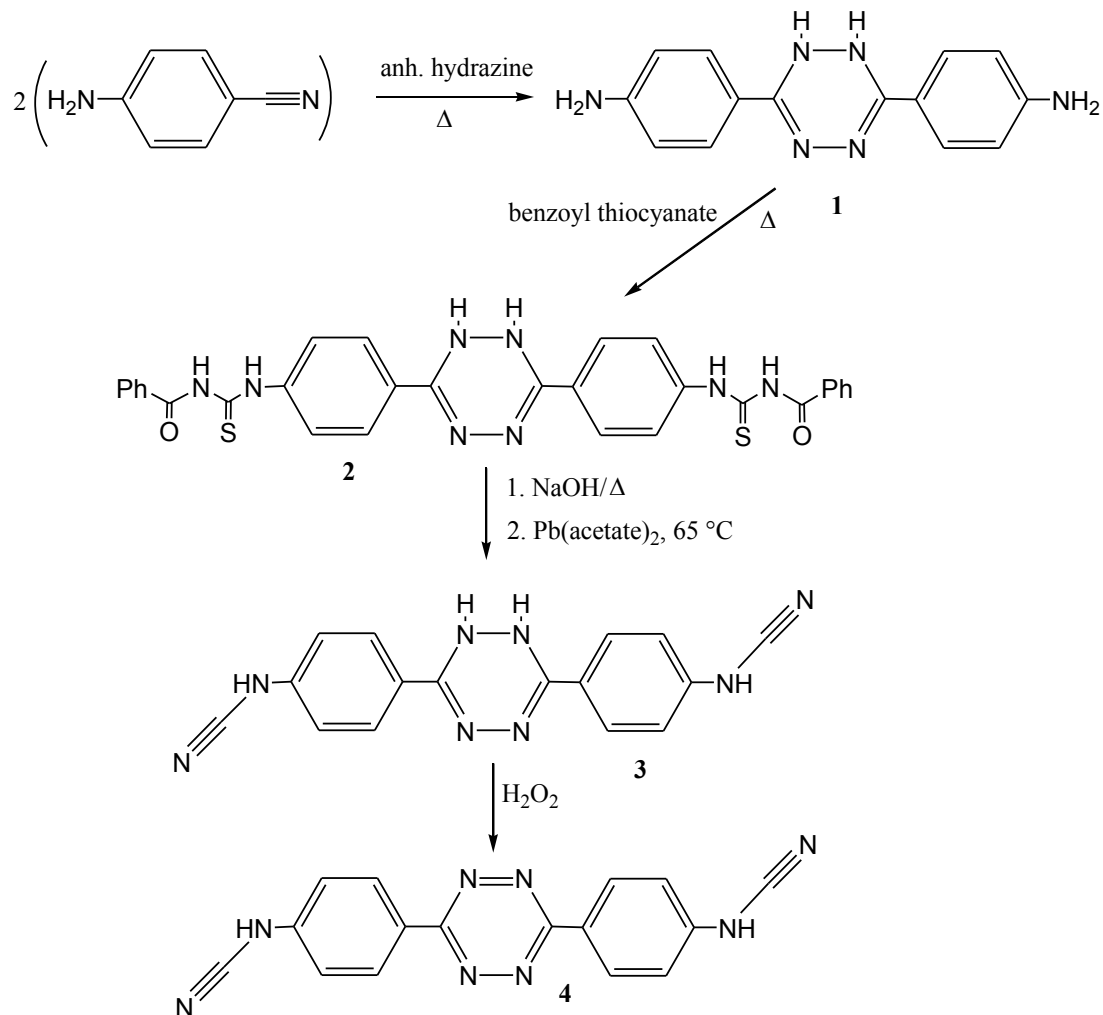


Nevertheless, the quantity of 3,6-bis-(4-aminophenyl)-1,2-dihydro-1,2,4,5-tetrazine was sufficient to proceed and, in latter steps, it was found to be important not to oxidize the dihydrotetrazine ring in this step as this deactivates the amine and prevents its conversion to the cyanamide. Reaction of the tetrazine compound with two equivalents of benzoyl thiocyanate formed the thiourea derivative in 77% crude yield which was then desulfurized by treatment with lead acetate followed by protonation with acetic acid to yield **3** (Scheme 4). Oxidation of crude **3** with hydrogen peroxide, followed by recrystallization from acetone/water gave H₂tdpc in 43% yield.

Scheme 3 Proposed Mechanism of 1,2-Dihydropyridazine to 4-Aminotriazol Recycling by Bentiss et al.³³



Scheme 4 Synthesis Procedure of H₂tdpc.



The dinuclear ruthenium complex $[\{\text{Ru}(\text{ttpy})(\text{bpy})\}_2(\mu\text{-tdpc})][\text{PF}_6]_2$ was prepared by the metathesis reaction of $\text{Tl}_{1.75}\text{tdpc}$ with two equivalents of $[\text{Ru}(\text{ttpy})(\text{bpy})\text{Cl}][\text{PF}_6]$. The complex is soluble in DMF and DMSO but only slightly soluble in poor donor solvents. Attempts to grow X-ray quality crystals were unsuccessful with the best results obtained by ether diffusion into a DMF solution of the complex which yielded thin, dark-red crystalline shards.

2.4.2 NMR Spectroscopy

¹H-NMR spectra of 3,6-bis-(4-aminophenyl)-1,2-dihydro-1,2,4,5-tetrazine (**1**), 3,5-diamino-4-amino-1,2,4-triazol, tdpCH₂ (**4**), Tl_{1.75}tdpc (**5**), [Ru(tpy)(bpy)]₂(μ-tdpc)][PF₆]₂ complex (**6**) and also ¹³C-NMR spectrum of tdpCH₂ (**4**) were all recorded in DMSO-d₆ with TMS as reference. The chemical shifts and integrations are listed in Table 1 also the spectra for all the products are shown in Figure 11 to Figure 16.

¹H-NMR spectrum of tdpCH₂ (**4**) showed the expected AX pattern of the phenyl ring protons and a broad singlet cyanamide proton chemical shift at 10.81 ppm.

The spectrum of Tl_{1.75}tdpc (**5**) (Figure 15) contains two doublets as expected and also two doublets at 8.4 and 7.2 ppm which are due to protonated form of this ligand, H₂tdpc. Unfortunately we were not able to purify it.

The ¹H-NMR spectrum of **6** is consistent with its formulation. Only two doublets at 7.72 and 6.17 ppm are observed for the tdp²⁻ ligand, with the correct integration for an equivalent coordination of its cyanamide groups to Ru(tpy)bpy moieties.

¹H-NMR peaks for compounds **1**, **4**, **6** and 3,5-diamino-4-amino-1,2,4-triazol have been assigned to the representative protons and are provided in parts B1 to B4 in the Appendix B.

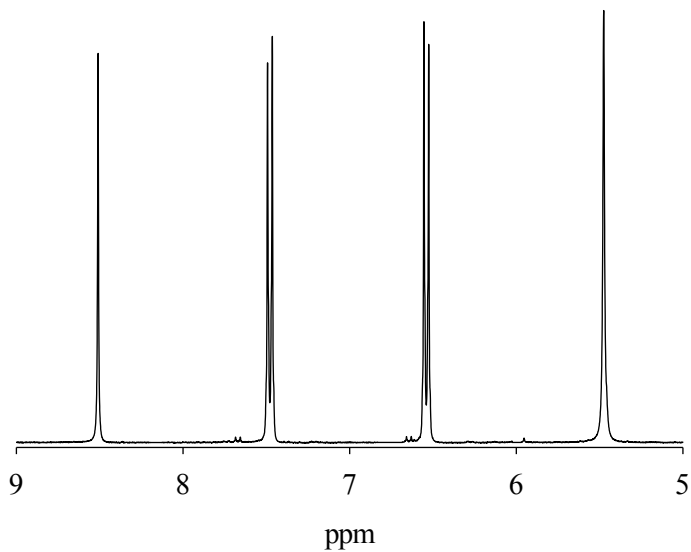


Figure 11 $^1\text{H-NMR}$ spectrum of 3,6-bis-(4-aminophenyl)-1,2-dihydro-1,2,4,5-tetrazine in DMSO-d_6 .

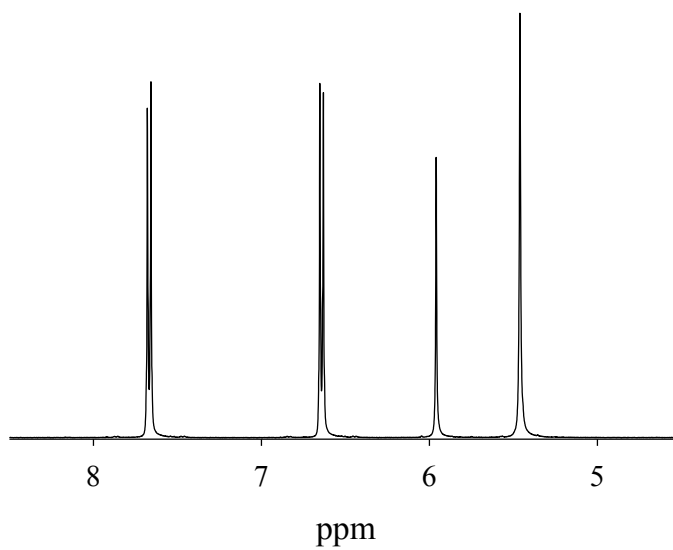


Figure 12 $^1\text{H-NMR}$ spectrum of 3,5-diamino-4-amino-1,2,4-triazol in DMSO-d_6 .

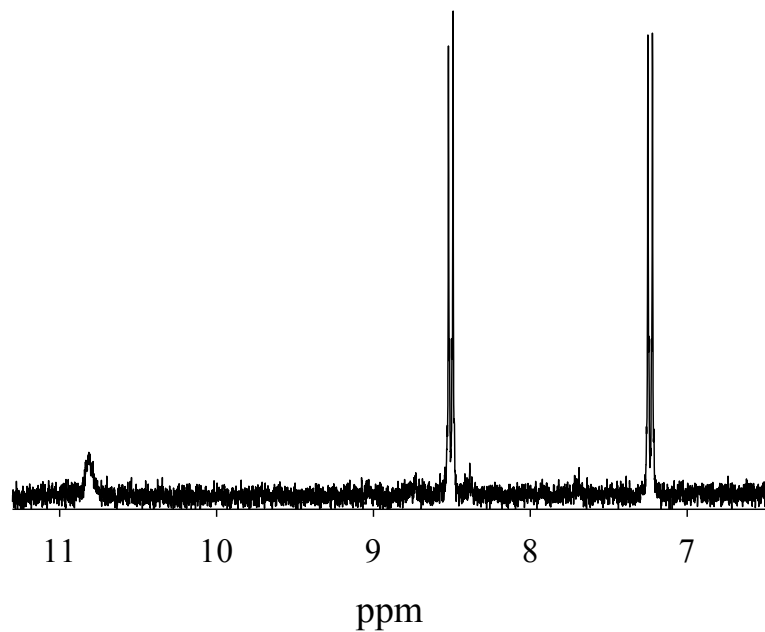


Figure 13 ^1H -NMR spectrum of H_2tdpc in DMSO-d_6 .

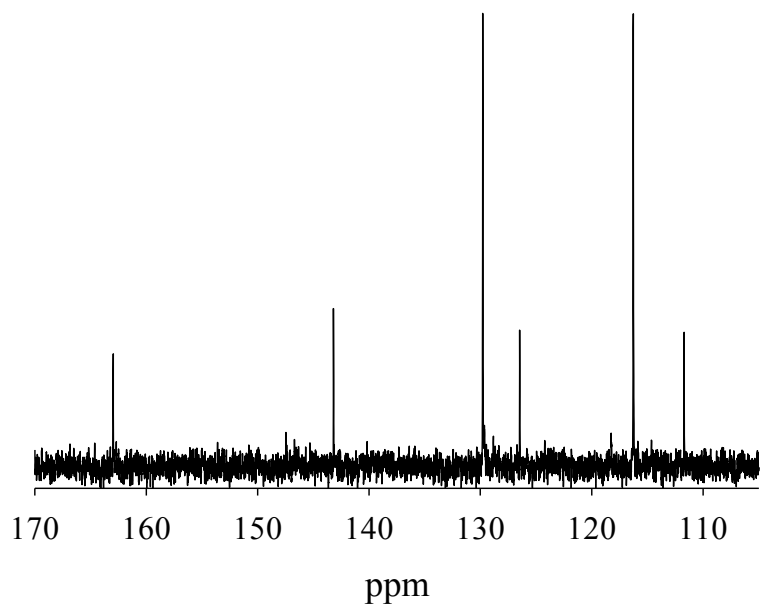


Figure 14 ^{13}C -NMR spectrum of H_2tdpc in DMSO-d_6 .

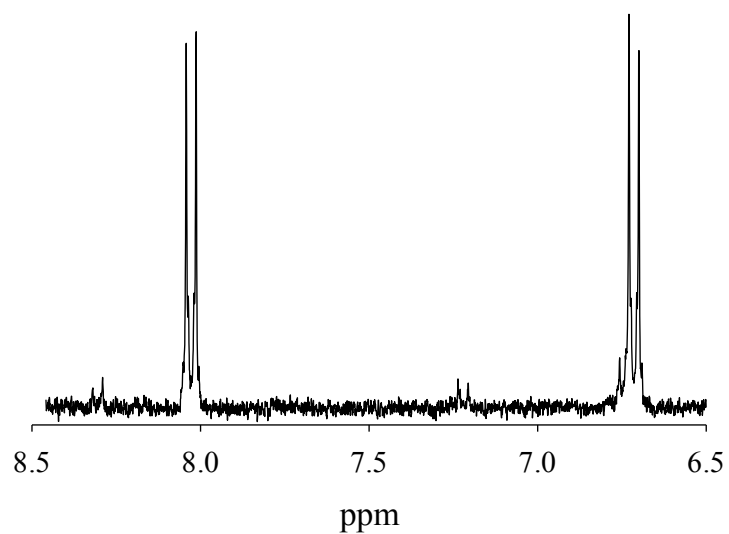


Figure 15 ^1H -NMR spectrum of $\text{Tl}_{1.75}\text{tdpc}$ in DMSO-d_6 . (Peaks at 7.2 and 8.4 ppm are due to impurities of protonated H_2tdpc).

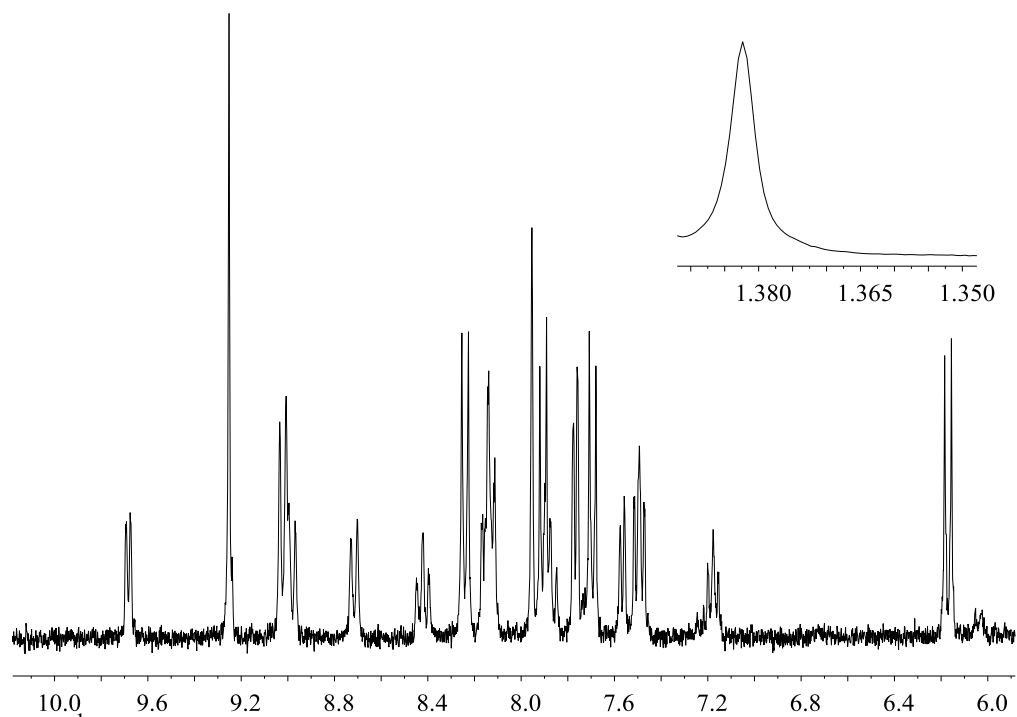


Figure 16 ^1H -NMR spectrum of $[\{\text{Ru}(\text{tpy})(\text{bpy})\}_2(\mu\text{-tdpc})][\text{PF}_6]_2$ in DMSO-d_6 .

Table 1 ¹H-NMR Chemical Shifts in DMSO-d₆

Compound	Chemical Shift (ppm)
3,6-Bis-(4-aminophenyl)-1,2-dihydro-1,2,4,5-tetrazine (1)	5.48 (s, 4H), 6.53 (d, 4H), 7.47 (d, 4H), 8.51 (s, 2H)
3,5-diamino-4-amino-1,2,4-triazol	5.46(s, 4H), 5.96 (s, 2H), 6.64 (d, 4H), 7.67 (d, 4H)
H ₂ tdpc (4)	10.81 (broad s, 2H), 8.50 (d, 4H), 7.25 (d, 4H)
Tl _{1.75} tdpc (5)	8.03 (d, 4H), 6.72 (d, 4H)
[{Ru(tpy)(bpy)} ₂ (μ-tdpc)][PF ₆] ₂ (6)	9.68 (d, 2H), 9.25 (s, 4H), 9.00 (dd, 6H), 8.72 (d, 2H), 8.45 (t, 2H), 8.24 (d, 4H), 8.18 (t, 6H), 7.94 – 7.83 (m, 6H), 7.77 (d, 4H), 7.72 (d, 4H), 7.57 (d, 2H), 7.52 – 7.46 (t, 4H), 7.18 (t, 2H), 6.17 (d, 4H), 1.38 (s, 18H)

2.4.3 IR-spectroscopy

The infrared spectra of neutral tdpCH₂ ligand, Tl_{1.75}tdpc and dinuclear [{Ru(tpy)(bpy)}₂(μ-tdpc)][PF₆]₂ complex were taken on KBr discs and corresponding stretching frequencies of ν(NCN) are tabulated among with literature values¹⁴ for adpcH₂ ligand, Tl₂adpc and dinuclear [{Ru(trpy)(bpy)}₂(μ-adpc)][PF₆]₂ complex in Table 2. Representative spectra of neutral tdpCH₂ ligand and its anionic form Tl_{1.75}tdpc and also [{Ru(tpy)(bpy)}₂(μ-tdpc)][PF₆]₂ complex are shown in Figure 17 to Figure 19.

The IR spectra of phenylcyanamide ligands are usually characterized by a strong $\nu(\text{NCN})$ in the range of 2200-2400 cm^{-1} . For the anionic form this band appears in the range of 2050-2150 cm^{-1} , which can be explained according to resonance structure of cyanamide (see Figure 3 in chapter 1).^{24,26,27,37,38} For the protonated H_2tdpc ligand the vibrational mode of NCN bond appears at 2228 cm^{-1} .

Table 2 Infrared Spectroscopy Data Performed as KBr discs

Compound	$\nu(\text{NCN})/\text{cm}^{-1}$
tdpcH_2	2228
$\text{Tl}_{1.75}\text{tdpc}$	2125
$[\{\text{Ru}(\text{tpy})(\text{bpy})\}_2(\mu\text{-tdpc})][\text{PF}_6]_2$	2176
adpcH_2	2225
Tl_2adpc	2078
$[\{\text{Ru}(\text{trpy})(\text{bpy})\}_2(\mu\text{-adpc})][\text{PF}_6]_2$	2161

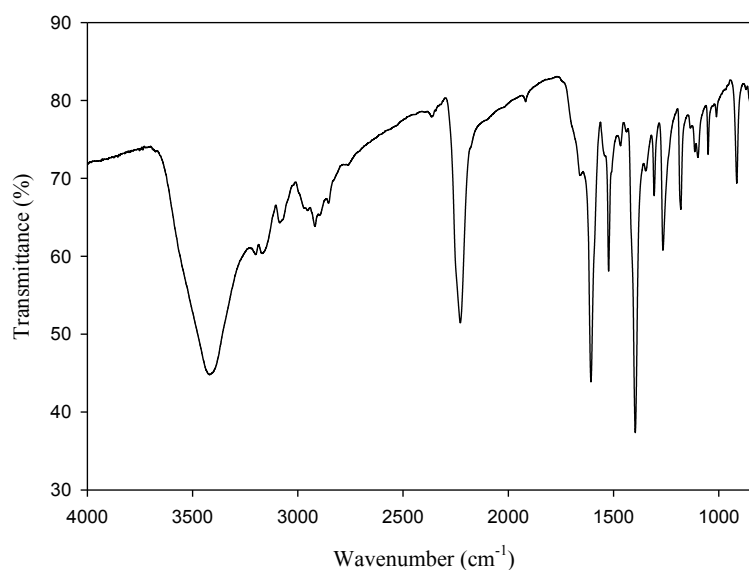


Figure 17 IR spectrum of H_2tdpc KBr pellet.

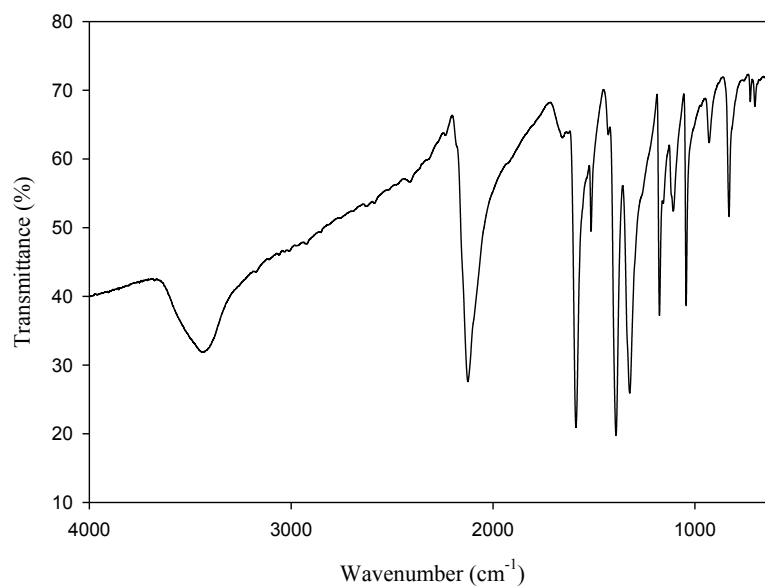


Figure 18 IR spectrum of $Tl_{1.75}tdpc$ KBr pellet.

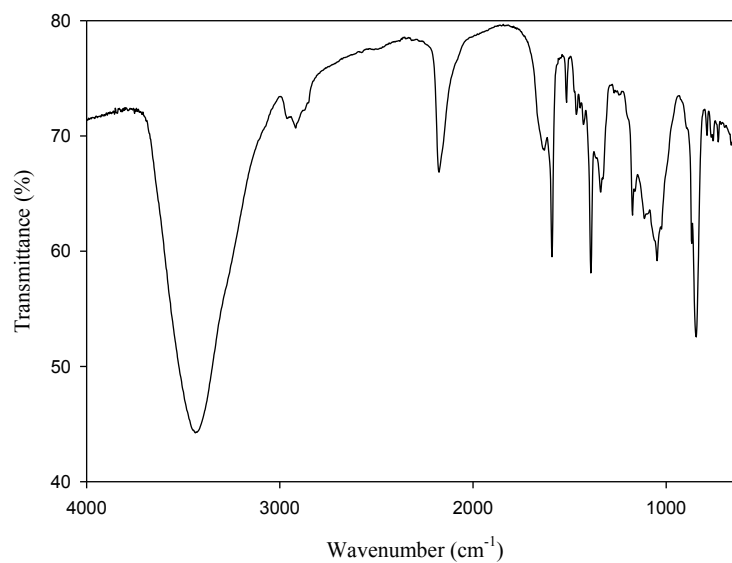
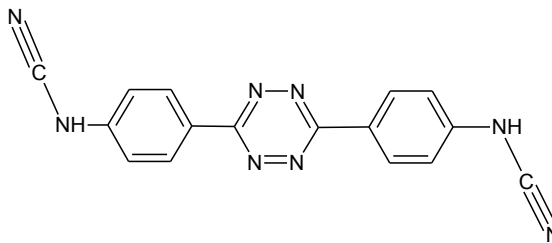


Figure 19 IR spectrum of $[Ru(tpy)(bpy)_2(\mu-tdpc)]_2[PF_6]_2$ KBr pellet.

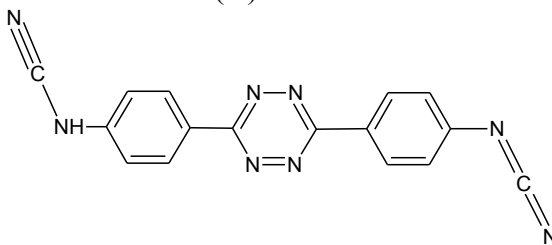
2.4.4 Electronic Absorption Spectroscopy

The electronic absorption data for tdpcH_2 (**4**), its thallium salt $\text{Tl}_{1.75}\text{tdpc}$ (**5**), and dinuclear $[\{\text{Ru}(\text{tpp})\text{(bpy)}\}_2(\mu\text{-tdpc})][\text{PF}_6]$ (**6**) complex have been placed in Table 3 as well as literature data for adpcH_2 (**7**), Tl_2adpc (**8**) and dinuclear $[\{\text{Ru}(\text{trpy})\text{(bpy)}\}_2(\mu\text{-adpc})][\text{PF}_6]$ (**9**) complex¹⁴ to compare. The UV-Vis spectra of tdpcH_2 (**4**), $\text{Tl}_{1.75}\text{tdpc}$ (**5**) and $[\{\text{Ru}(\text{tpp})\text{(bpy)}\}_2(\mu\text{-tdpc})][\text{PF}_6]$ (**6**) are shown in Figure 20 to Figure 23.

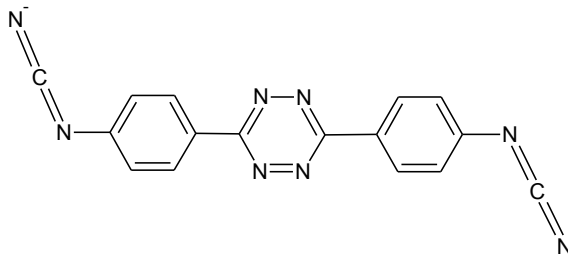
Scheme 5 Protonated, Monoprotonated and Deprotonated Forms of tdpc Ligand.



(A)



(B)



(C)

The electronic spectrum of **4** (form A in Scheme 5) is shown in Figure 17 and that of the dianion (structure C Scheme 5) is shown in Figure 19. The spectrum of **4** in DMF

is a mixture of protonated, deprotonated and possibly monoprotonated (structure B in Scheme 5) forms. This occurs because DMF, strong donor solvent, is acting as a base.

The complex's spectrum (Figure 23) shows absorptions centered at ~300 nm, which are assigned to $\pi \rightarrow \pi^*$ transitions of phenyl and pyridine moieties, and a broad visible absorption centered at 450 nm. The latter is likely due to overlapping tdpc²⁻ ILCT transitions and Ru(II)-to-tpy and -bpy metal-to-ligand charge transfer (MLCT) transitions.

Table 3 Quantitative Electronic Absorption Spectral Data

Compound	Absorption / nm ($\epsilon/M^{-1}cm^{-1}$)
4^a	275 (37000), ($\pi \rightarrow \pi^*$ phenyl) 335 (26000), (HNCN \rightarrow Tetrazine)
5^b	455 (54000) (NCN \rightarrow Tetrazine)
6^a	290 (150000), ($\pi \rightarrow \pi^*$ bpy & phenyl) 436 (78000), ($\pi \rightarrow \pi^*$ MLCT & 4 ILCT),
8^b	500 (54400), 523 (51500), (NCN \rightarrow Azo ILCT)
9^b	293 (81900), ($\pi \rightarrow \pi^*$ bpy, terpyrine & phenyl) 317 (72100), 490 (69100), (ILCT, Ru(II)- bpy & Ru(II)- trpy) ¹⁴

^a in CH₃CN

^b in DMF

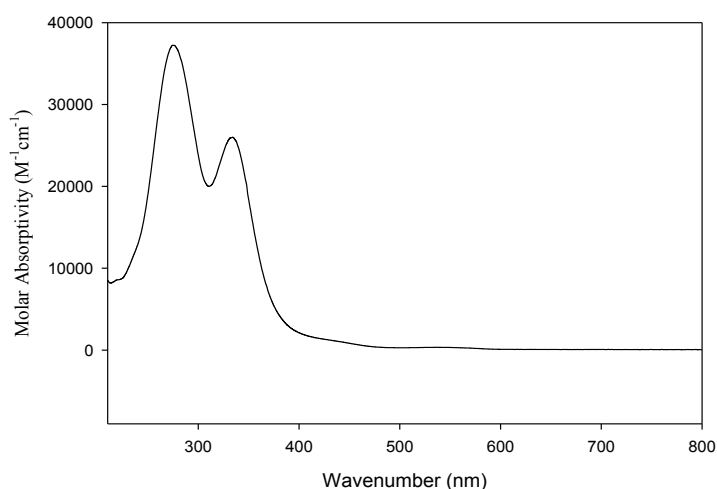


Figure 20 Electronic absorption spectrum of H₂tdpc (**4**) in acetonitrile.

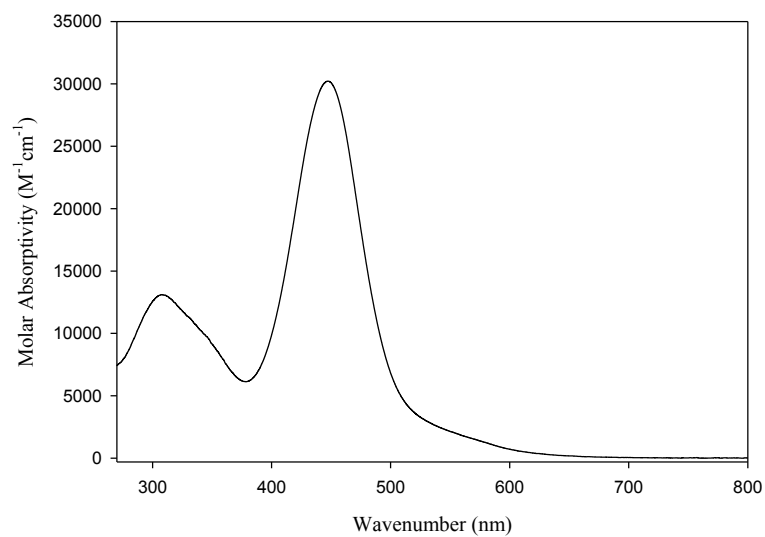


Figure 21 Electronic absorption spectrum of H₂tdpc (**4**) in DMF.

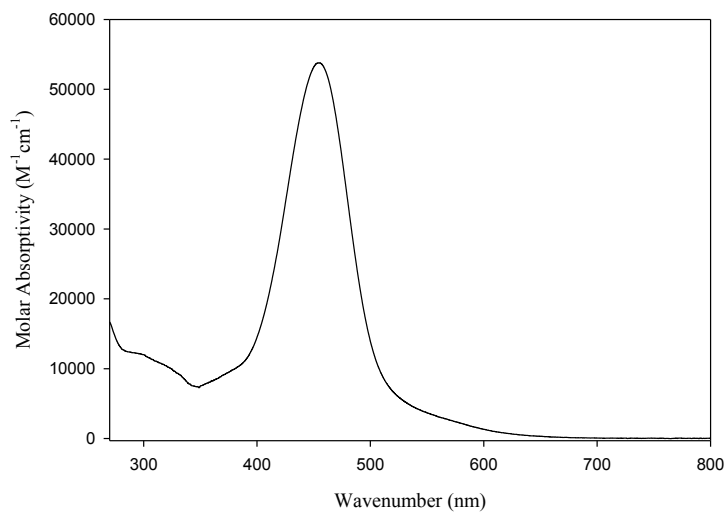


Figure 22 Electronic absorption spectrum of Tl_{1.75}tdpc (**5**) in DMF.

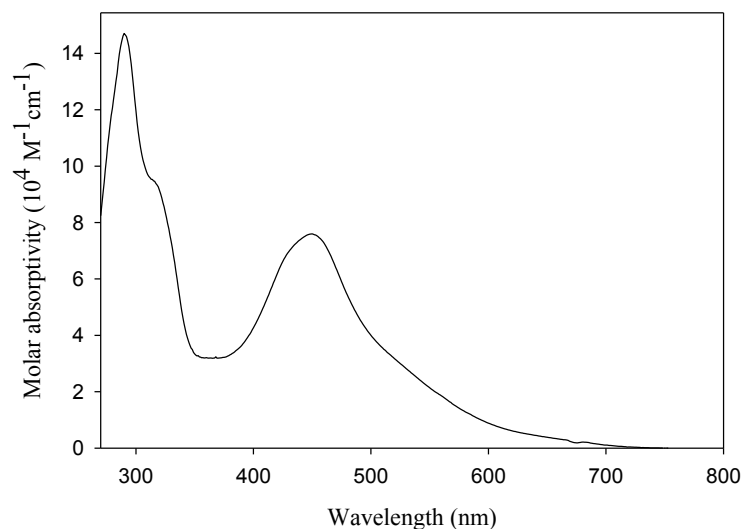


Figure 23 Electronic absorption spectrum of [$\{\text{Ru}(\text{tpy})(\text{bpy})\}_2(\mu\text{-tdpc})\][\text{PF}_6]_2$ (**6**) in DMF.

2.4.5 Electrochemistry

The cyclic voltammetry of [$\{\text{Ru}(\text{tpy})(\text{bpy})\}_2(\mu\text{-tdpc})\][\text{PF}_6]_2$ (**6**) in DMF (Figure 24) showed only one oxidation wave at 0.98 V vs. NHE which is at similar potential to that of the reagent complex $[\text{Ru}(\text{tpy})(\text{bpy})\text{Cl}][\text{PF}_6]$ whose voltammogram shows a Ru(III/II) couple at 1.04 V vs NHE.¹³ For [$\{\text{Ru}(\text{tpy})(\text{bpy})\}_2(\mu\text{-tdpc})\]^{2+}$, the separation between anodic and cathodic waves ($\Delta E_p = 140$ mV) and the shape of the anodic and cathodic waves is consistent with two overlapping Ru(III/II) couples. Using the method of Taube and Richardson,³⁹ we estimated the separation between these couples to be 100 mV which corresponds to a comproportionation constant of only $K_c = 50$. Mixed-valent [$\{\text{Ru}(\text{tpy})(\text{bpy})\}_2(\mu\text{-tdpc})\]^{3+}$ (**6**) is therefore a weakly coupled Class II complex.

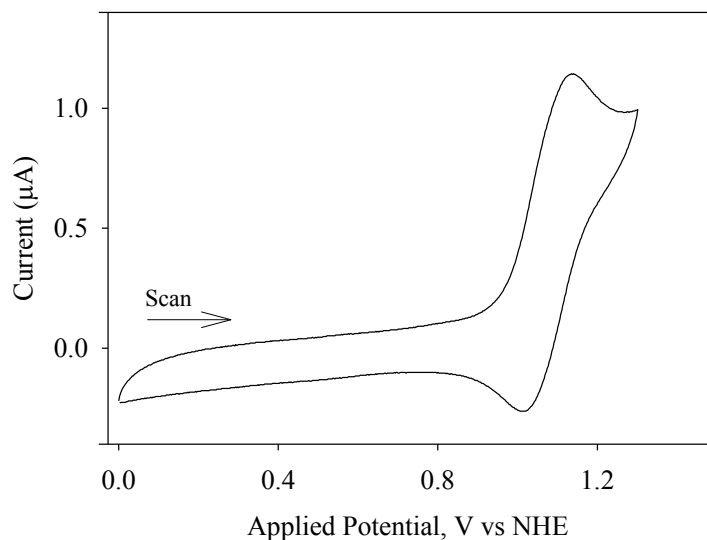


Figure 24 Cyclic voltammogram of $[\{Ru(tpy)(bpy)\}_2(\mu\text{-tdpc})][PF_6]_2$ in DMF with 0.1 M tetrabutylammonium hexafluorophosphate, using platinum counter and working electrode, silver wire pseudo-reference (cobaltocene internal reference, $E^\circ = -0.589$ V versus NHE) at scan rate of 100mV/s.

Table 4 Cyclic Voltammetry Data for Dinuclear Ruthenium Complexes with tdpc^{2-} and adpc^{2-} Bridging Ligands

Complex	Ru III/II
$[\{Ru(tpy)(bpy)\}_2(\mu\text{-tdpc})][PF_6]_2$ (6)	1.04 ^(a)
$[\{Ru(trpy)(bpy)\}_2(\mu\text{-adpc})][PF_6]_2$ (9)	0.79 ^(a) 1.57 ^(a) 0.91 ^(b) ~ 1.6 ^(b)

^(a) In DMF ^(b) In CH_3CN

2.4.6 Vis-NIR Spectroelectrochemistry

The spectroelectrochemistry of $[\{Ru(tpy)(bpy)\}_2(\mu\text{-tdpc})]^{2+}$ (6) in DMF solution is shown in Figure 25. Upon oxidation to form the [Ru(III),Ru(II)] complex (Figure 25a), the band at 450 nm decreases and a new band appears at 1190 nm which is assigned to the Ru(III)-cyanamide ligand-to-metal charge transfer (LMCT) chromophore.²⁷ At

higher positive potentials, oxidation to the [Ru(III),Ru(III)] complex (Figure 25b) causes the intensity of the LMCT band at 1190 nm to initially increase, consistent with there being two LMCT chromophores, and a decrease in the low energy tail. Unfortunately, further oxidation results in the loss of isosbestic points and the general loss of absorption intensity in the vis-NIR region. The inability to recover the [Ru(II),Ru(II)] spectrum indicated decomposition of the [Ru(III),Ru(III)] complex. Nevertheless, the initial loss of the low energy tail is consistent with its assignment as an intervalence transition. Deconvolution of this low energy tail, assuming Gaussian band shape, yielded an intervalence transition with wavelength 1530 nm (or $\nu_{\max} = 6540 \text{ cm}^{-1}$), corrected⁽¹⁾ $\epsilon_{\max} = 7680 \text{ M}^{-1}\text{cm}^{-1}$, and band width at $\frac{1}{2} \epsilon_{\max}$, $\nu_{1/2} = 3420 \text{ cm}^{-1}$. This band width is in reasonable agreement with that calculated by the Hush model ($\nu_{1/2} = \sqrt{2310\nu_{\max}} = 3890 \text{ cm}^{-1}$) and further confirms [$\{\text{Ru}(\text{ttpy})(\text{bpy})\}_2(\mu\text{-tdpc})$]³⁺ as a Class II complex. The resonance exchange H_{ad} was calculated to be 400 cm^{-1} using equation 6 (chapter 1),⁴⁰ where r (transition dipole moment length) was taken as the through space metal-metal separation 21 \AA .

⁽¹⁾ At small K_c the intensity of an intervalence transition should be corrected for the comproportionation equilibrium of species other than the mixed-valence complex. For $K_c = 50$, the percentage mixed-valence complex is given by $P = \frac{\sqrt{K_c}}{\sqrt{K_c+2}} = 78\%$.

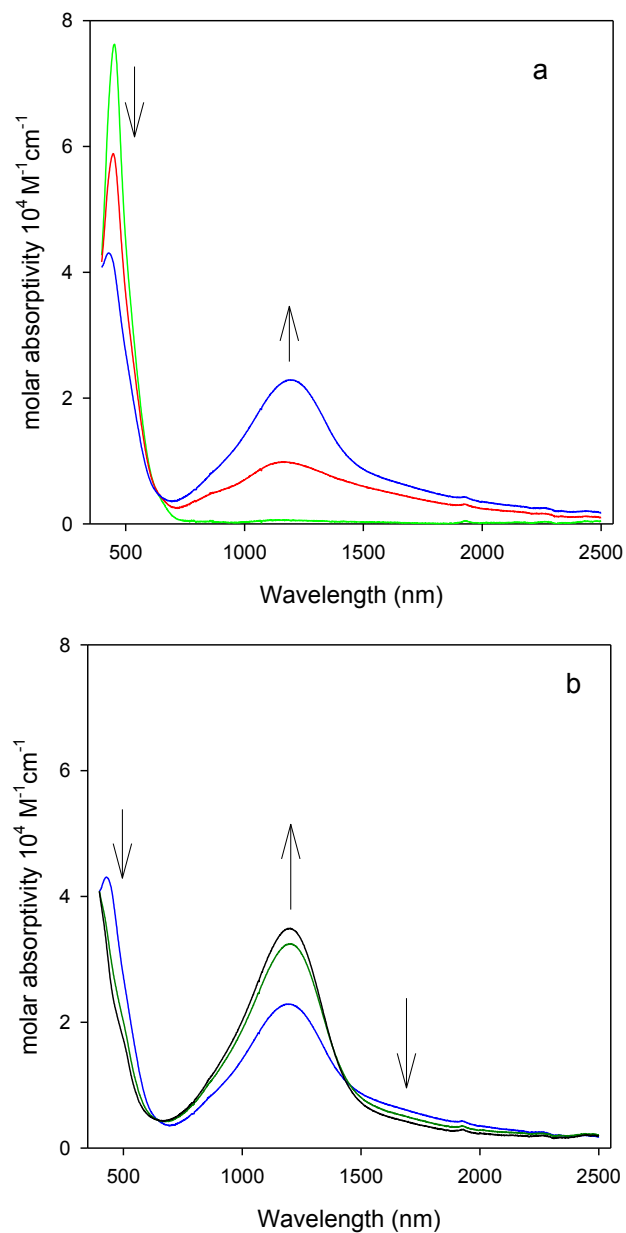


Figure 25 Vis-NIR spectroelectrochemistry of $[\{\text{Ru}(\text{tpy})(\text{bpy})\}_2(\mu\text{-tdpc})][\text{PF}_6]_2$ (**6**) in DMF solution, 0.1 M TBAH. a) oxidation forming $[\{\text{Ru}(\text{tpy})(\text{bpy})\}_2(\mu\text{-tdpc})]^{3+}$ and b) partial oxidation to form $[\{\text{Ru}(\text{tpy})(\text{bpy})\}_2(\mu\text{-tdpc})]^{4+}$.

2.4.7 IR-spectroelectrochemistry

The IR spectroelectrochemistry of [$\{\text{Ru}(\text{tppy})(\text{bpy})\}_2(\mu\text{-tdpc})\][\text{PF}_6]_2$ (**6**) in DMF solution is shown in Figure 26. Upon oxidation to the mixed-valence state, the more intense cyanamide stretching band $\nu(\text{NCN})$ at 2160 cm^{-1} decreases and a very weak $\nu(\text{NCN})$ band appears at 2030 cm^{-1} which arises from the cyanamide group bound to Ru(III).

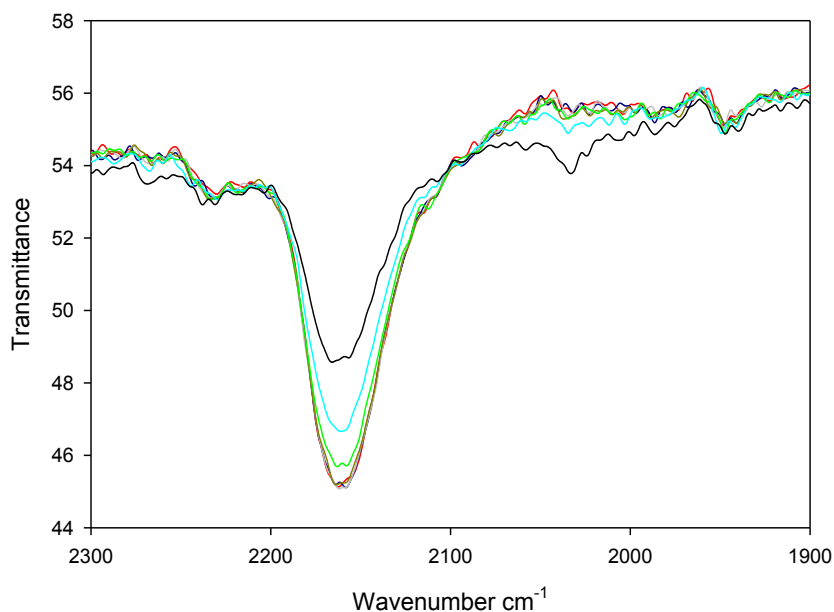


Figure 26 IR spectroelectrochemistry of [$\{\text{Ru}(\text{tppy})(\text{bpy})\}_2(\mu\text{-tdpc})\][\text{PF}_6]_2$ (**6**) in DMF solution, 0.1 M TBAH showing oxidation to [$\{\text{Ru}(\text{tppy})(\text{bpy})\}_2(\mu\text{-tdpc})\]^{3+}$.

As explained in chapter 1 similar shifts in $\nu(\text{NCN})$ bands with ruthenium oxidation state have been observed for mononuclear and dinuclear ruthenium cyanamide complexes¹² and is due to a change in the contribution of carbodiimide and nitrile resonance forms to the cyanamide group. Importantly, the appearance of two $\nu(\text{NCN})$ bands in the mixed-valence complex supports a valence-trapped state.

2.4.8 DFT Calculation

The frontier molecular orbitals and energies of adpc^{2-} and tdpc^{2-} are shown in Figure 27. The equilibrium geometry of both dianion bridging ligands is approximately planar in which the cyanamide groups adopt an *anti*-conformation. A planar geometry was found for substituted 1,4-dicyanamidebenzene dianion ligands and their complexes and also complexes of adpc^{2-} (**9**) which is a consequence of the mixing of cyanamide and aromatic π systems. Furthermore, (as shown in Figure 27), the HOMOs of adpc^{2-} (**8**) and tdpc^{2-} (**5**) are π non-bonding and span the entire molecule. The HOMO of tdpc^{2-} (**5**) at 0.7 eV is 0.7 eV more stable than that of adpc^{2-} (**8**) and this extra stability is expected to decrease metal-metal coupling via hole-transfer superexchange when tdpc^{2-} bridges two metal ions.²⁹

The DFT calculation of the spin density distribution in the mixed-valence complex $[\{\text{Ru}(\text{tpy})(\text{bpy})\}_2(\mu\text{-tdpc})]^{3+}$ (**6**) is shown in Figure 28 in which spin density resides mostly in $p\pi$ atomic orbitals of the bridging ligand with minor $d\pi$ orbital contributions from the ruthenium ions. Based on this calculation alone, a radical bridging ligand state is predicted however solvent interactions can shift spin density onto the metal ions as has been demonstrated for $[\{\text{Ru}(\text{NH}_3)_6\}_2(\mu\text{-dicyd})]^{3+}$ where dicyd^{2-} is 1,4-dicyanamide benzene dianion²⁹ and because of this interpretation of Figure 28 should be qualified. In addition, the cyanamide groups in this calculation are equivalent but this is inconsistent with the observation of two $\nu(\text{NCN})$ bands in the IR spectroelectrochemistry of the mixed-valent complex in Figure 26.

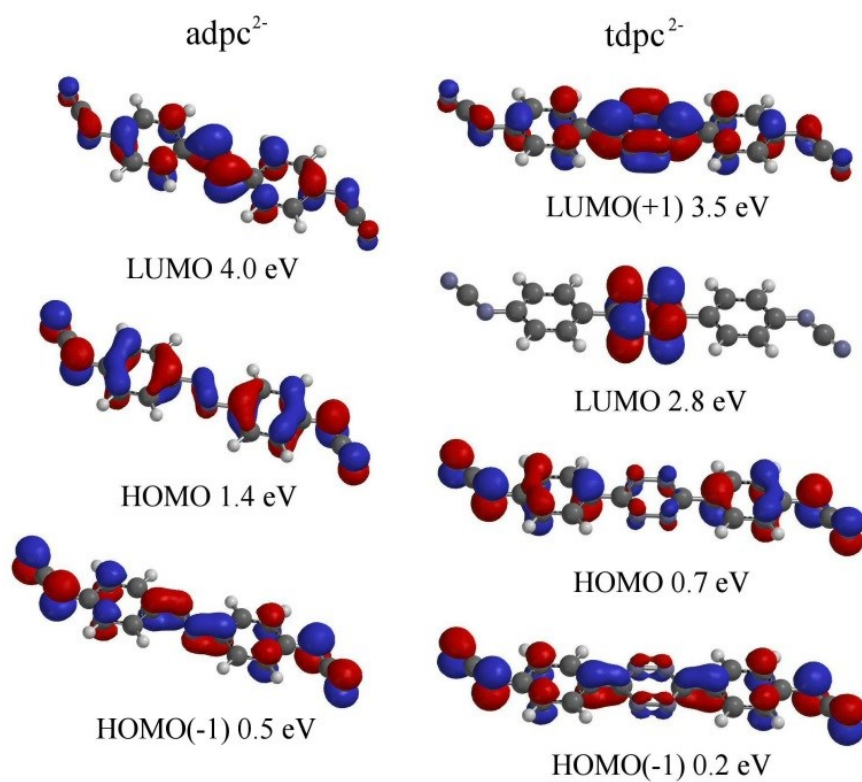


Figure 27 DFT calculated frontier molecular orbitals and energies of adpc^{2-} (**8**) and tdpc^{2-} (**5**).

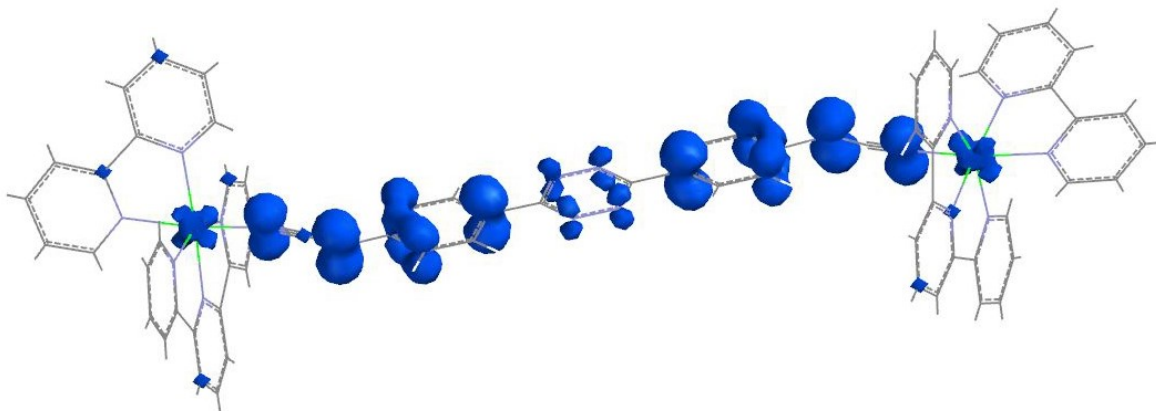


Figure 28 Spin density distribution of $[\{\text{Ru}(\text{tpy})(\text{bpy})\}_2(\mu\text{-tdpc})]^{3+}$ (**6**).

2.5 Conclusion

The novel bridging ligand, 3,6-bis(phenylcyanamido)-1,2,4,5-tetrazine (tdpcH₂) (**4**) and its dinuclear complex, [$\{\text{Ru}(\text{tpp})\text{(bpy)}\}_2(\mu\text{-tdpc})\text{][PF}_6\text{]}_2$ (**6**), were prepared and characterized by elemental analysis, and ¹H NMR spectroscopy. Cyclic voltammetry and vis-NIR and IR spectroelectrochemistry of [$\{\text{Ru}(\text{tpp})\text{(bpy)}\}_2(\mu\text{-tdpc})\text{]}^{2+}$ (**6**) showed that [$\{\text{Ru}(\text{tpp})\text{(bpy)}\}_2(\mu\text{-tdpc})\text{]}^{3+}$ is a Class II mixed-valence system with metal-metal coupling of 400 cm⁻¹ assuming a metal-metal separation of 21 Å. This was contrasted with metal-metal coupling of 2600 cm⁻¹ for the Class III mixed-valence system [$\{\text{Ru}(\text{tpy})\text{(bpy)}\}_2(\mu\text{-adpc})\text{]}^{3+}$ (**9**) and a metal-metal separation of 19.5 Å. DFT calculations of adpc²⁻ and tdpc²⁻ revealed that the HOMO of tdpc²⁻ is 0.7 eV more stable than that of adpc²⁻ and this together with a slightly longer metal-metal separation is expected to diminish hole-transfer superexchange via the tdpc²⁻ ligand. Gas phase DFT calculations of the spin density distribution of [$\{\text{Ru}(\text{tpp})\text{(bpy)}\}_2(\mu\text{-tdpc})\text{]}^{3+}$ showed most of the spin density localized on the bridging ligand. However this result is in disagreement with IR spectroelectrochemistry results and recent studies have shown that the distribution of spin density can be dramatically shifted by solvent interactions.

Chapter 3: Photo-linkage Isomerism in a Dinuclear DMSO Complex

3.1 Introduction

Among different classes of molecular sensors and optical molecular devices such as molecular switches and storage devices are photo-switchable bi-stable complexes.^{41,42} Such compounds undergo fast photo-induced isomerization between ground and metastable states.⁴³ One class of ligands with photo-linkage isomerism ability is the S \rightarrow O isomerization in sulfoxide groups^{44,45} which arises from the metal-to-ligand charge transfer (MLCT) excited state. This linkage isomerism can also occur as a result of the thermal oxidation of the metal centre.

According to Hard-Soft Acid Base (HSAB) theory, the hard acid Ru(III) would preferably bond to hard base such as oxygen in dmsO to form Ru(III)-sulfoxide(O) while Ru(II) as soft acid prefers sulfur binding site of sulfoxide as Ru(II)-sulfoxide(S) (as is shown in Figure 29).

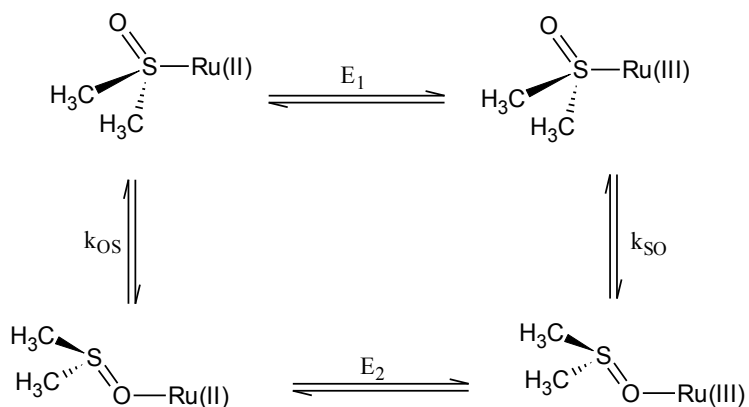


Figure 29 Electrochemically induced linkage isomerism in Ru-sulfoxide complexes.⁴⁶

Recent studies^{44,46-49} on ruthenium-sulfoxide complexes have shown the same linkage isomerism can be induced photochemically. The ultra-fast charge transfer from $d\pi$ -orbital of metal centre to π^* -orbitals of the π -acceptor ligand generates a Ru(III) ion in the excited state. In response dmsO rearranges to the sulfoxide(O) species. The excited state then rapidly relaxes to the metastable Ru(II)-sulfoxide(O) which undergoes slow conversion to Ru-sulfoxide(S) isomer (Figure 30).

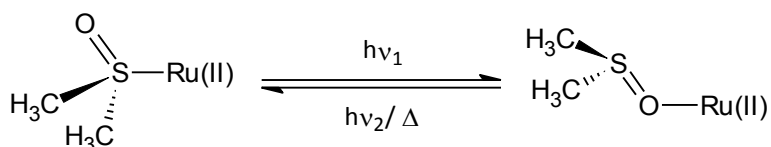
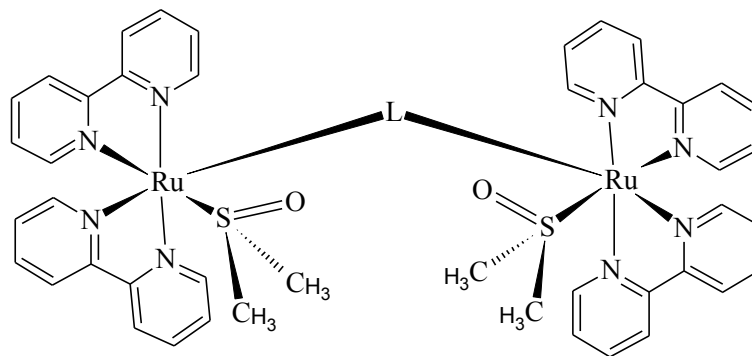


Figure 30 Photo-induced linkage isomerism in ruthenium-sulfoxide complexes.

Past studies on mixed-valence ruthenium complexes bridged by aromatic phenylcyanamide complexes showed that these complexes possess solvent and coordination sphere sensitive metal-metal coupling. Creating photo-switch mixed-valence complexes first prerequisites finding an appropriate coordination sphere with ability of photoisomerism and mixed valency. According to recent studies,⁴⁶ the coordination sphere of $\text{cis-}[\{\text{Ru}(\text{bpy})_2(\text{dmsO})(\text{R-pcyd})\}]^+$ complexes, where bpy is 2,2'-bipyridine, dmsO is dimethylsulfoxide and R-pcyd is substituted phenylcyanamide ligands, fits this requirement. Indeed the quantum yield of dmsO linkage isomerism in these complexes was shown to be dependent on the donor properties of the phenylcyanamide ligand.

The objective of present research work is to synthesize a mixed-valence complex with the same coordination sphere as $[\{\text{Ru}(\text{bpy})_2(\text{dmsO})(\text{R-pcyd})\}]^+$. The proposed structure of the complex $[\{\text{Ru}(\text{bpy})_2(\text{dmsO})\}_2(\mu\text{-L})]^{n+}$ is:



There are many studies¹⁴ that show that when $L = \mu\text{-adpc}^{2-}$, this ligand can extend the electronic transition pathway via its extended conjugated π system. Interaction of the HOMO and LUMO of the ligand with the donor and acceptor orbitals of ruthenium ion make superexchange possible through both mechanisms, hole- and electron- transfer, in $[\{\text{Ru}(\text{trpy})(\text{bpy})\}_2(\mu\text{-adpc})]^{2+}$ complex.

In order to examine the ability of this ligand in superexchange in dinuclear complexes another class of di-bridged ruthenium complex $\{\text{Ru}(\text{bpy})_2\}_2(\mu\text{-adpc})_2$ have been synthesized and characterized by elemental analysis, $^1\text{H-NMR}$ and IR spectroscopies which in the next step was reacted with DMSO in mild acidic solution headed for replacing one of the bridging ligands with two DMSO ligands. The pure $[\{\text{Ru}(\text{bpy})_2(\text{dmsO})\}_2(\mu\text{-adpc})][\text{PF}_6]_2$ product has been characterize by elemental analysis, $^1\text{H-NMR}$ and IR spectroscopies.

3.2 Experimental

3.2.1 Materials

Glacial acetic acid ($\leq 99.7\%$, ACS reagent grade, Anachemia), ammonium thiocyanate (Sigma-Aldrich), 4-nitroaniline ($\geq 97.5\%$, Sigma), potassium peroxomonosulphate (Oxone[®]) (4.5% active oxygen, Acros), sulfuric acid (ACS reagent grade, 98%, Anachemia), benzoyl chloride (99%, Sigma-Aldrich), triethyl amine (99.5%, Fluka), lead(II) acetate trihydrate (ACS reagent grade, 99+%, Aldrich), sodium hydroxide (97%, ACS reagent grade, Caledon Labs.), thallium (I) acetate ($\geq 99\%$, Sigma-Aldrich) (**Caution: highly toxic! Danger of cumulative effect**), ammonium hexafluorophosphate (99.5%, Alfa Aesar), ruthenium trichloride hydrate (99.9%, Alfa Aesar), lithium chloride ($\geq 99\%$, Sigma-Aldrich), 2,2'-bipyridine (Reagent plus, $\geq 99\%$, Sigma-Aldrich), dimethyl sulfoxide (anhydrous, $\geq 99.5\%$, Sigma-Aldrich) and dimethylformamide DMF (Caledon) were used as received.

3.2.2 Preparation of 4,4'-Azodianiline

5 g (36 mmol) 4-nitroaniline was dissolved in 70 mL 5.5 M H₂SO₄ solution (20.5 mL H₂SO₄ in 49.5 mL water). 23 g (0.15 mole) Oxone[®] was added gradually (3 times, each time 8 g) during an hour to the sulfuric acid solution at 60-65 °C. An extra 10 mL of water was added to the thick mixture to help stirring the solution better. The reaction mixture was stirred for another hour at the same temperature then filtered and yellowish orange precipitate was washed 3 times with 250 mL distilled water. Recrystallization

from 80 mL boiling acetic acid yielded 3.5 g (13 mmol, 72%) red needle 4,4'-azodi(nitrobenzene) crystals which was washed with 100 mL cold glacial acetic acid.

Dried 4,4'-azodi(nitrobenzene) was then dissolved in 100 mL (3:1) ethanol/water solution. After addition of 44 g (0.56 mole) Na₂S the solution was refluxed for one hour. During reflux time color of the solution changed from red to dark-blue to reddish black. After one hour the round bottom flask was set aside to cool down to room temperature for 40 min, then the solution was chilled down in the fridge. After cooling completely (overnight in the fridge) 2.3 g (11 mmol, 82%) pure red needle crystals of 4,4'-azodianiline was filtered off the solution. Overall yield: 60%. ¹H NMR (300 MHz, DMSO – d₆): 7.53 (d, 4H); 6.63 (d, 4H); 5.72 (s, 4H) ppm. Mpt: 251 °C (Literature Mpt: 245 °C)

3.2.3 Preparation of 4,4'-Azodi(phenylcyanamide), (adpcH₂) (7)

4.5 mL benzoyl chloride in 50 mL acetone was added drop-wise to refluxing solution of 2.44 g ammonium thiocyanate in 50 mL acetone precipitating ammonium chloride as the reaction proceeded. After the addition was complete, the reaction mixture was refluxed for a further 15 minutes. Solution of 4,4'-azodianiline (3.4 g, 16 mmol) in 200 mL of hot acetone was then added drop-wise to the refluxing mixture and the reaction mixture refluxed for 1 h. The reaction mixture was poured into 1 L stirring distilled water precipitating the brownish-green thiourea derivative which was filtered and washed with distilled water. The thiourea derivative was then added to hot 450 mL 2 M NaOH and the mixture boiled for 5 minutes. The clear-red solution was cooled down to 60 °C followed by addition of 12.2 g (30 mmol) of lead acetate in 50 mL

distilled water. Black PbS formed immediately and after 5 minutes of stirring, the PbS was Büchner filtered from the red filtrate which was cooled in a suction flask immersed in an ice/salt bath. Addition of 100 mL glacial acetic acid to the filtrate precipitated the yellow 4,4'-azodi(phenylcyanamide) (**7**) which was filtered, washed with water and dried. Recrystallization from 3:1 acetone/water solution yielded 3.2 g (78%) pure adpcH₂. IR: ν (NCN) 2238 cm⁻¹. ¹H NMR (300 MHz, DMSO - d₆) 10.5 (broad singlet, 2H); 7.89 (d, 4H); 7.14 (d, 4H) ppm.

3.2.4 Preparation of Tl₂adpc (**8**)

To the boiling solution of 0.52 g (2 mmol) adpcH₂ in 2:1 acetone/ water was added 60 mL 2:1 acetone/water solution of 1.06 g (4 mmol) TlNO₃ followed by 2 mL triethylamine. The reaction mixture was boiled for 5 minutes and then gradually chilled to -20 °C. Fine orange crystals of Tl₂adpc (**8**) were formed which was filtered, washed with water and acetone and finally dried. Yield: 0.8 g, 60%. IR: ν (NCN) 2035 cm⁻¹. ¹H-NMR (300 MHz, DMSO - d₆) δ : 7.41 (d, 4H); 6.60 (d, 4H) ppm.

3.2.5 Preparation of *cis*-bis(bipyridine)dichlororuthenium(II), [Ru(bpy)₂Cl₂] (**10**)

In order to prepare the precursor complex 6.11 g (0.04 mole) 2,2'-bpy was reacted with 5.1 g (0.02 mole) RuCl₃·3H₂O in 300 mL DMF under reflux condition for 3 hours. After chilling to room temperature the volume of the solution was reduced to approximately 100 mL using rotary evaporator. Crude product was then precipitated using 450 mL diethyl ether, filtered and dried overnight.

Recrystallization was performed by dissolving the crude product in 350 mL hot 1:1 ethanol/water solution, hot solution was filtered and to the still hot filtrate was added 45 g (1.1 mole) lithium chloride. The solution then boiled to reduce the volume to 200 mL and then cooled down overnight in the fridge. Dark green $[\text{Ru}(\text{bpy})_2\text{Cl}_2]$ (**10**) was filtered off the solution and washed with copious amount of water. Yield: 5.2 g, 56%. ^1H -NMR (300 MHz, $\text{DMSO} - d_6$): 9.98 (d, 2H); 8.65 (d, 2H); 8.50 (d, 2H); 8.07 (td, 2H); 7.77 (td, 2H); 7.68 (td, 2H); 7.52 (d, 2H); 7.10 (td, 2H) ppm.

3.2.6 Preparation of $[\{\text{Ru}(\text{bpy})_2\}_2(\mu\text{-adpc})_2] \cdot (\text{DMSO}) \cdot 3(\text{H}_2\text{O})$ (**11**)

0.65 g (1.0 mmol) Ti_2adpc and 0.46 g (0.95 mmol) $[\text{Ru}(\text{bpy})_2\text{Cl}_2]$ were refluxing in 30 mL DMF for 3 h. The reaction mixture cooled down to $-20\text{ }^\circ\text{C}$ and then filtered. Fine black precipitate was filtered off the solution, dissolved in 5 mL DMSO, filtered through $45\mu\text{m}$ Millipore (syringe filter) and recrystallized by acetone diffusion. Yield: 0.43 g, 64%. Anal. Calcd. for $\text{Ru}_2\text{C}_{70}\text{H}_{60}\text{O}_3\text{N}_{20}\text{S}$: C, 56.82; H, 4.09; N, 18.93. Found: C, 56.75; H, 3.93; N, 18.79. IR: $\nu(\text{NCN})$ 2161 cm^{-1} . ^1H -NMR (300 MHz, $\text{DMSO}-d_6$): 9.54 (d, 4H), 8.80 (d, 4H), 8.67 (d, 4H), 7.95 (t, 4H), 7.93 (m, 8H), 7.70 (d, 4H), 7.48 (d, 8H), 7.29 (t, 4H), 6.68 (d, 8H) ppm. ^{13}C -NMR (300 MHz, $\text{DMSO}-d_6$): 159.1; 157.8; 156.3; 152.8; 152.2; 144.6; 136.7; 135.8; 128.2; 127.2; 126.6; 123.7; 123.8; 119.7; 31.2.

3.2.7 Preparation of $[\{\text{Ru}(\text{bpy})_2(\text{dmsO})\}_2(\mu\text{-adpc})][\text{PF}_6]_2 \cdot 3\text{H}_2\text{O}$ (**12**)

0.2 g (0.15 mmol) $\{\text{Ru}(\text{bpy})_2\}_2(\mu\text{-adpc})_2$ was dissolved in 5 mL DMSO. 0.30 mmol HPF_6 in 20 mL DMSO was then added to the complex solution. The mixture was heated up to $100\text{-}110\text{ }^\circ\text{C}$ under inert atmosphere for 30 minutes. The hot DMSO mixture

filtered through frit and to the hot filtrate was added excess amount of NH_4PF_6 (0.5 g, 3 mmol). 40 mL distilled water was then used to precipitate the crude product. After cooling down to room temperature, the product was collected by suction filtration (0.12 g). The crude product was purified by chromatography. In a typical experiment 0.10 g of the crude complex was dissolved in 7 mL of 1:1 acetonitrile/toluene which was filtered and loaded onto a 30 cm x 3 cm chromatography column containing 150 g grade V alumina (Brockmann 1, weakly acidic, 150 mesh). One band containing mononuclear complex eluted first with 1:1 acetonitrile/toluene. The second band containing desired complex was eluted using 1:9 DMF/acetonitrile and the eluate evaporated to dryness using rotary evaporation. Residual was dissolved again in 10 mL acetonitrile and filtered through frit, evaporated to dryness and again was dissolved in 5 mL acetone which was then precipitated out using 40 mL diethyl ether. Yield: 22 mg (Yield of column: 22%, total yield: 12.3%). Anal. Calcd. for $\text{Ru}_2\text{C}_{54}\text{H}_{58}\text{N}_{14}\text{O}_5\text{S}_2\text{P}_2\text{F}_{12}$: C, 43.89; H, 3.68; N, 12.35. Found: C, 43.73; H, 3.27; N, 12.21. IR: $\nu(\text{NCN})$ 2171cm^{-1} , $\nu(\text{S}=\text{O})$ 1098cm^{-1} , $\nu(\text{Ru-S})$ 427cm^{-1} . $^1\text{H-NMR}$ (300 MHz, DMSO-d_6): 10.04 (d, 2H); 9.18 (d, 2H); 8.85 (m, 8H); 8.74 (d, 2H); 8.45 (t, 2H); 8.36 (t, 2H); 8.18 (t, 2H); 8.10 (t, 2H); 8.49 (q, 4H); 7.92 (d, 2H); 7.52 (t, 2H); 7.45 (t, 2H); 7.35 (d, 4H); 7.26 (d, 2H); 6.20 (d, 4H); 3.22 (s, 6H); 2.26 (s, 6H) ppm.

3.3 Physical Measurements

3.3.1 Electrochemistry

Cyclic voltammetry studies were performed using Metrohm Autolab potentiostat/galvanostat PGSTAT30 as described before.

N,N-Dimethylformamide (DMF) and Dimethyl sulfoxide (DMSO) (Sigma-Aldrich, Chromosolv®Plus, 99.9%, HPLC grade) were used as solvents for the studies. As an internal reference cobaltocenium hexafluorophosphate ($E^{\circ} = -0.589$ V versus NHE)³⁴ was used.

3.3.2 Infrared, Electronic Absorption and NMR Spectroscopies.

In order to record infrared absorption spectra KBr disk of each compound was placed in sample holder part of Bomem Michelson 120 FTIR spectrometer which were corrected for air background.

Electronic absorption spectra were taken using a Cary 3 spectrophotometer as described before.

¹H NMR spectra were recorded using Bruker 300 Ultra Shield spectrometers and all the peaks were referenced to TMS at 0.00 ppm. 5-10 mg of sample in 1 mL DMSO-d₆ was used to record the chemical shifts.

3.3.3 Vis-NIR and IR Spectroelectrochemistry

Vis-NIR and IR-spectroelectrochemistry were performed using an optical transparent thin-layer electrochemical cell. 0.1M TBAH solution in DMF was used as supporting electrolyte and solvent. Applied potential was in the range of -0.1 and 1.3 V during the experiment. The Vis-NIR spectra were collected on a UV-Vis-NIR Cary 5 spectrophotometer with appropriate background correction of solvent and electrolyte at a scan rate of 1800 nm/min and IR spectra were collected on the same Bomem Michelson 120 FTIR spectrometer as used for IR-spectroscopy.

3.3.4 Elemental Analyses:

All elemental analyses were performed by Canadian Microanalytical Services, Ltd. in Delta, B. C., Canada.

3.3.5 DFT Calculations:

Gas-phase hybrid HF-DFT SCF calculations of equilibrium geometry, MOs, orbital energies and spin density distributions were performed with Wavefunction Inc., Spartan' 14 Parallel program package, using the B3LYP/6-31G* model.

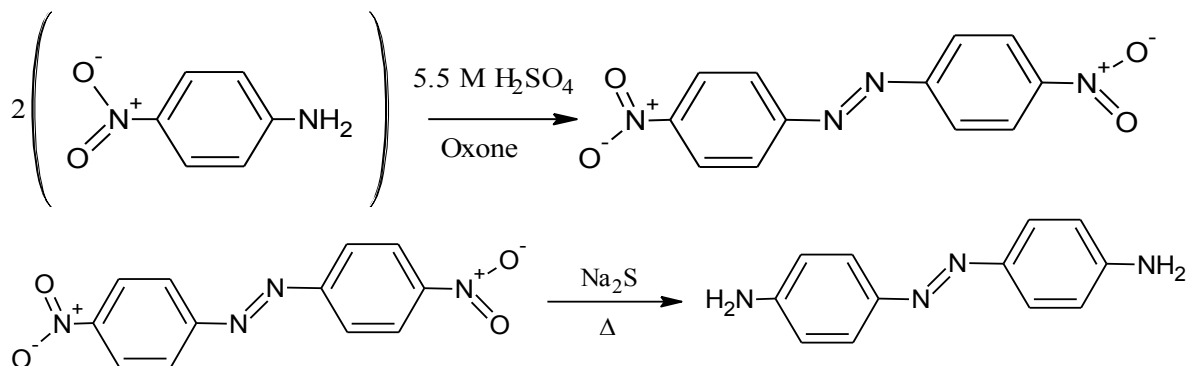
3.4 Results and Discussions:

3.4.1 Synthesis of Ligand

4,4'-Azodianiline was synthesized via condensation reaction of nitroso compounds. The oxidation of the aromatic amine achieved by using Oxone[®] (potassium peroxomonosulphate) in aqueous acidic solution led to the less water soluble nitrosoarene. Azocoupling reaction resulted in desired 4,4'-azodi(nitrobenzene) which was recrystallized from acetic acid to yield 71% pure product. Experiments showed the yield of the reaction increases by slow addition of the oxidizing agent.

In the next step of completing the anticipated azodianiline the nitro groups of azodi(nitrobenzene) reduced to amine groups using sodium sulfide in ethanol/water solution at refluxing temperature. The pure product was crystallized directly from the reaction mixture in 61% overall yield.

Scheme 6 Synthesis of 4,4'-Azodianiline

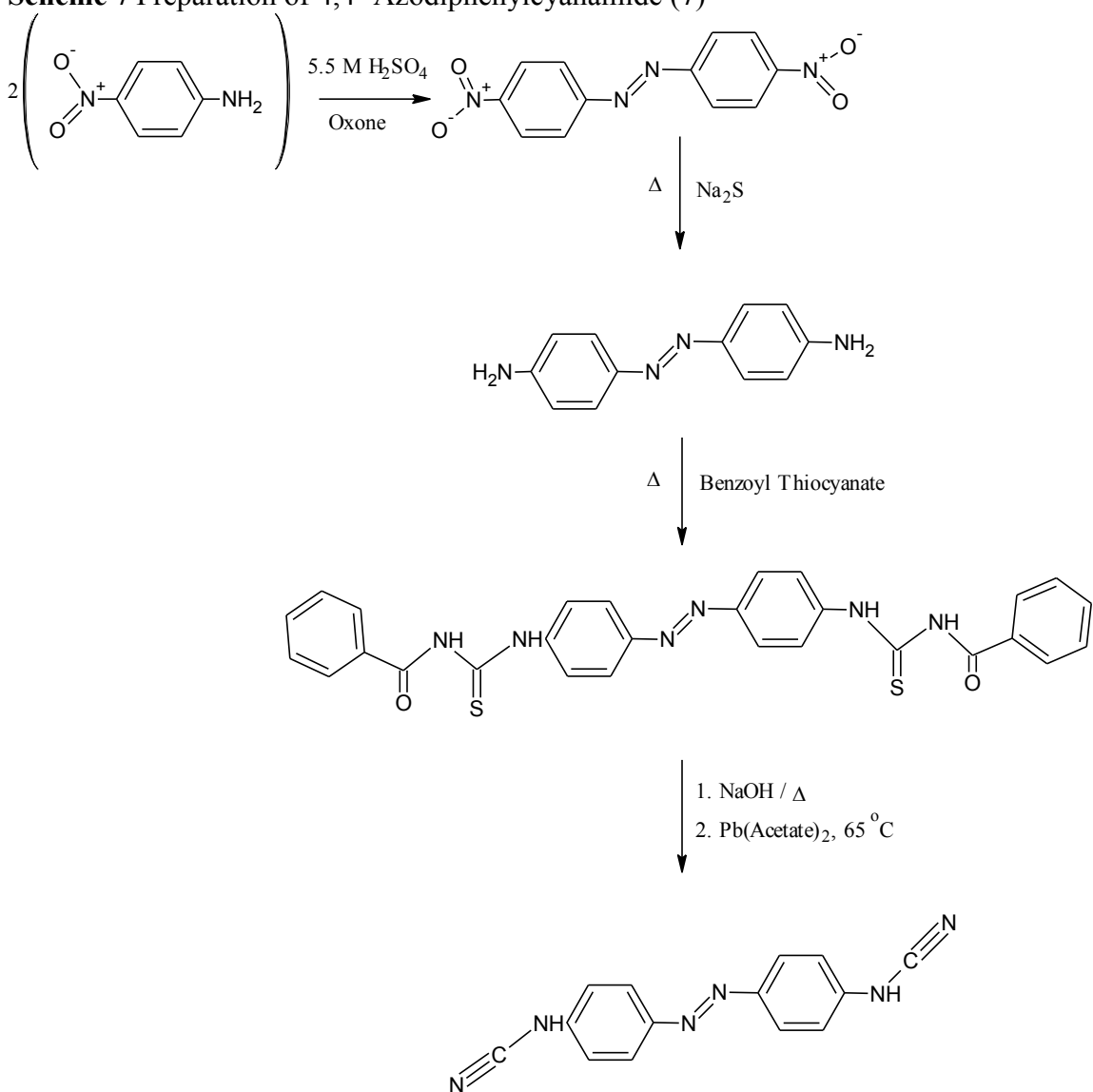


The azodi(phenylcyanamide) ligand (7) was synthesized via thiourea procedure from corresponding aniline derivative (Scheme 7). This method consists of the synthesis of benzoyl thiocyanate from the reaction of ammonium thiocyanate with benzoyl chloride in refluxing acetone solution which results pale green solution with white precipitate. Addition of an aniline derivative to the reaction mixture results in nucleophilic addition of amine group to the carbonyl of benzoyl thiocyanate. The formed thiourea derivative undergoes base hydrolysis by boiling in 2 M NaOH(aq) solution followed by desulfurization at 65 °C by lead acetate precipitating black PbS. Finally acidification of the aqueous solution with glacial acetic acid yielded a protonated phenylcyanamide derivative. Several experimental steps have to be estimated during this procedure such as (1) the duration of the reaction between benzoylthiocyanate and aniline derivative depends on the nature of the phenyl ring substituents. It has been shown for highly deactivated amines excess amount of benzoylthiocyanate is needed as well as longer refluxing time. (2) Desulfurization step has to be done at temperature not greater than

65°C to prevent dimerization. And finally (3) acidification step should be done as fast as possible to prevent the formation of a guanidine derivative.²²

In order to increase the reactivity of the prepared ligand, its thallium salt (**8**) was synthesized in acetone/water solution by reacting thallium acetate salt with neutral adpcH₂ (**7**) in presence of triethylamine as deprotonating agent.

Scheme 7 Preparation of 4,4'-Azodiphenylcyanamide (**7**)

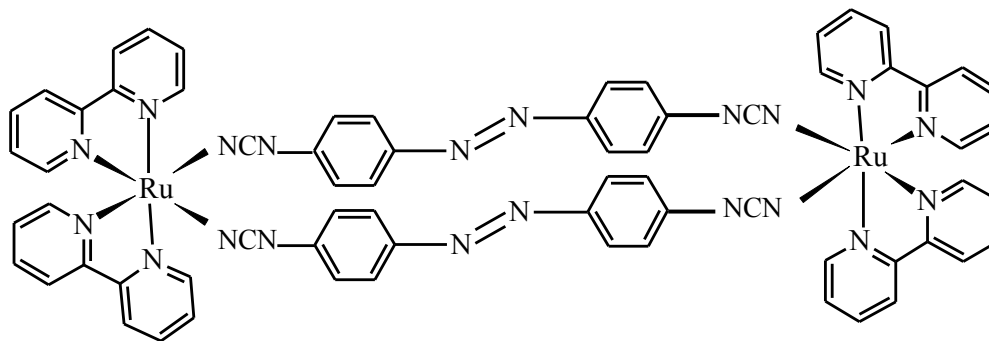


3.4.2 Synthesis of complexes:

Precursor cis-[Ru(bpy)₂Cl₂] complex (10) was synthesized through the reaction of two equivalent bipyridine with an equivalent RuCl₃ in DMF. After 3 hours of reflux the crude product stirred in a hot solution of lithium chloride in ethanol/water, which after chilling down resulted in pure micro crystalline desired complex.

[{Ru(bpy)₂}₂(μ-adpc)₂] complex (11). Synthesis of this complex was a slight challenge in terms of reaction duration as the reaction mixture made of refluxing one equivalent thallium salt of adpc²⁻ ligand with one equivalent of pre-made cis-[Ru(bpy)₂Cl₂] (**10**) in DMF has the potential of producing less soluble multi-nuclear complexes which have almost the same ¹H-NMR spectra as the desired complex. Refluxing time longer than 3 hours of Tl₂adpc (**8**) with Ru(bpy)₂Cl₂ (**10**) caused thick layer of black precipitate at the bottom of reaction flask which was just slightly soluble in hot DMSO while the desired dinuclear complex was soluble in DMF and DMSO.

After 3 hours refluxing the reaction mixture and chilling down to -20 °C the solution was filtered, black fine precipitate on the filter was collected, which was the mixture of TlCl (thallium chloride) salt and the desired product. Purification of the product achieved by dissolving the mixture in hot DMSO followed by filtration using Millipore filters and finally recrystallizing the ruthenium complex (**11**) with acetone diffusion in to DMSO solution.



3.4.3 Infrared Spectroscopy:

One of the best spectroscopic methods to show the presence of cyanamide functional group in a compound is the vibration of NCN bond in infrared region. In the present research the infrared spectra of adpcH₂ (**7**), Tl₂adpc (**8**) and the dinuclear [$\{\text{Ru}(\text{bpy})_2\}_2(\mu\text{-adpc})_2$] (**11**) complex were taken on KBr pellets. The corresponding IR-spectra are shown in Figure 31 to Figure 33. The vibration of NCN band appears at 2238, 2035 and 2161 cm⁻¹ for adpcH₂ (**7**), Tl₂adpc (**8**) and the [$\{\text{Ru}(\text{bpy})_2\}_2(\mu\text{-adpc})_2$] (**11**) complex, respectively.

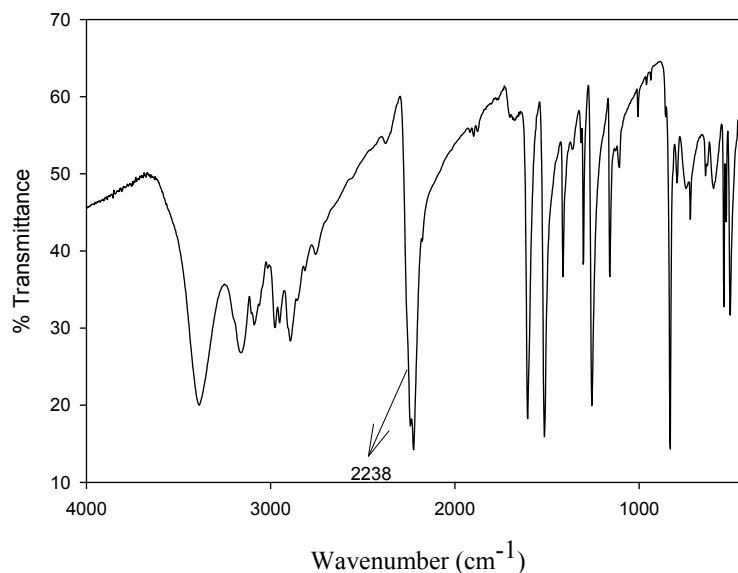


Figure 31 IR spectrum of adpcH₂ (**7**) (KBr disc).

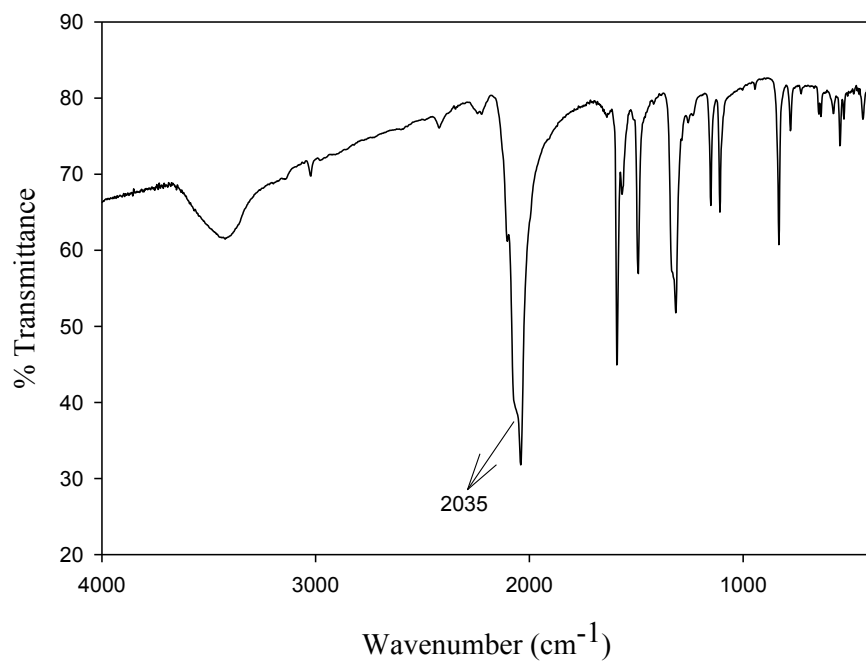


Figure 32 IR spectrum of Tl₂adpc (**8**) salt (KBr disc).

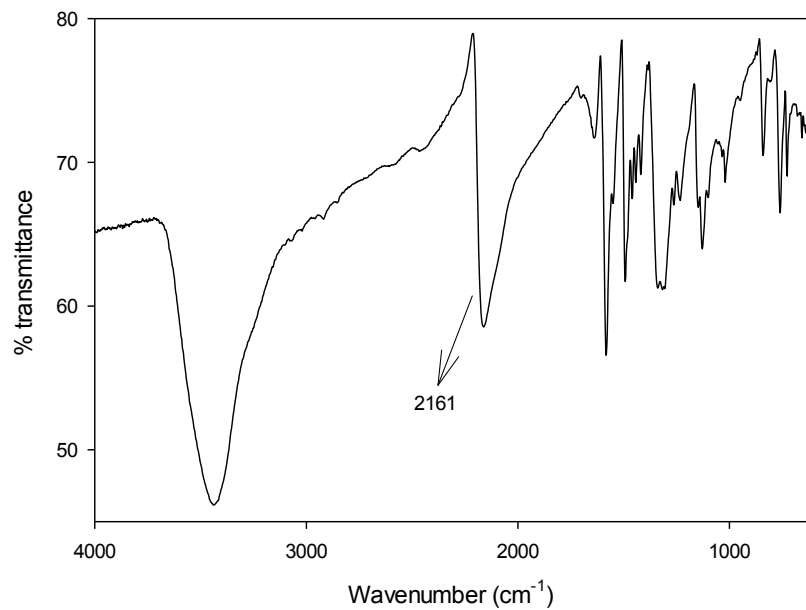


Figure 33 IR spectrum of [{Ru(bpy)₂ }₂(μ-adpc)₂] (**11**) complex (KBr disc).

As was described before in section 1.3.1, different resonance structures of cyanamide group are responsible for the differences in $\nu(\text{NCN})$. In the neutral form of the ligand the resonance structure A in Figure 3 is the dominant form as for dianion form of the ligand in Tl_2adpc form B is the major structure.

3.4.4 $^1\text{H-NMR}$ spectroscopy

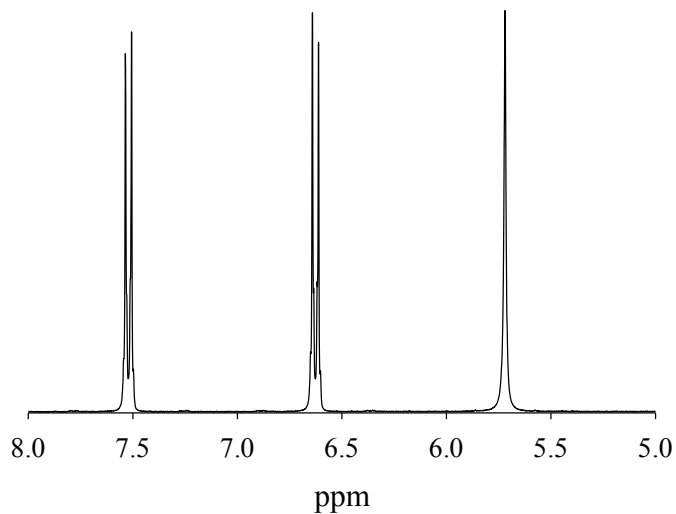
$^1\text{H-NMR}$ spectra of azodianiline, adpcH_2 (**7**), Tl_2adpc (**8**), $[\text{Ru}(\text{bpy})_2\text{Cl}_2]$ (**10**) and $[\{\text{Ru}(\text{bpy})_2\}_2(\mu\text{-adpc})_2]$ (**11**) were all recorded in DMSO-d_6 with TMS as reference. The chemical shifts and integrations are listed in Table 5 also the spectra for all the products are shown in Figure 34 to Figure 38. $^1\text{H-NMR}$ of adpcH_2 and its thallium salt have been previously reported¹⁴ and were replicated in the present work.

The bipyridine ligands in $\text{cis-}[\text{Ru}(\text{bpy})_2\text{Cl}_2]$ (**10**) complex (Figure 37) have two magnetically non-equivalent pyridine moieties and therefore display 8 total proton peaks including two sets of two doublets and two sets of two triplets within the chemical shifts from 7.1 to 10 ppm. For the $[\{\text{Ru}(\text{bpy})_2\}_2(\mu\text{-adpc})_2]$ (**11**) complex chemical shifts of bipyridine ligands have almost the same pattern as its precursor complex. $^1\text{H-NMR}$ spectrum (Figure 38) shows two magnetically non-equivalent pyridine moieties as 8 peaks in total for bipyridines and two doublets for two groups of different protons in adpc^{2-} bridging ligands.

$^1\text{H-NMR}$ peaks for complexes 10 and 11 have been assigned to the representative protons and are provided in parts B5 and B6 in the Appendix B.

Table 5 300 MHz ^1H NMR Data in $\text{DMSO-}d_6$.

Compound	Chemical shifts(ppm)/type
4,4'-Azodianiline	7.53 (d, 4H); 6.63 (d, 4H) 5.72 (s, 4H)
adpcH ₂ (7)	10.5 (broad s, 2H) 7.89 (d, 4H); 7.14 (d, 4H)
Tl ₂ adpc (8)	7.41 (d, 4H); 6.60 (d, 4H)
cis-[Ru(bpy) ₂ Cl ₂] (10)	9.98 (d, 2H) 8.65 (d, 2H) 8.50 (d, 2H) 8.07 (td, 2H) 7.77 (td, 2H) 7.68 (td, 2H) 7.52 (d, 2H) 7.10 (td, 2H)
[{Ru(bpy) ₂ } ₂ (μ -adpc) ₂] (11)	9.54 (d, 4H); 8.80 (d, 4H) 8.67 (d, 4H); 7.95 (t, 4H) 7.93 (m, 8H); 7.70 (d, 4H) 7.48 (d, 8H); 7.29 (t, 4H) 6.68 (d, 8H)

**Figure 34** ^1H -NMR of 4,4'-azodianiline in $\text{DMSO-}d_6$.

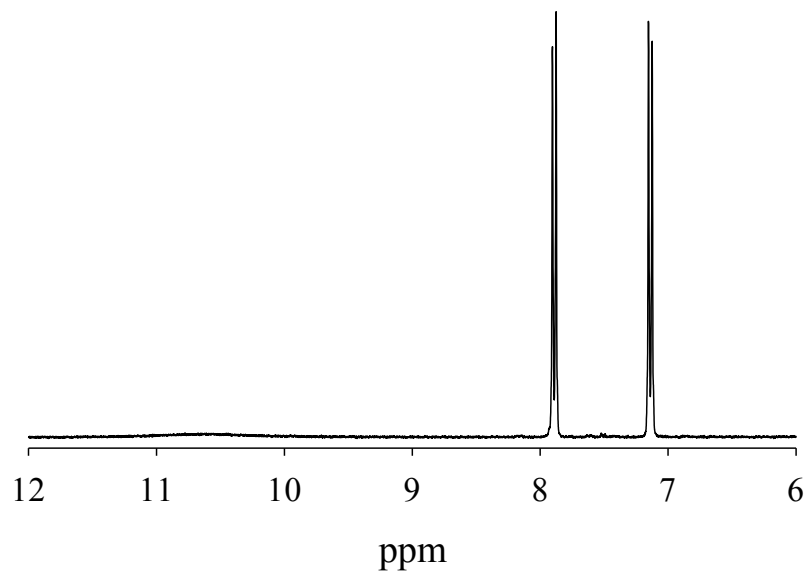


Figure 35 $^1\text{H-NMR}$ of adpcH_2 (**7**) in DMSO-d_6 .

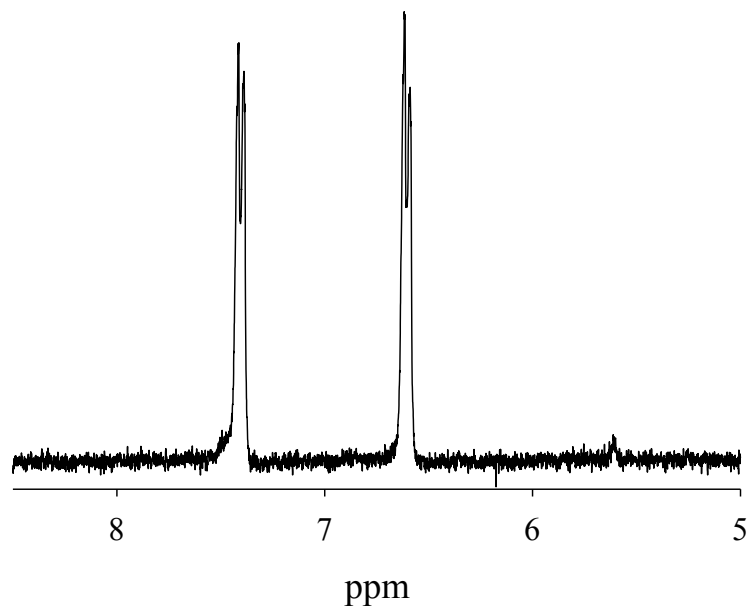


Figure 36 $^1\text{H-NMR}$ of Tl_2adpc (**8**) in DMSO-d_6 .

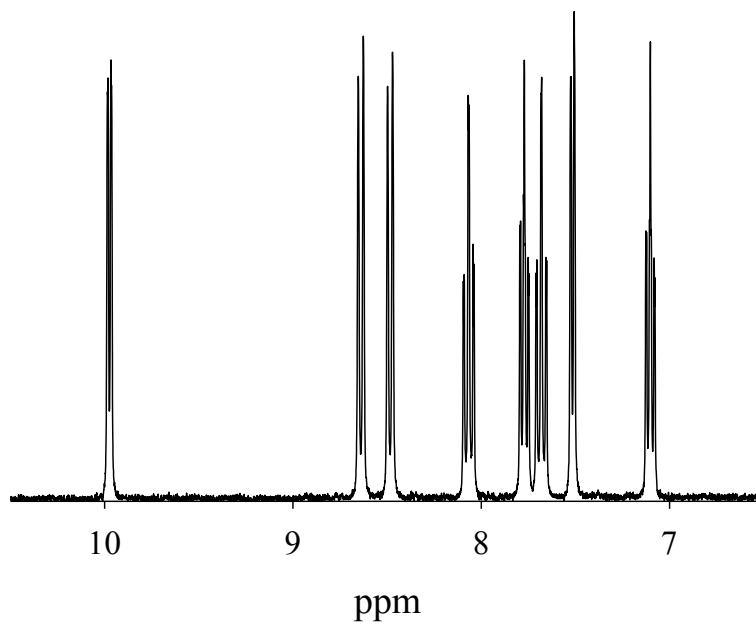


Figure 37 $^1\text{H-NMR}$ of $\text{cis-}[\text{Ru}(\text{bpy})_2\text{Cl}_2]$ (**10**) in DMSO-d_6 .

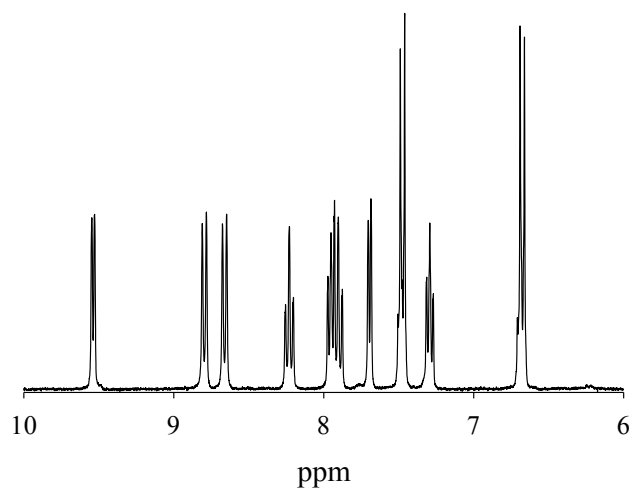


Figure 38 $^1\text{H-NMR}$ of $[\{\text{Ru}(\text{bpy})_2\}_2(\mu\text{-adpc})_2]$ (**11**) in DMSO-d_6 .

3.4.5 Electrochemistry

The CV of [$\{\text{Ru}(\text{bpy})_2\}_2(\mu\text{-adpc})_2$] (**11**) was performed in DMF at the scan rate of 0.1 V/sec. The voltammogram is shown in Figure 39. CV data for Tl_2adpc (**8**) and the dinuclear complex are tabulated in Table 6. As previous studies showed, the CV of $\text{Tl}_2[\text{adpc}]$ (**8**) has two closely spaced redox couples which are only partially reversible.¹⁴ The voltammogram of [$\{\text{Ru}(\text{bpy})_2\}_2(\mu\text{-adpc})_2$] (**11**) in DMF shows two oxidation waves at 0.64 and 0.77 V versus NHE which we assigned to Ru(III/II). The other peak representing two electron process at 0.93 V was assigned to adpc(1-/2-) oxidation. The assignments of couples determined by combined IR and vis-NIR spectroelectrochemical analysis as well as theoretical calculations on oxidized dinuclear complexes.

The Ru(III/II) couples of (**11**) are reversible and the separations between cathodic and anodic waves are 59 mV and 61 mV for a scan rate of 0.1 V/sec. As $K_C = 10^{16.91 \Delta E}$ and $\Delta E=130$ mV the comproportionation equilibrium constant for [$\{\text{Ru}(\text{bpy})_2\}_2(\mu\text{-adpc})_2$] (**11**) complex was calculated to be $K_c = 1.6 \times 10^2$. This low K_c value implies a weak metal-metal coupling in the mixed-valence complex.

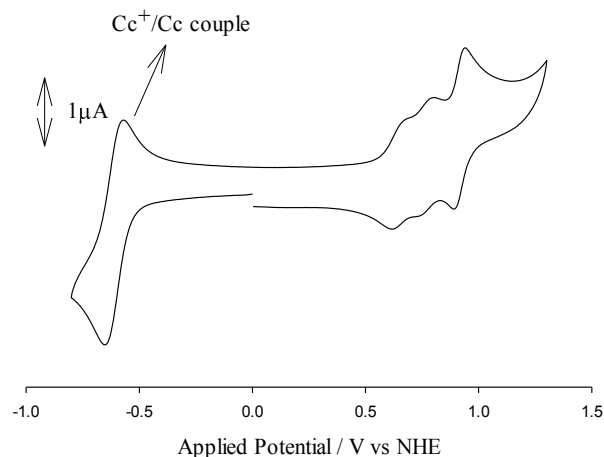


Figure 39 Cyclic voltammogram [$\{\text{Ru}(\text{bpy})_2\}_2(\mu\text{-adpc})_2$] in DMF with 0.1 M tetrabutylammonium hexafluorophosphate, using platinum counter and working electrode, silver wire pseudo-reference (cobaltocene internal reference, Cc/Cc^+) at scan rate of 100mV/s vs. NHE.

Table 6 Electrochemical^a Results for dianion adpc and its dinuclear ruthenium complex.

Compound	Ru(III/II)	L(-1/-2)	L(0/-1)
$[\text{AsPh}_4]_2[\text{adpc}]^{14}$		0.48 ^b	0.63 ^b
$[\{\text{Ru}(\text{bpy})\}_2(\mu\text{-adpc})_2]^{\text{b}}$ (11)	0.64, 0.77	0.93	

^ain Volts vs NHE at ambient temperature (23°C) and a scan rate 0.1 V/s; 0.1 M TBAH electrolyte; using platinum counter and working electrode, silver wire pseudo-reference; cobaltocenium hexafluorophosphate ($E^\circ = -0.589\text{V}$ versus NHE)⁵¹ was used as internal reference; ^bin DMF.

3.4.6 Electronic Absorption Spectroscopy

The quantitative electronic absorption spectra of Ti_2adpc (**8**) and $[\{\text{Ru}(\text{bpy})\}_2(\mu\text{-adpc})_2]$ (**11**) in DMF are shown in Figure 40 and Figure 41 respectively and also tabulated in Table 7. The anionic ligand in DMF shows a strong visible absorption in the case of adpc^{2-} which has been assigned to a cyanamide-to-azo group intra-ligand charge

transfer (ILCT).¹⁴ Upon the coordination of adpc^{2-} to Ru(II) metal centre this ILCT band is present and overlaps in energy with metal-to-ligand charge transfer (MLCT) of Ru(II)-bpy chromophores.

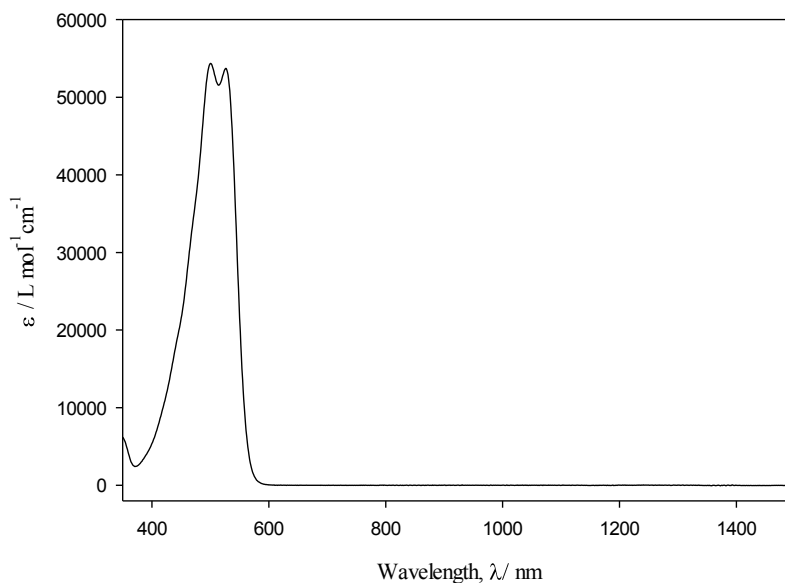


Figure 40 Electronic absorption spectrum of Ti_2adpc (8) in DMF.

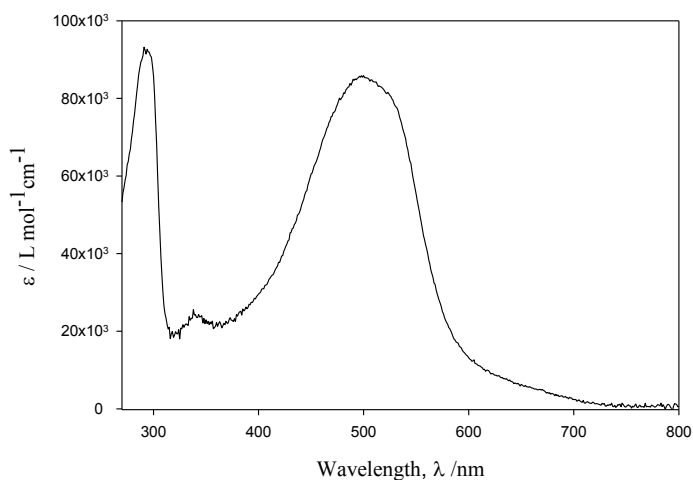


Figure 41 Electronic absorption spectrum of $[\text{Ru}(\text{bpy})_2]_2(\mu\text{-adpc})_2$ (11) in DMF.

Table 7 Quantitative Electronic Absorption Spectral Data of Dianion adpc and its Dinuclear Complexes in DMF.

Compound	Absorptions ($\epsilon / M^{-1}cm^{-1}$)
(8) ¹⁴	500 (54400), 525 (51500) (NCN \rightarrow Azo ILCT)
(11)	290(92900) ($\pi \rightarrow \pi^*$ bpy) 340(24500), 500(85700) (ILCT, Ru(II)- bpy & Ru(II)- trpy)
(9) ¹⁴	293 (81900), ($\pi \rightarrow \pi^*$ bpy, terpyrine & phenyl) 317 (72100), 490 (69100), (ILCT, Ru(II)- bpy & Ru(II)- trpy) ¹⁴

3.4.7 Vis-NIR Spectroelectrochemistry

The Vis-NIR spectroelectrochemistry of the [Ru(II), Ru(II)] (**11**) complex in DMF generating the [Ru(III), Ru(II)] and [Ru(III), Ru(III)] spectra are shown in Figure 42.

For one electron oxidation product of [$\{Ru(bpy)\}_2(\mu\text{-adpc})_2$] (**11**) which was performed in an electrical range between 0.0 - 0.55 V (vs Ag/AgCl reference electrode), three new bands at $\lambda_{\text{max}} = 654, 830$ and 1930 nm appear in the visible near-IR region (part A Figure 42). Assignment of the band at 830 nm is given to the Ru (III)-cyanamide chromophore as it shows gain of absorptivity with the formation of the [R(III), Ru(III)] complex. The band at 654 nm has been assigned to a Ru(II) \rightarrow adpc MLCT transition nm as decreases in intensity with the formation of completely oxidized [Ru(III), Ru(III)].¹⁴ The absorption centered at 1930 nm which is not present in the spectra of the [Ru(II), Ru(II)] and [Ru(III), Ru(III)] is assigned to a Ru(II)-Ru(III) metal-to-metal charge transfer (MMCT). Further oxidation of this complex (electrical potential range between 0.55 – 0.65V vs. Ag/AgCl reference electrode) results in intensity decrease of

the previously generated peak at 1930 nm and the generation of another peak at 1353 nm which is associated with Ru(III)-Ru(III) ligand-to-metal charge transfer (LMCT) (part B Figure 42). Further oxidation of the complex results in a loss of reversibility.

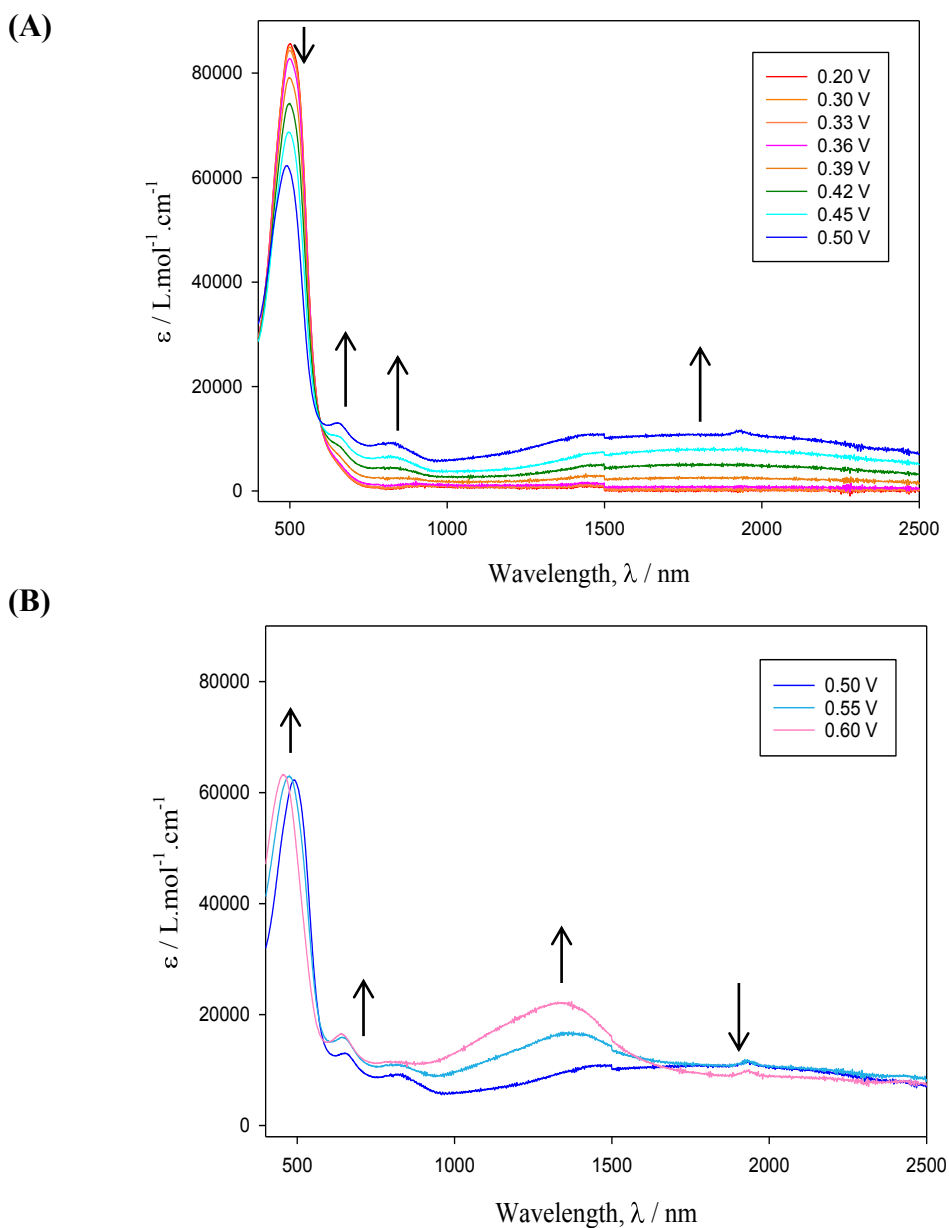


Figure 42 OTTLE cell electronic spectra of $[\{\text{Ru}(\text{bpy})\}_2(\mu\text{-adpc})_2]$ in DMF under increasing oxidation potentials (0.0 \rightarrow 0.65 V). 0.1 M TBAH; ITO (indium-tin oxide)

coated glass served as working and counter electrodes; Ag/AgCl reference electrode(A)0.0 - 0.50 V; (B) 0.5-0.55 V; (C) 0.55-0.65 V.

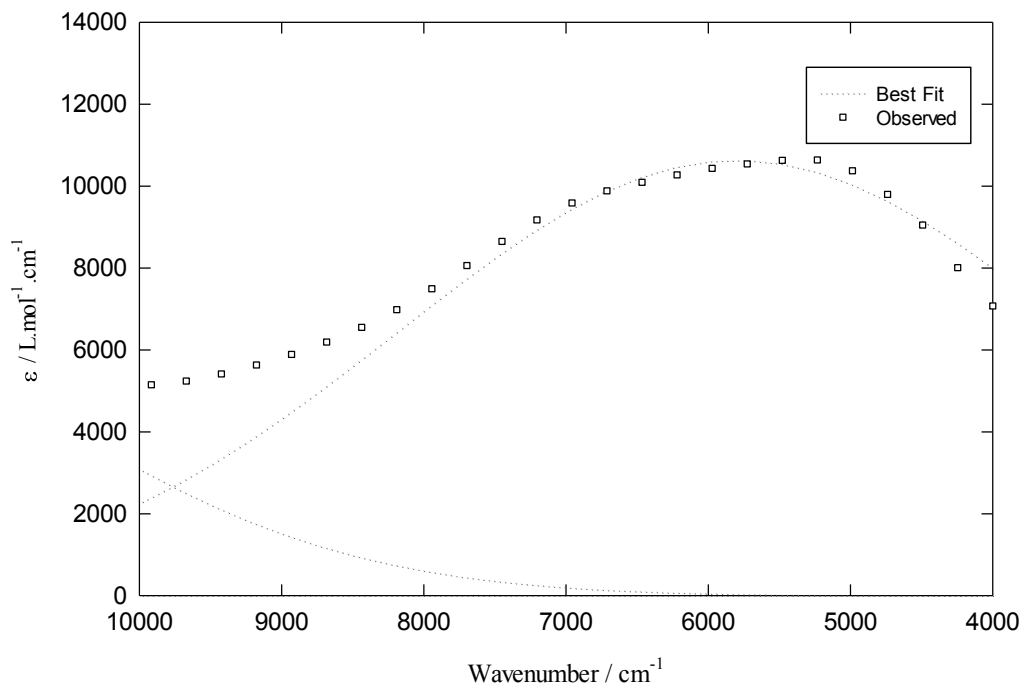


Figure 43 Metal-metal charge transfer band of [$\{\text{Ru}(\text{bpy})\}_2(\mu\text{-adpc})_2$] in DMF, smoothed data.

MMCT band plotted against an energy axis has been presented in Figure 43 in which the characteristic of Class (III) mixed-valence complexes such as non-Gaussian shape with high energy tail have been revealed⁵⁰. [$\{\text{Ru}(\text{bpy})\}_2(\mu\text{-adpc})_2$] complex possesses λ_{max} , ϵ_{max} and $\Delta\nu_{1/2}$ equal to 1846 nm, 10363 $\text{M}^{-1}.\text{cm}^{-1}$ and 4500 cm^{-1} , respectively.

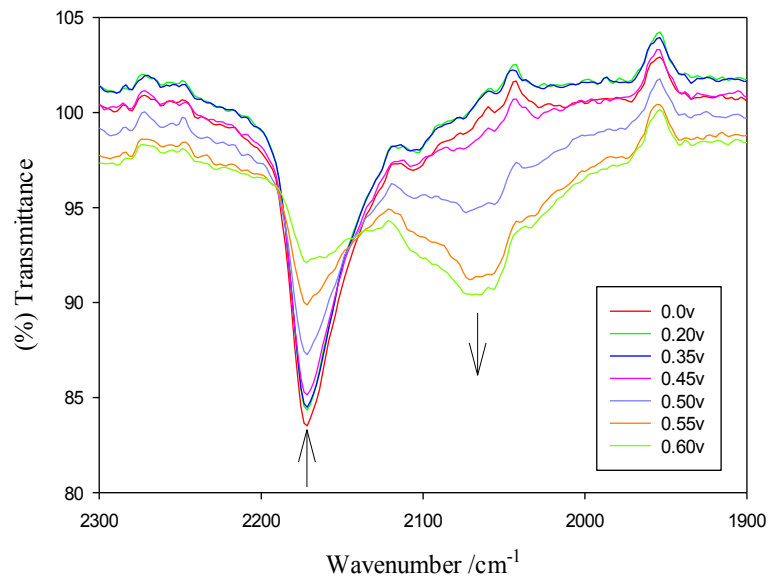
3.4.8 IR Spectroelectrochemistry

As stated before cyanamide group possesses two different resonance forms which are in contribution with the oxidation state and the coordination sphere of the complex.

Two different oxidation states ($2+$ and π -acid $3+$) of ruthenium perturb the resonance form of cyanamide ligand (see Figure 3) which can be recognized via IR-spectroelectrochemistry methods.

From the spectra, the oxidation of [$\{\text{Ru}(\text{bpy})\}_2(\mu\text{-adpc})_2$] (**11**) to form [$\{\text{Ru}(\text{bpy})\}_2(\mu\text{-adpc})_2$] $^{1+}$ resulted in a gradual decrease of intensity of the $\nu(\text{NCN})$ at 2170 cm^{-1} and small increase of intensity in lower and higher energy tails. The growth of the band at 2260 cm^{-1} is associated with the resonance form A in Figure 3 which is due to the formation of Ru(III) species. Further oxidation to generate [$\{\text{Ru}(\text{bpy})\}_2(\mu\text{-adpc})_2$] $^{2+}$ accompanied by less dramatic decrease of the peak at 2170 cm^{-1} and increase of the peak at 2060 cm^{-1} which might be due to anionic cyanamide bound to Ru(III) centre. Generally, good reversibility was observed for single electron oxidation, while the second oxidation is not very reversible (80 - 90% recovery of the initial spectrum). The observation of two $\nu(\text{NCN})$ bands for [$\{\text{Ru}(\text{bpy})\}_2(\mu\text{-adpc})_2$] $^{1+}$ arises from two cyanamide coordination environments, one bonded to Ru(III) and the other to Ru(II). This is consistent with a Class II mixed-valence state.

(A)



(B)

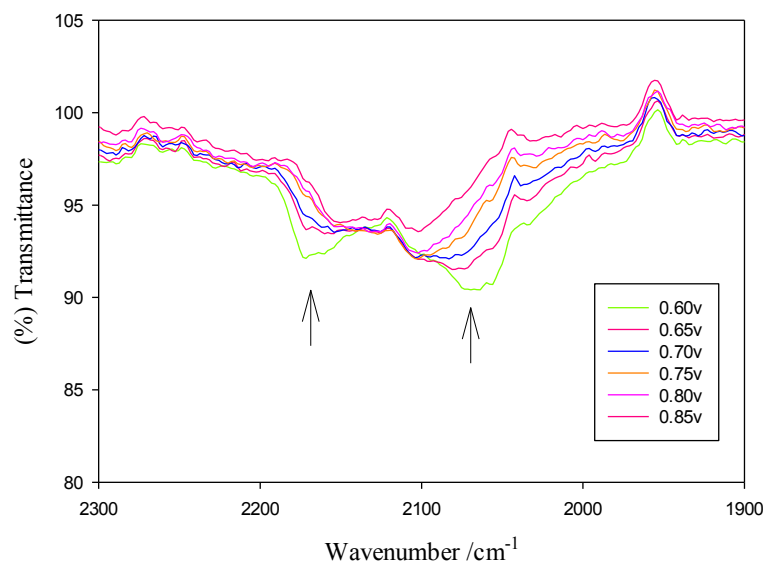


Figure 44 IR spectroelectrochemical oxidation of $[\text{Ru}(\text{bpy})_2(\mu\text{-adpc})_2]$ to form $[\text{Ru}(\text{bpy})_2(\mu\text{-adpc})_2]^+$ and $[\text{Ru}(\text{bpy})_2(\mu\text{-adpc})_2]^{2+}$ in DMF, 0.1 M TBAH. 0.0 - 0.85 V vs. Ag / AgCl.

3.4.9 DFT Calculation of Neutral and Singly Oxidized $[\{\text{Ru}(\text{bpy})\}_2(\mu\text{-adpc})_2]$ Complex

Theoretical DFT calculation of frontier molecular orbitals of $[\{\text{Ru}(\text{bpy})\}_2(\mu\text{-adpc})_2]$ (**11**) complex was performed using the B3LYP/6-31G* model and has been shown in Figure 45.

As seen for this complex the HOMO is mostly bridge-based with small contribution to ruthenium ($d\pi$) orbitals and two degenerated LUMO are based on bipyridine π^* orbitals as expected for π -acceptor ligands which helps stabilizing filled $d\pi$ orbitals of Ru(II) metal centre.

The DFT calculation of the spin density distribution in the mixed-valence $[\{\text{Ru}(\text{bpy})\}_2(\mu\text{-adpc})_2]^+$ is shown in Figure 46 in which spin density resides in $p\pi$ atomic orbitals of the bridging ligands with $d\pi$ orbital contributions from the ruthenium ion.

Comparison of the spin density calculated for $[\{\text{Ru}(\text{bpy})\}_2(\mu\text{-adpc})_2]^+$ with that of a similar calculation for $[\{\text{Ru}(\text{tpy})(\text{bpy})\}_2(\mu\text{-adpc})]^{3+}$, Figure 47, shows decrease of metal's $d\pi$ contribution for the latter complex. This is consistent with the Ru(III) oxidation state being better stabilized when two cyanamide anion ligands are coordinated.

However, based on these calculations alone, for $[\{\text{Ru}(\text{bpy})\}_2(\mu\text{-adpc})_2]^+$, a radical bridging ligand is predicted for the mixed-valence state in disagreement with IR spectroelectrochemistry which shows two $\nu(\text{NCN})$. It is suggested that the level of theory used is inadequate and that a more sophisticated treatment involving solvent interactions is required. Previous studies have shown this to be extremely important.²⁹

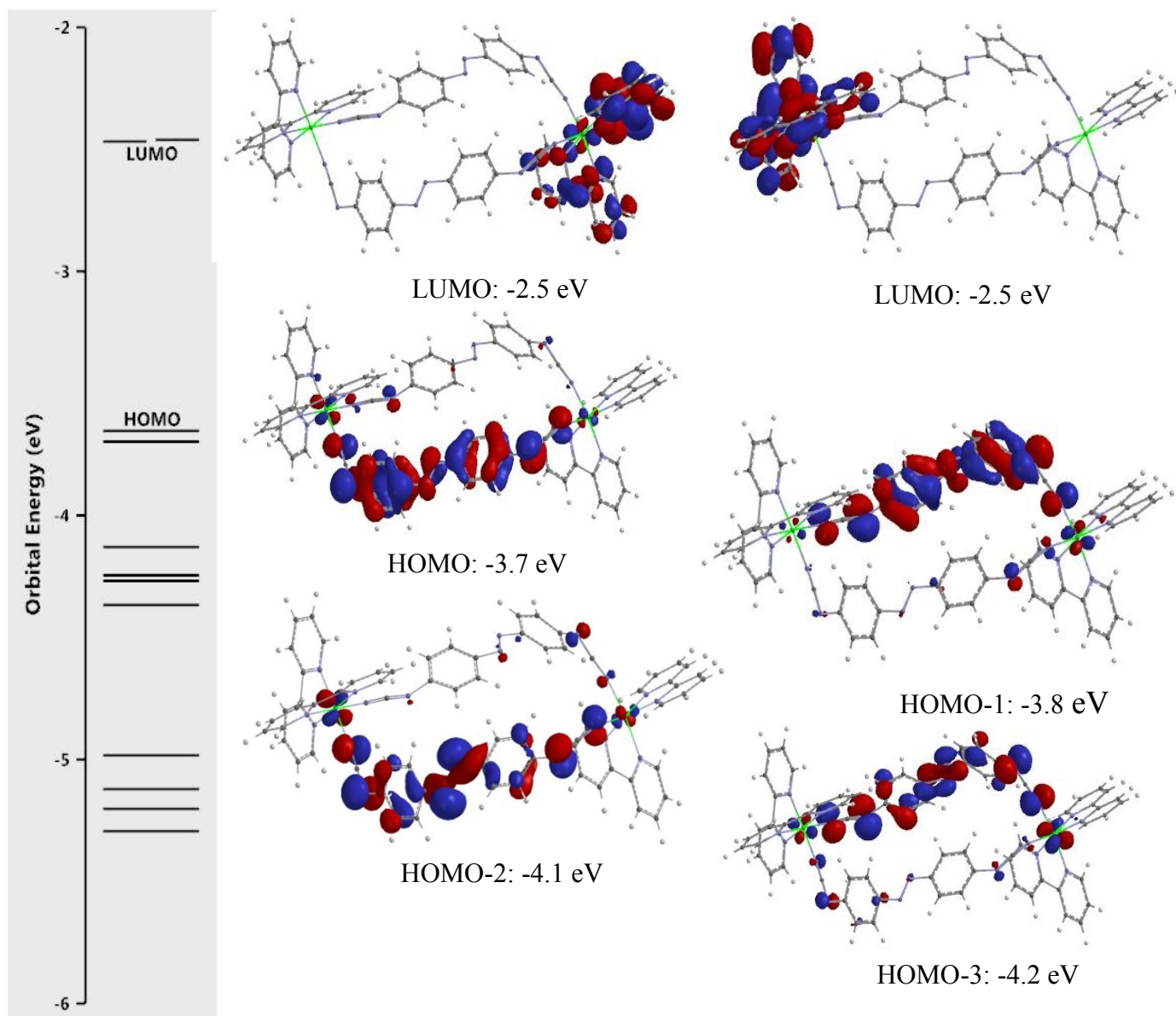


Figure 45 DFT calculation of orbital energies and selected molecular orbitals of $[\{\text{Ru}(\text{bpy})\}_2(\mu\text{-adpc})_2]$ (**11**).

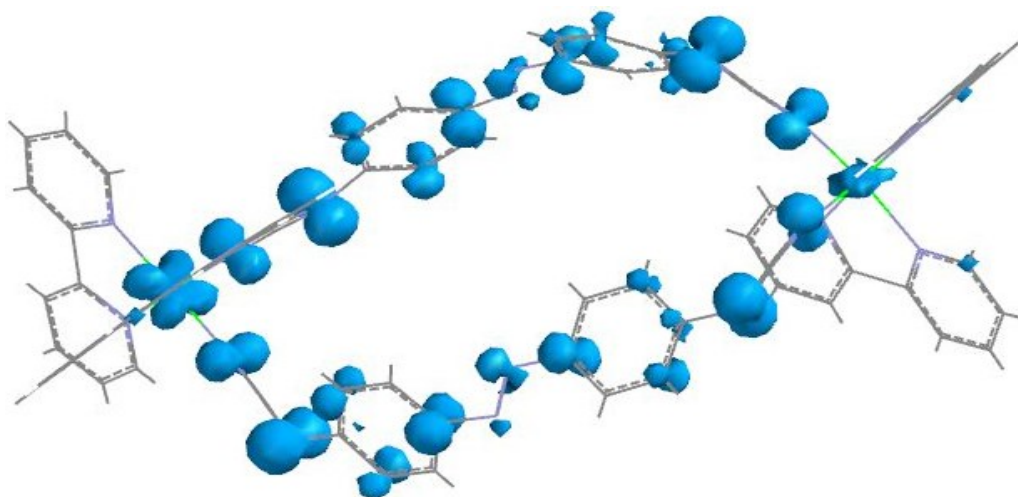


Figure 46 Spin density distribution of $[\{Ru(bpy)_2\}_2(\mu\text{-adpc})_2]^+$.

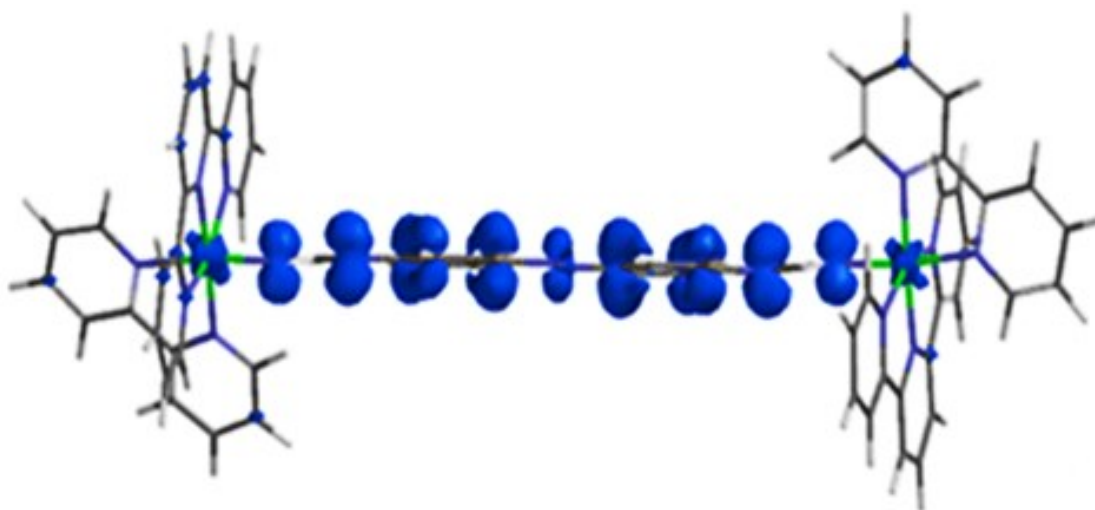
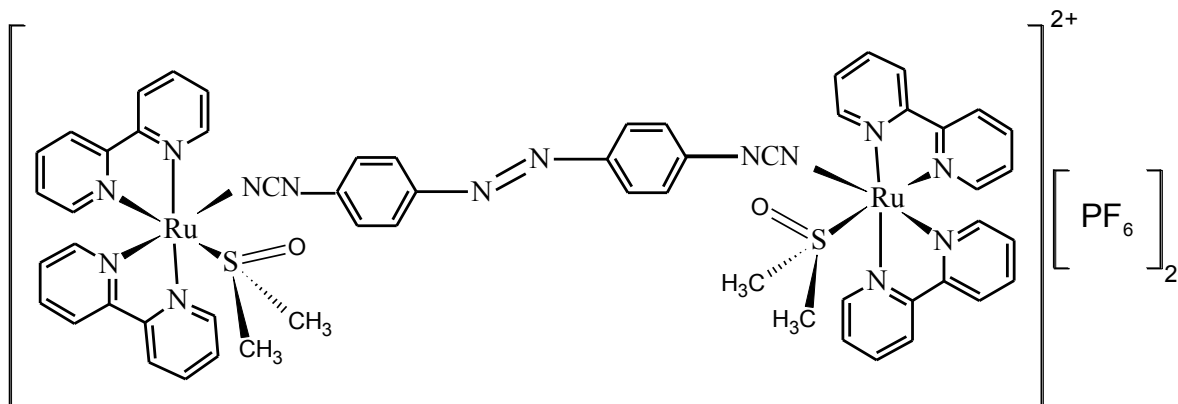


Figure 47 Spin density distribution of $[\{Ru(tpy)(bpy)\}_2(\mu\text{-adpc})]^{3+}$.⁵¹

3.5 Results and Discussion of dinuclear $[\{\text{Ru}(\text{bpy})_2(\text{dms})\}_2(\mu\text{-adpc})][\text{PF}_6]_2$ complex:

3.5.1 Synthesis

$[\{\text{Ru}(\text{bpy})_2(\text{dms})\}_2(\mu\text{-adpc})][\text{PF}_6]_2$ (**12**) complex was synthesized by refluxing the precursor $[\{\text{Ru}(\text{bpy})_2\}_2(\mu\text{-adpc})_2]$ (**11**) complex in slightly acidic DMSO solution under inert atmosphere. Experiments have shown longer reflux time or higher temperatures even during solvent removal (drying time) results in substitution of both adpc^{2-} ligands by dms .⁴⁶ In order to obtain elementally pure complex from crude mixture of mononuclear and dinuclear complexes, purification was achieved by using deactivated grade (V) alumina column. To prevent undesired linkage isomerism and binding to alumina the purification step was performed in dark. The desired product was eluted from the column by 1:9 DMF/acetonitrile solvent. Higher polarity of solvent decreased the elution time but increased the amount of impurity in the final product. The specific binding ability⁴⁶ of these types of complexes to alumina column decreased the yield.



3.5.2 Infrared Spectroscopy

Infrared data of the dinuclear $[\{\text{Ru}(\text{bpy})_2(\text{dms})\}_2(\mu\text{-adpc})][\text{PF}_6]_2$ (**12**) complex in both S- and O-bonded forms have been placed in the Table 8 and a representative IR-spectrum of the initial S-bonded isomer is shown in Figure 48. The IR spectrum of S-bonded complex was taken on KBr pellet. The spectrum of O-bonded isomer obtained by evaporating the partially photolyzed acetone solution of initially S-bonded isomer with white light from Xe-150 watt arc lamp for 1 hour onto KBr pellet. The representative spectrum is shown in Figure 49.

Both IR spectra exhibited strong $\nu(\text{NCN})$ band at 2166 cm^{-1} for the coordinated adpc^{2-} ligands. The intense band located at 840 cm^{-1} is due to $\nu(\text{P-F})$ stretching of hexafluorophosphate anion in both isomers. One of the characteristics of the ruthenium-polypyridyl-sulfoxide complexes is a fairly intense $\nu(\text{SO})$ band at $1080\text{-}1150\text{ cm}^{-1}$ and $860\text{-}1000\text{ cm}^{-1}$ for S- and O-bonded sulfoxide ligands, respectively.⁵² The other characteristics of Ru-dms complexes is the weak $\nu(\text{Ru-S})$ and $\nu(\text{Ru-O})$ stretches at $410\text{-}430\text{ cm}^{-1}$ and $460\text{-}490\text{ cm}^{-1}$ respectively.⁵²⁻⁵⁵ In agreement with the reported ranges, the $\nu(\text{SO})$ of Ru-S and Ru-O isomers of the dinuclear $[\{\text{Ru}(\text{bpy})_2(\text{dms})\}_2(\mu\text{-adpc})][\text{PF}_6]_2$ complex stretches at 1098 and 1020, respectively.

Table 8 Infrared Spectroscopy Data (KBr disc)

$\nu(\text{NCN})/\text{cm}^{-1}$	$\nu(\text{SO})$ S-bound	$\nu(\text{SO})$ O-bound	$\nu(\text{Ru-S})$	$\nu(\text{Ru-O})$
2166	1098	1020	427	446

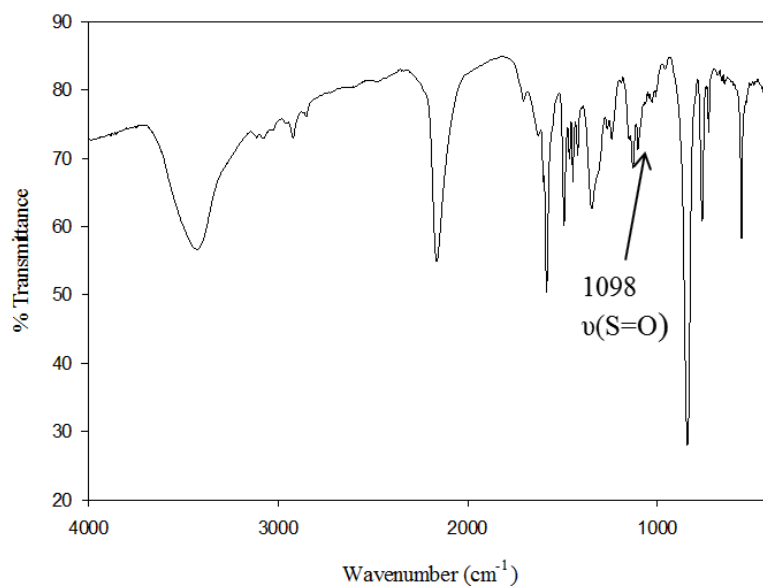


Figure 48 IR spectrum of $[\{\text{Ru}(\text{bpy})_2(\text{S-dms})\}_2(\mu\text{-adpc})][\text{PF}_6]_2$ complex(KBr disc).

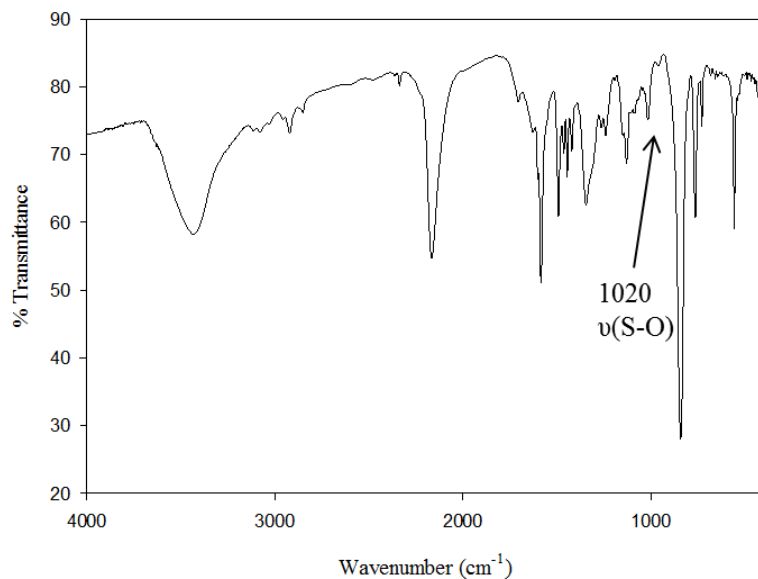


Figure 49 IR spectrum of $[\{\text{Ru}(\text{bpy})_2(\text{O-dms})\}_2(\mu\text{-adpc})][\text{PF}_6]_2$ complex(KBr disc).

3.5.3 $^1\text{H-NMR}$ Spectroscopy

The $^1\text{H-NMR}$ spectrum of the $[\{\text{Ru}(\text{bpy})_2(\text{S-dms})\}_2(\mu\text{-adpc})][\text{PF}_6]_2$ (**12**) complex was recorded in DMSO-d_6 solution and is shown in Figure 51. The chemical shifts of the protons along with the assignments of the peaks are tabulated in Table 9.

All proton peaks for bpy, adpc²⁻ and coordinated DMSO ligands were assigned with the help of coupling constants, ¹H-¹H COSY and integration values for respective peaks. The results were also compared with reported chemical shifts of structurally similar [Ru(bpy)₂(S-dmsO)(R-pcyd)][PF₆]₂ complexes.⁴⁶ The numbering scheme used to assign the protons is shown in Figure 50.

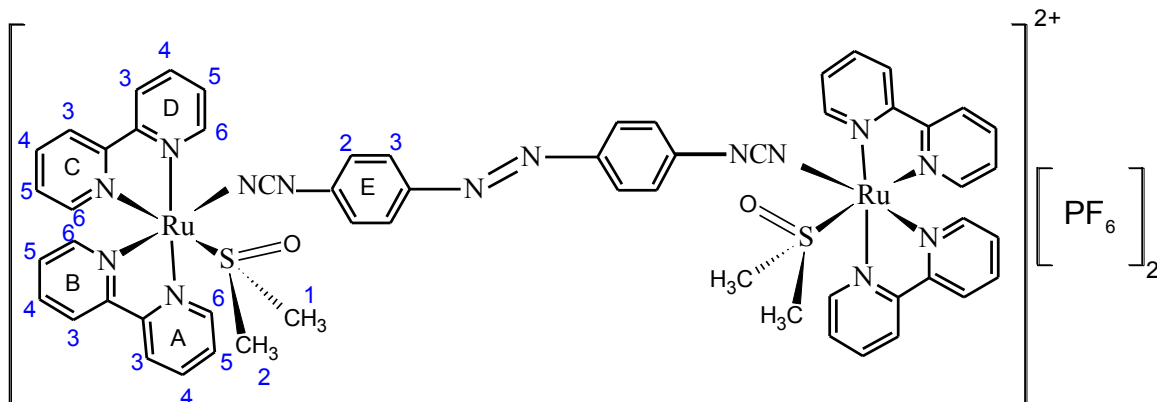


Figure 50 The numbering scheme used to assign the proton chemical shifts.

Table 9 300 MHz ¹H NMR Data of [{Ru(bpy)₂(S-dmsO)}₂(μ-adpc)][PF₆]₂ in DMSO-*d*₆.

Chemical shift (ppm) / type		
bpy	adpc	dmsO
10.04(d, 2H) A6	7.35(d, 4H) E3	3.22(s, 6H) Me1
9.18(d, 2H) D6	6.20(d, 4H) E2	2.26(s, 6H) Me2
8.85(m, 8H) D3, A3, B3		
8.74(d, 2H) C3		
8.45(t, 2H) D4		
8.36(t, 2H) A4		
8.18(t, 2H) B4		
8.10(t, 2H) C4		
8.49(q, 4H) D5, A5		
7.92(d, 2H) C6		
7.52(t, 2H) B5		
7.45(t, 2H) C5		
7.26(d, 2H) B6		

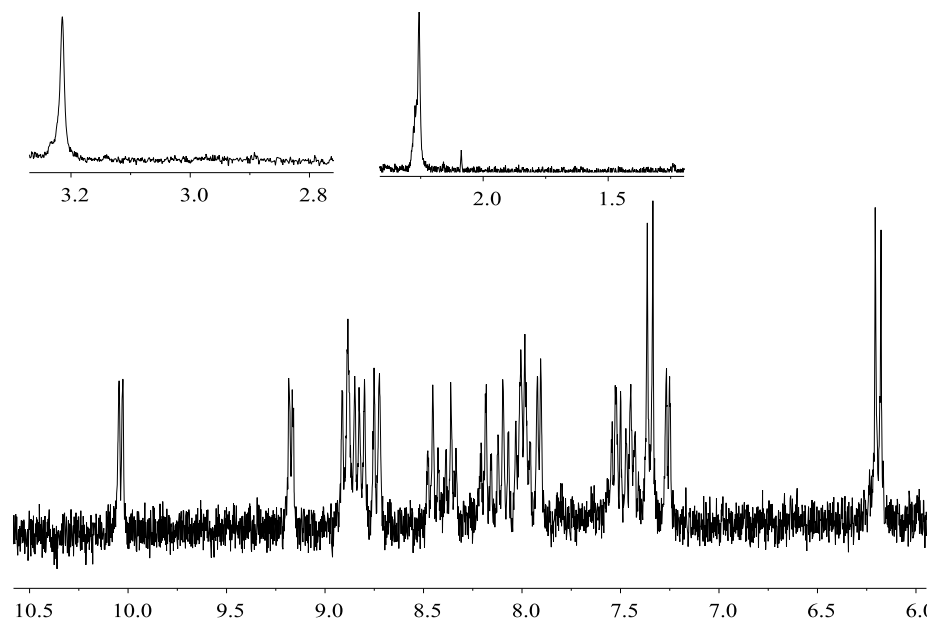


Figure 51 $^1\text{H-NMR}$ of $[\{\text{Ru}(\text{bpy})_2(\text{S-dms})\}_2(\mu\text{-adpc})][\text{PF}_6]_2$ (**12**) in DMSO-d_6 , two inset figures are the peaks for methyl groups of dms ligand.

The spectral pattern seen in $[\{\text{Ru}(\text{bpy})_2(\text{S-dms})\}_2(\mu\text{-adpc})][\text{PF}_6]_2$ (**12**) is much the same as the same protons in *cis*- $[\text{Ru}(\text{bpy})_2(\text{S-dms})\text{Cl}][\text{PF}_6]$ complex in term of the number of the peaks and chemical shifts and were assigned accordingly.^{43,56–60} The dinuclear complex (**12**) has two non-equivalent bipyridine ligands with four magnetically non-equivalent pyridine rings (rings A, B, C and D in Figure 50) therefore exhibit a total of 16 peaks in $^1\text{H-NMR}$. These 16 peaks are divided into eight doublets (positions 3 and 6 Figure 50) and eight triplets (positions 4 and 5 Figure 50) in the range of 7.26 to 10.04 ppm. Two doublets at 6.20 and 7.35 ppm with the integration of 4 are assigned to the phenyl protons of the bridging ligand, adpc²⁻. In the aliphatic region of the spectrum two singlet peaks (the inset peaks in Figure 51) with equal integrations of 6 protons, one at 3.22 and the other one at 2.26 ppm, represent two non-equivalent methyl groups on the coordinated dms ligand. The same as *cis*- $[\text{Ru}(\text{bpy})_2(\text{dms}-S)\text{Cl}][\text{PF}_6]$ complex two

methyl groups on dmsoligands in the dinuclear complex (**12**) showed non-equivalent behavior as one appeared more downfield (2.26 ppm) and the other one more up-field (3.22 ppm). According to the X-ray crystal structure of the *cis*-[Ru(bpy)₂(S-dmsoligand)Cl][PF₆] complex, one of the methyl groups (Me₂ in Figure 50) experiences the shielding (2.26 ppm) effect of the anisotropic pyridine ring current as the other one experiences the cyanamide moieties of the bridging ligand and appears at more up-field region (3.22 ppm).

¹H-NMR spectrum of the partially photolyzed solution of [$\{Ru(bpy)_2(dmsoligand)\}_2(\mu\text{-adpc})\}][PF_6]_2$ (**12**) complex in DMSO-d₆ was taken after irradiation of the solution of initially S-bonded complex (**12**) with white light from Xe-150 watt arc lamp for 1 hour. The spectra of initial S-bonded and final mixture of S- and O-bonded complex (**12**) are shown in Figure 52 to Figure 54.

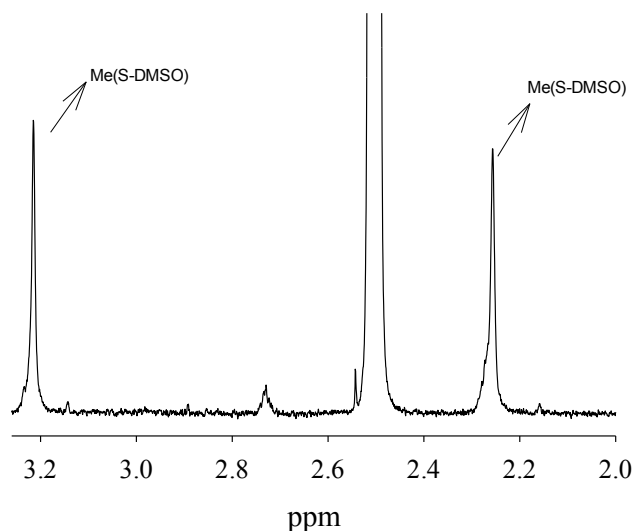


Figure 52 ¹H NMR spectra of [$\{Ru(bpy)_2(S\text{-dmsoligand})\}_2(\mu\text{-adpc})\}][PF_6]_2$ complex in dmsoligand-d₆, initial S-isomer.

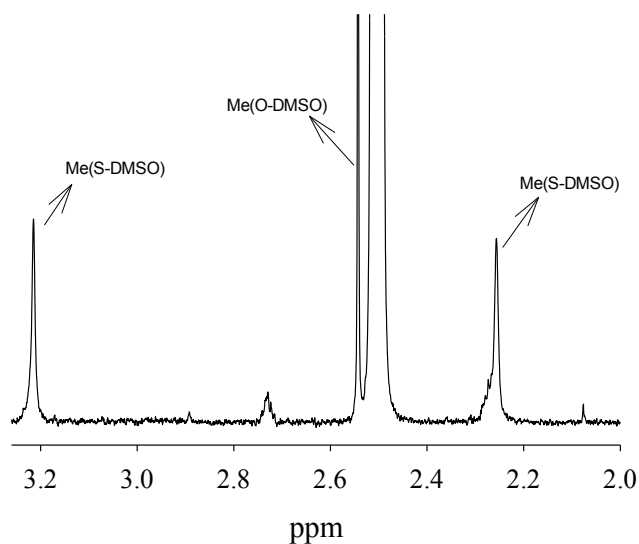


Figure 53 ^1H NMR spectra of $[\{\text{Ru}(\text{bpy})_2(\text{dmsO})\}_2(\mu\text{-adpc})][\text{PF}_6]_2$ complex in $\text{dmsO-}d_6$, after 1 hour irradiation.

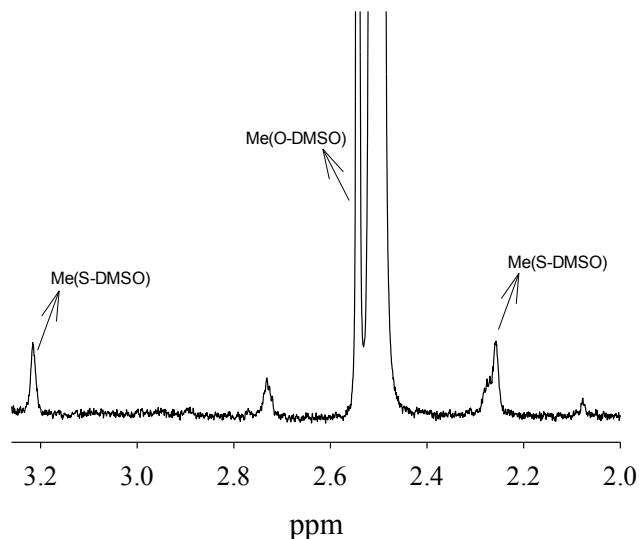


Figure 54 ^1H NMR spectra of $[\{\text{Ru}(\text{bpy})_2(\text{dmsO})\}_2(\mu\text{-adpc})][\text{PF}_6]_2$ complex in $\text{dmsO-}d_6$, after 2 hours irradiation.

Upon partial photolysis of the initial S-bonded complex (**12**) two singlet peaks of the methyl groups merged together to a sharp singlet at 2.54 ppm, close to the residual solvent peak in $\text{DMSO-}d_6$. This change in the H-NMR spectrum of dmsO complex (**12**) in the aliphatic range has been described as $\text{S} \rightarrow \text{O}$ linkage isomerism of dmsO ligand

where the chemical shifts of the two non-equivalent methyl groups in S-bond isomer merge together as two equivalent methyl groups in O-bond isomer.

3.5.4 Electronic Absorption Spectroscopy

The quantitative electronic absorption spectrum of the dinuclear complex (**12**) was recorded in its DMSO solution and as shown in Figure 55 has two maximum of absorption at 287 and 488 nm with extinction coefficients of 81500 and 55100 M⁻¹cm⁻¹ respectively.

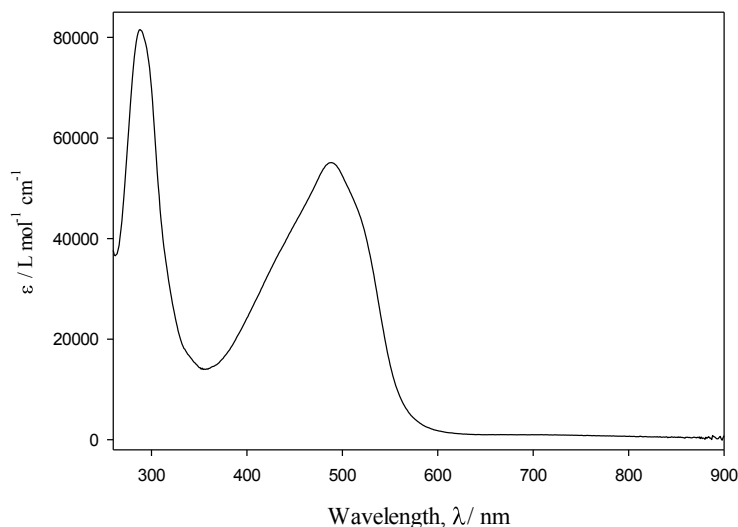


Figure 55 Electronic absorption spectrum of [{Ru(bpy)₂(S-dmsO)}₂(μ-adpc)][PF₆]₂ in DMF.

The electronic absorption spectrum of the dinuclear [{Ru(bpy)₂(S-dmsO)}₂(μ-adpc)][PF₆]₂ (**12**) complex, the same as its mononuclear analogue [Ru(bpy)₂(R-pcyd)(dmsO-S)]⁺ complexes,⁴⁶ is characterized by two intense bands, one at UV region (287 nm, ε = 81500 M⁻¹cm⁻¹) and the other band at 488 nm (ε =55100). The sharp band at UV region has been assigned to bpy rings π to π* transitions. The intense band at 488,

the same as observed for $[\{\text{Ru}(\text{trpy})(\text{bpy})\}_2(\mu\text{-adpc})]^{2+}$ (**9**) complex,¹⁴ is assigned to cyanamide-to-azo group intraligand charge transfer (ILCT) transition which has the same energy as the MLCT transition of the Ru(II)-to-bpy chromophores.

Figure 56 shows the spectra of the S- and the O-bonded isomers of $[\{\text{Ru}(\text{bpy})(\text{O-dmsso})\}_2(\mu\text{-adpc})]^{2+}$ complex in DMSO solution. The O-bonded spectrum was recorded after complete photolysis of initially S-bonded isomer using blue light (450 ± 20 nm) irradiation. As shown in Figure 57, this linkage isomerism thermally reverts back to S-bonded isomer ($\text{O} \rightarrow \text{S}$ isomerism).

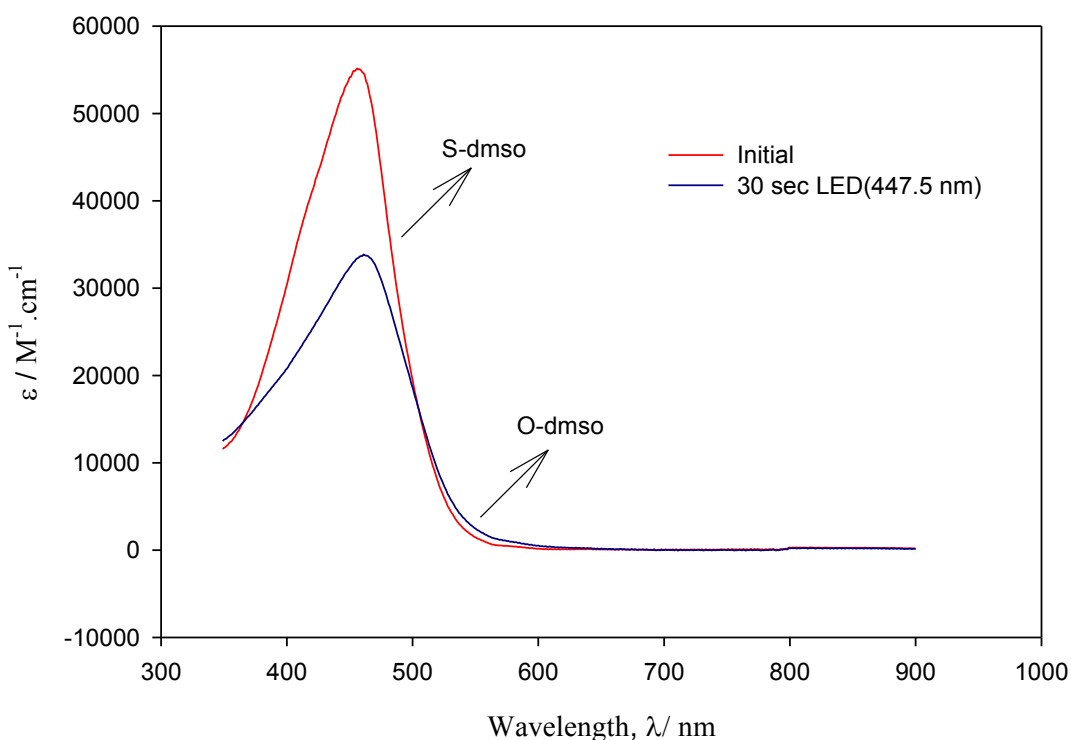


Figure 56 Photo-induced S \rightarrow O isomerization of $[\{\text{Ru}(\text{bpy})_2(\text{dmsso})\}_2(\mu\text{-adpc})]^{2+}$ in DMSO solution.

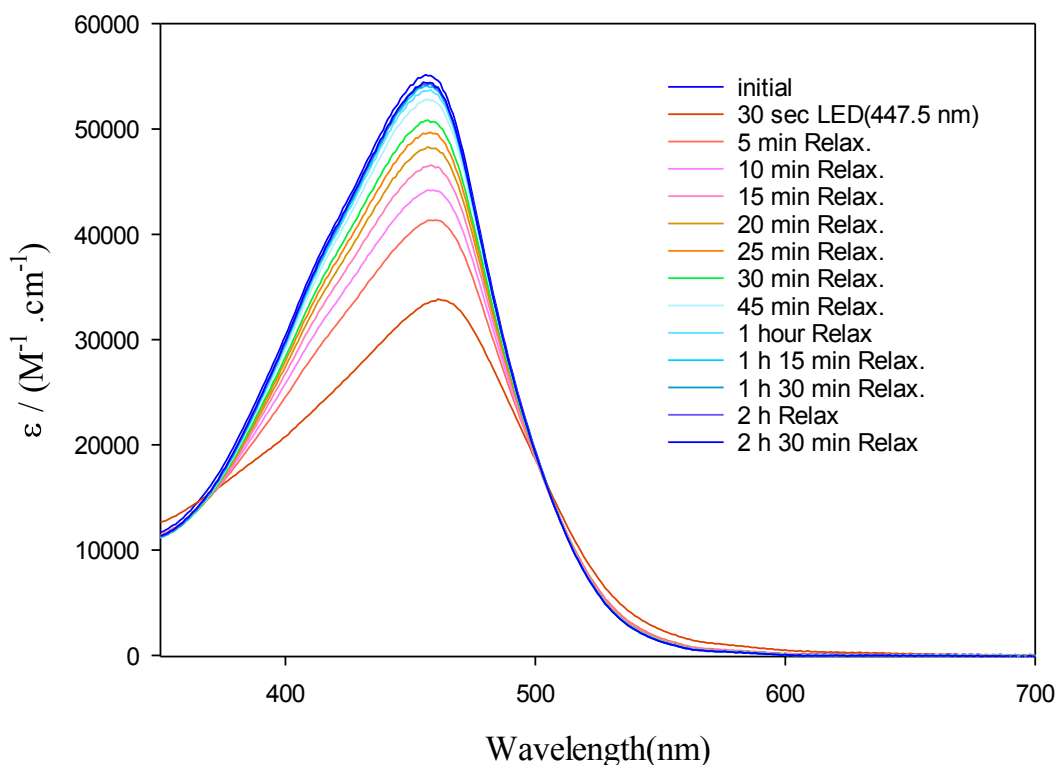


Figure 57 Thermal relaxation of photo-induced S \rightarrow O isomer of $[\{\text{Ru}(\text{bpy})_2(\text{dmsO})\}_2(\mu\text{-adpc})]^{2+}$.

3.5.5 Electrochemistry

CV of $[\{\text{Ru}(\text{bpy})_2(\text{dmsO})\}_2(\mu\text{-adpc})][\text{PF}_6]_2$ (**12**) complex was performed in DMSO at the scan rate of 0.1 V/sec. The cyclic voltammogram is shown in Figure 58. The voltammogram of this complex (**12**) showed two quasi-reversible and one irreversible peaks. The first two reversible peaks at 0.76 V and 0.94 V potentials have been assigned to Ru(III/II) oxidation and the irreversible one at 1.09 V assigned to the oxidation of two Ru(III) centres to Ru(IV).

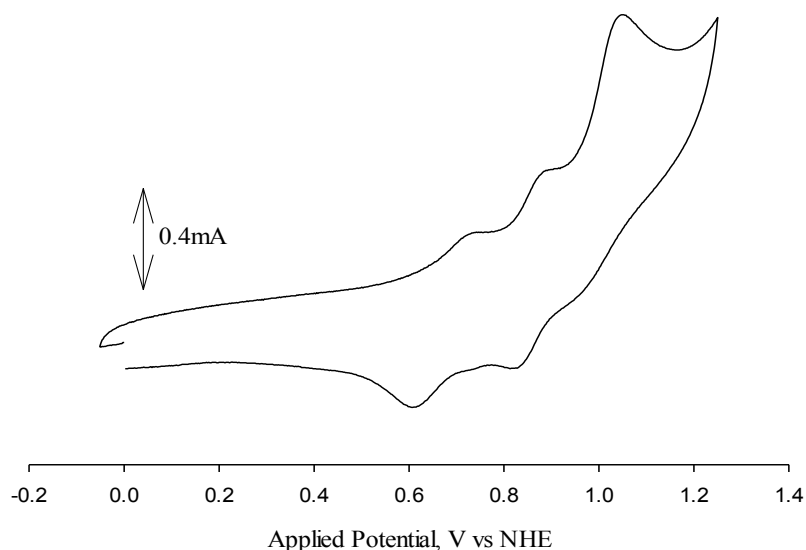


Figure 58 Cyclic voltammogram [$\{\text{Ru}(\text{bpy})_2(\text{dmsO})\}_2(\mu\text{-adpc})\}[\text{PF}_6]_2$ in DMSO with 0.1 M tetrabutylammonium hexafluorophosphate, using platinum counter and working electrode, silver wire pseudo-reference (cobaltocene internal reference, $E^\circ = -0.589$ V versus NHE) at scan rate of 100mV/s.

The separations between cathodic and anodic quasi-reversible waves for Ru(III/II) oxidations are 96 mV and 92 mV at different scan rates. As $K_C = 10^{16.91 \Delta E}$ and with $\Delta E = 180$ mV the comproportionation equilibrium constant for of $[\{\text{Ru}(\text{bpy})(\text{dmsO})\}_2(\mu\text{-adpc})]^{3+}$ complex was calculated to be $K_c = 1.11 \times 10^3$. This K_c value implies this complex as Class II with a moderate coupling between metal centres.

3.5.6 DFT Calculation

Figure 59 shows theoretical DFT calculation of frontier molecular orbitals of $[\{\text{Ru}(\text{bpy})(\text{dmsO})\}_2(\mu\text{-adpc})]^{2+}$ (**12**) complex using the B3LYP/6-31G* model. The same as $[\{\text{Ru}(\text{bpy})_2\}_2(\mu\text{-adpc})_2]$ (**11**) complex the HOMO and also HOMO-1 are mostly on phenylcyanamide bridging ligand and LUMO has the bipyridine character.

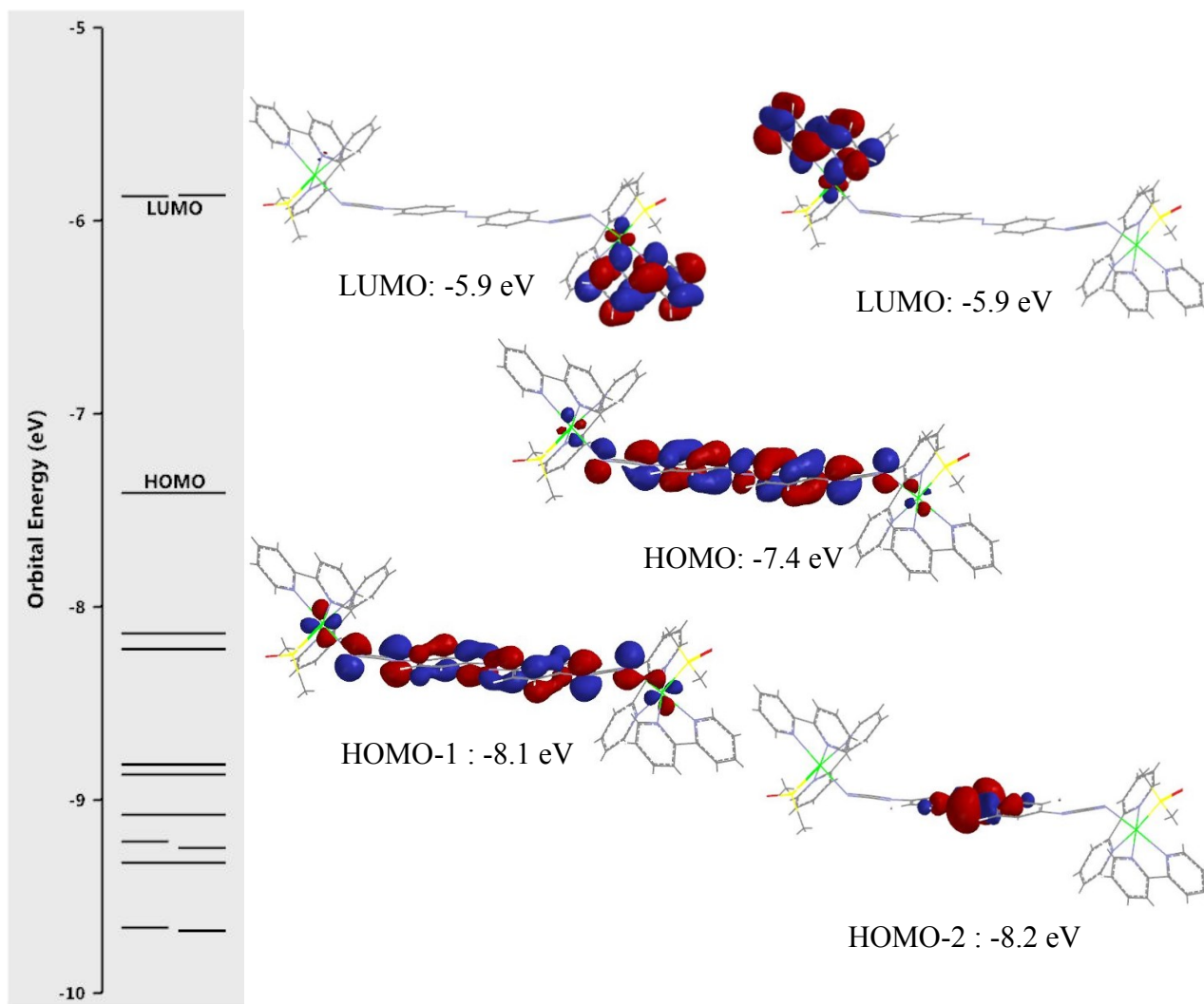


Figure 59 DFT calculation of orbital energies and selected molecular orbitals of $[\{\text{Ru}(\text{bpy})_2(\text{dmsO})\}_2(\mu\text{-adpc})][\text{PF}_6]_2$ (**12**).

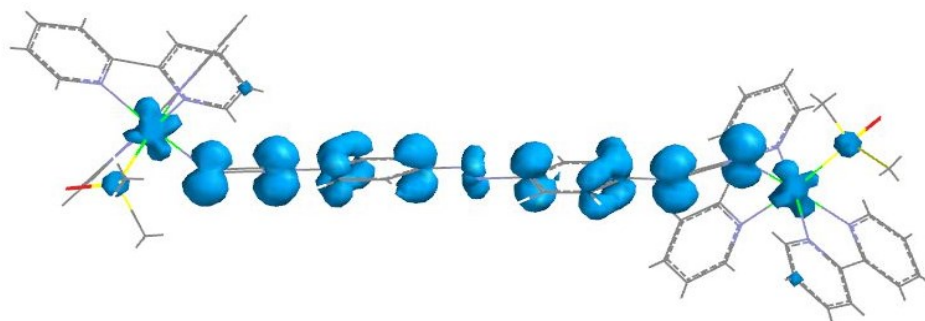


Figure 60 Spin density distribution of $[\{\text{Ru}(\text{bpy})_2(\text{dmsO})\}_2(\mu\text{-adpc})]^{3+}$ (**12**).

The DFT calculation of the spin density distribution in the mixed-valence complex $[\{\text{Ru}(\text{bpy})_2(\text{dmsO})\}_2(\mu\text{-adpc})]^{3+}$ is shown in Figure 60. According to these calculation spin density resides mostly in $p\pi$ atomic orbitals of the bridging ligand with slight $d\pi$ orbital contributions from the ruthenium ions. Based on this calculation alone, a radical bridging ligand state is predicted however as has been stated before solvent interactions can shift spin density onto the metal²⁹ and because of this interpretation of Figure 60 should be qualified.

3.6 Conclusion

$[\{\text{Ru}(\text{bpy})\}_2(\mu\text{-adpc})_2]$ (**11**) and $[\{\text{Ru}(\text{bpy})_2(\text{dmsO})\}_2(\mu\text{-adpc})][\text{PF}_6]_2$ (**12**) were prepared and characterized by elemental analysis and ¹H-NMR spectroscopy. Cyclic voltammetry studies of the neutral complex showed two reversible peaks each consists with one electron for Ru(III/II) couples and a peak in consistence with two electron reaction for L^0/L^{-1} of bridging ligands. IR- and UV-Vis-spectroelectrochemistry of the dinuclear $[\{\text{Ru}(\text{bpy})\}_2(\mu\text{-adpc})_2]$ (**11**) complex showed that the oxidation yields a Class II mixed-valence state with $K_c = 1.11 \times 10^3$. Electronic absorption studies on $[\{\text{Ru}(\text{bpy})_2(\text{dmsO})\}_2(\mu\text{-adpc})][\text{PF}_6]_2$ (**12**) complex showed the complex undergoes photo-induced linkage isomerism in solution using 447.5 nm LED lamp. The $[\{\text{Ru}(\text{bpy})_2(\text{dmsO})\}_2(\mu\text{-adpc})]^{2+}$ isomer reverts back thermally to $[\{\text{Ru}(\text{bpy})_2(\text{dmsO-S})\}_2(\mu\text{-adpc})]^{2+}$. The cyclic voltammogram of this complex showed three processes as two quasi-reversible couples for Ru(III/II) followed by one irreversible process which we assigned to Ru(III/IV).

Gas phase DFT calculations on both the mixed-valence dinuclear complexes **(11)** and **(12)** showed spin-density distribution to be localized mostly on the bridging ligand with only a small contribution from the ruthenium centres in disagreement with IR spectroelectrochemical studies.

Chapter 4: Conclusion and Future Work

4.1 Research Summary

The synthesis and characterization of the brand new phenylcyanamide ligand tdpc^{2-} : 3,6-bis(phenylcyanamido)-1,2,4,5-tetrazine and its dinuclear ruthenium complex $[\{\text{Ru}(\text{tpty})(\text{bpy})\}_2(\mu\text{-tdpc})][\text{PF}_6]_2$ were described in Chapter 2.

The elemental analysis and the $^1\text{H-NMR}$ of the protonated H_2tdpc (**4**) were in a good agreement with the expected formula. The IR-spectrum showed the sharp $\nu(\text{NCN})$ band at 2228 cm^{-1} and 2124 cm^{-1} for neutral and dianion form of the ligand, respectively. Low solubility of the thallium salt of tdpc^{2-} ligand (**5**) prevents us from further purification and also performing cyclic voltammetry studies on the dianion form of the ligand. The electronic absorption spectra of H_2tdpc (**4**) showed absorption at UV region (275 nm) which upon partial deprotonation (dissolving in DMF, strong donor solvents) and complete deprotonation, as in $\text{Tl}_{1.75}\text{tdpc}$ (**5**), shifts to longer wavelengths, 450 nm.

Elemental analysis, $^1\text{H-NMR}$ and IR-spectroscopies of the dinuclear complex (**6**) confirmed the proposed formula. Cyclic voltammetry and spectroelectrochemistry were used to study the coupling between two metal centres in the dinuclear complex (**6**). Table 4 showed the cyclic voltammetry results for $[\{\text{Ru}(\text{tpty})(\text{bpy})\}_2(\mu\text{-tdpc})][\text{PF}_6]_2$ (**6**) complex in comparison to Class(III) $[\{\text{Ru}(\text{trpy})(\text{bpy})\}_2(\mu\text{-adpc})][\text{PF}_6]_2$ (**9**) complex. The shape and the ΔE_p (separation between the cathodic and anodic potentials) of the only observed oxidation wave for $[\{\text{Ru}(\text{tpty})(\text{bpy})\}_2(\mu\text{-tdpc})]^{2+}$ (**6**) is consistence with two overlapped Ru(II/III) couples.

UV-Vis spectroelectrochemistry of the complex (**6**) showed formation of the new band at 1190 nm with a low energy tail centered at 1530 nm during the oxidation of the complex (**6**) which is assigned to an intervalence transition. The band at 1190 is assigned to two overlapped metal-to-ligand charge transfer (MLCT) bands. Calculations based on the properties of the intervalence band confirmed weak metal-metal coupling in $[\{\text{Ru}(\text{ttpy})(\text{bpy})\}_2(\mu\text{-tdpc})]^{3+}$ complex. The IR-spectroelectrochemistry of this complex during the oxidation showed rapid decrease of the initial $\nu(\text{NCN})$ band and appearance of a new weak band at lower frequencies. The appearance of two $\nu(\text{NCN})$ in the IR spectra of the mixed-valence complex (**6**) supports the valence-trapped state. The overall results from CV, Vis-NIR and IR spectroelectrochemistry showed the mixed-valence $[\{\text{Ru}(\text{ttpy})(\text{bpy})\}_2(\mu\text{-tdpc})]^{3+}$ complex to have metal-metal coupling of 400 cm^{-1} which is consistent with a weakly-coupled Class II system.

Spin density calculation on the mixed-valence $[\{\text{Ru}(\text{ttpy})(\text{bpy})\}_2(\mu\text{-tdpc})]^{3+}$ complex (**6**) showed majority of the spin density on the $p\pi$ orbitals of the bridging ligand with minor contribution of metal $d\pi$ orbitals which is not in agreement with the experimental results. As explained before, solvent interactions with the complex can shift spin density to the metal centres.

The DFT studies on the dianion form of tdpc^{2-} (**5**) ligand showed stability of HOMO by the factor of 0.7 eV in compare to adpc^{2-} . The extra stability of the HOMO was expected to decrease the metal-metal coupling in dinuclear systems when tdpc^{2-} bridges the metal centres in compare to adpc^{2-} systems if the hole transfer superexchange mechanism was dominant. The experimentally observed weak coupling in $[\{\text{Ru}(\text{ttpy})(\text{bpy})\}_2(\mu\text{-tdpc})]^{3+}$ (**6**) compare to strong coupling in $[\{\text{Ru}(\text{trpy})(\text{bpy})\}_2(\mu\text{-$

adpc)] (**9**) complex suggests hole-transfer superexchange as the major pathway for our phenylcyanamide systems.

In the second study of this research dinuclear [$\{\text{Ru}(\text{bpy})_2\}_2(\mu\text{-adpc})_2$] (**11**) complex was synthesized and the proposed formula was approved by elemental analysis. IR-spectrum of the complex with a sharp band at 2161 cm^{-1} confirmed the presence of cyanamide ligand. $^1\text{H-NMR}$ spectrum of the complex (**11**) consists of 10 peaks was also in agreement with the expected structure.

The cyclic voltammogram of the dinuclear complex (**11**) consists of 3 oxidation couples which are assigned to two separate one-electron processes for Ru(II/III) and one two-electron process for L(-1/-2) oxidations.

UV-Vis spectroelectrochemistry study of the complex (**11**) showed formation of a metal-to-metal charge transfer (MMCT) band centered at 2000 nm. Further oxidation to generate $[\text{Ru}(\text{III}),\text{Ru}(\text{III})]$ species caused an ILCT band at 1400 nm.

The IR-spectroelectrochemistry study on [$\{\text{Ru}(\text{bpy})_2\}_2(\mu\text{-adpc})_2$] (**11**) complex showed Class II behavior during the oxidation. The oxidation resulted in the intensity decrease of the initial $\nu(\text{NCN})$ and generation of a new peak at lower frequencies.

The total results of different experimental tests showed moderate metal-metal coupling in the mixed-valence $[\text{Ru}(\text{II}), \text{Ru}(\text{III})]$ state of the complex (**11**). With a calculated $K_c = 1.11 \times 10^3$, this mixed-valence complex is classified as a Class II complex.

Gas phase DFT calculation on the spin density distribution of the mixed-valence $[\{\text{Ru}(\text{bpy})_2\}_2(\mu\text{-adpc})_2]^+$ complex (**11**) showed greater contribution of ruthenium- $d\pi$ orbital with the bridging ligand's orbitals than in $[\{\text{Ru}(\text{tpp})_2(\text{bpy})\}_2(\mu\text{-tdpc})]^{3+}$ (**6**). It is

suggested that inclusion of the effect of solvent-solute interaction in the DFT calculation would result in better agreement with the spectroelectrochemical studies of the complex.

The characterized dinuclear [$\{\text{Ru}(\text{bpy})_2\}_2(\mu\text{-adpc})_2$] (**11**) complex was then used to synthesize the dinuclear [$\{\text{Ru}(\text{bpy})_2(\text{S-dmsO})\}_2(\mu\text{-adpc})$][PF_6]₂ complex (**12**) in order to investigate the linkage-isomerism of dmsO with the aim of developing a mixed-valence “photo-switchable” complex. Characterization of the S-bonded complex by elemental analysis and infrared spectroscopy confirmed the proposed formula and the presence of adpc²⁻ ligand. ¹H-NMR spectrum of the S-bonded complex (**12**) consists of 18 peaks for aromatic rings and two shielded singlet peaks for two methyl groups on dmsO ligands which are in agreement with the proposed structure and formula. The ¹H-NMR spectrum of the partially photolyzed [$\{\text{Ru}(\text{bpy})_2(\text{dmsO})\}_2(\mu\text{-adpc})$] complex (**12**) showed the same pattern as the S-bonded isomer except for the methyl peaks.

Cyclic voltammetry data for this complex (**12**) showed two reversible Ru(II/III) couples and one irreversible couple which we assigned to Ru(III/IV) oxidations of both metal centres.

Electronic absorption spectroscopic studies on the complex (**12**) in DMSO solution showed mostly the same absorptions as for the precursor [$\{\text{Ru}(\text{bpy})_2\}_2(\mu\text{-adpc})_2$] (**11**) complex. The spectrum consists of two absorption peaks one at UV region which is assigned to π to π^* transitions of bipyridine and phenyl rings and a peak in visible region which has been assigned to cyanamide-to-azo intraligand charge transfer (ILCT).

Irradiation of the DMSO solution of the complex (**12**) showed decrease of the electronic absorption which we assigned to S \rightarrow O linkage isomerism of dmsO that

thermally reverts back to sulfur bound over 3 hours. Thermal reversibility of the electronic absorption change shows photo-switchable activity of this complex.

Gas phase DFT calculation on the spin density of this complex (**12**), the same as the other two complexes, showed the most of the density on the bridging ligand.

4.2 Future Work

Changing the acceptor group, azo, in adpc^{2-} (**7**) with stronger acceptor unit such as tetrazine in tdpc^{2-} (**4**) stabilized the π -HOMO of the bridging ligand by 0.7 eV, which against our prediction showed decrease of coupling between the two metal centres in its dinuclear $[\{\text{Ru}(\text{ttpy})(\text{bpy})\}_2(\mu\text{-tdpc})]^{2+}$ (**6**) complex. Further characterization of the complex by EPR would provide more quantitative estimate of spin density distribution on the complex (**6**). Also changing the energy of the HOMO of tdpc^{2-} through synthesis of substituted tdpc^{2-} ligands with different electron donor groups can provide more information about the effect of this group of ligands on the degree of metal-metal coupling.

$^1\text{H-NMR}$ and electronic absorption spectroscopic studies on photo-linkage isomerism of the dinuclear $[\{\text{Ru}(\text{bpy})_2(\text{dmsO})\}_2(\mu\text{-adpc})]^{2+}$ (**12**) complex showed encouraging results. UV-Vis- and IR- spectroelectrochemistry studies on $[\{\text{Ru}(\text{bpy})_2(\text{dmsO})\}_2(\mu\text{-adpc})][\text{PF}_6]_2$ (**12**) would be the next step in characterizing this potentially photo-switchable complex completely in solution. Previous studies on mononuclear complexes of the same coordination showed solid state photo-isomerization of ruthenium-dmsO complexes in Poly(methyl methacrylate) (PMMA) polymer films.⁴⁶

The same studies on the dinuclear complex (**12**) may open new aspects in molecular devices.

Synthesis of analogue complexes with substituted adpc^{2-} ligands with different electronic absorption than adpc^{2-} would also be a further step in synthesis of photo-switchable complexes.

Appendices

Appendix A : Techniques

A.1 Preparation of Ag/ AgCl Reference Electrode

As reference electrode in OTTLE cell two stripes of silver wires with known diameter were twisted together and were soaked in 3M HNO₃ solution for 5 minutes and then rinsed with deionized water. The cleaned silver wire was then used as working electrode in the standard H-cell with platinum disk counter and the reference glassy Ag/AgCl electrode. 0.1m HCl solution was used as electrolyte. The current density then was set as 0.4 mA/cm² of the silver wire. The cell was left in the adjusted current for 30 minutes while the white-gray Ag/AgCl layer was collected on the surface of the working silver wire. The Ag/AgCl electrode was then rinsed with deionized water and left to dry.

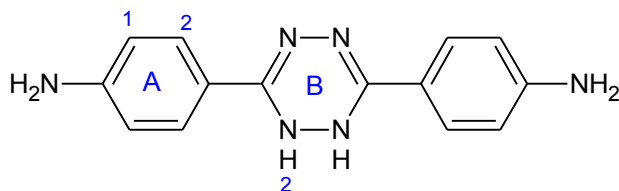
A.2 TBAH Preparation

TBAH was synthesized through the combination of 0.1 M tetrabutylammonium bromide (1 g in 30 mL 1:1 ethanol/water) solution with 0.1 M (30 mL 1:1 ethanol/water solution of 0.5 g) ammonium hexafluorophosphate. Precipitated white TBAH was collected and washed with 30 mL water.

Recrystallization of TBAH was achieved through dissolving the crude product in 30m hot ethanol followed by filtration. To the still hot filtrate was added 10mL water. The solution was cooled to room temperature and then chilled down overnight in the fridge. The white TBAH needles were collected and the same process was done for 2 more times. The pure TBAH was vacuum dried at 110°C (refluxing toluene) for 48hours. Yield: 77%.

Appendix B : NMR Spectra

B.1 3,6-bis-(4-aminophenyl)-1,2-dihydro-1,2,4,5-tetrazine (1)



300 MHz ^1H NMR Data of (1) in $\text{DMSO-}d_6$.

Chemical shift (ppm) / type		
Phenyl	Tetrazine	Ammine
6.53 (d, 4H) A1 7.47 (d, 4H) A2	8.51 (s, 2H) B2	5.48 (s, 4H)

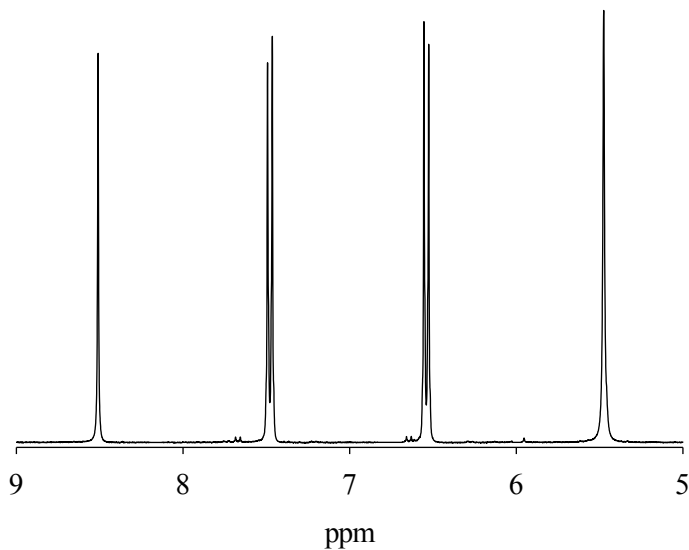
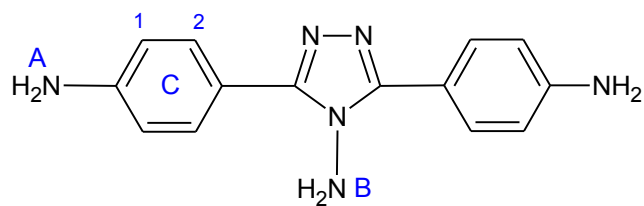


Figure 61 ^1H -NMR spectrum of 3,6-bis-(4-aminophenyl)-1,2-dihydro-1,2,4,5-tetrazine in $\text{DMSO-}d_6$.

B.2 3,5-diamino-4-amino-1,2,4-triazol



300 MHz ¹H NMR Data of 3,5-diamino-4-amino-1,2,4-triazol in DMSO-*d*₆.

Chemical shift (ppm) / type		
phenyl	triazol	ammine
6.64 (d, 4H) C1 7.67 (d, 4H) C2	5.96 (s, 2H) B	5.46 (s, 4H) A

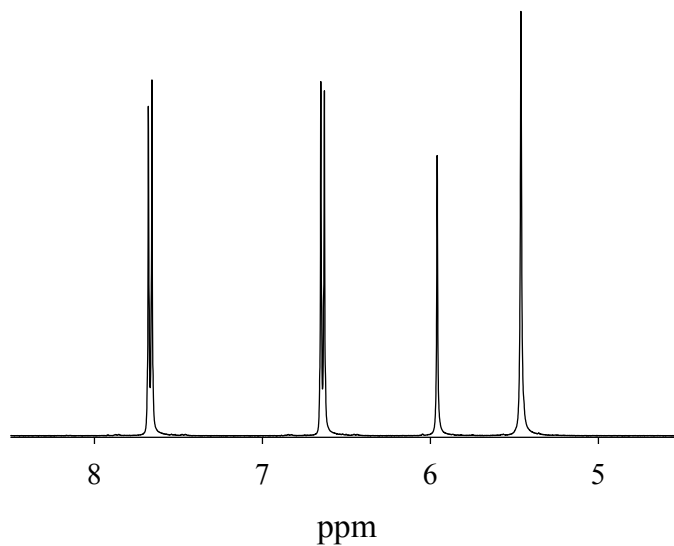
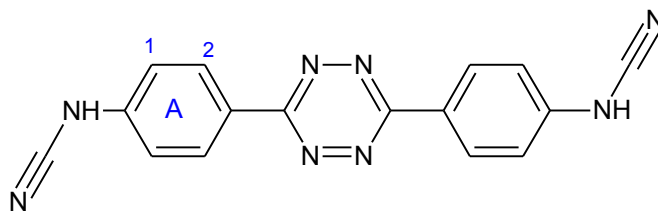


Figure 62 ¹H-NMR spectrum of 3,5-diamino-4-amino-1,2,4-triazol in DMSO-*d*₆

B.3 H₂tdpc (4)



300 MHz ¹H NMR Data of (4) in DMSO-*d*₆.

Chemical shift (ppm) / type	
phenyl	cyanamide
7.25 (d, 4H) A1	10.81 (broad s, 2H)
8.50 (d, 4H) A2	

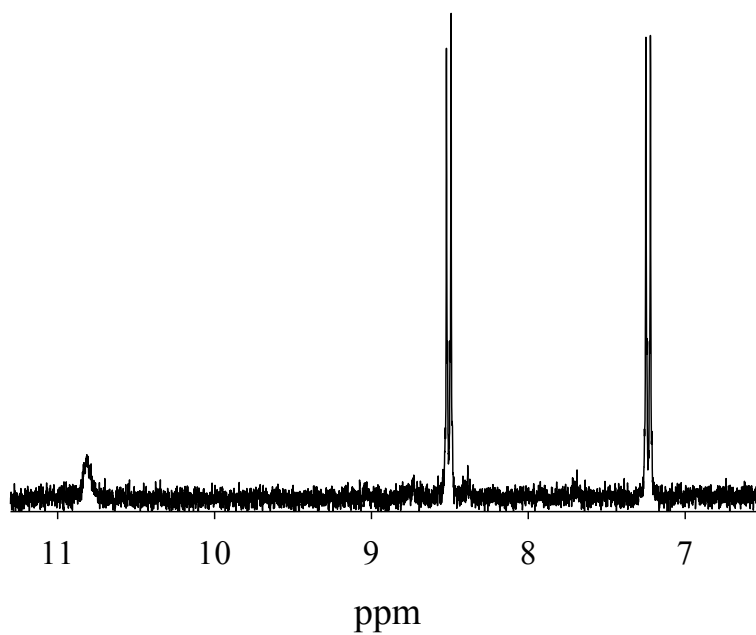
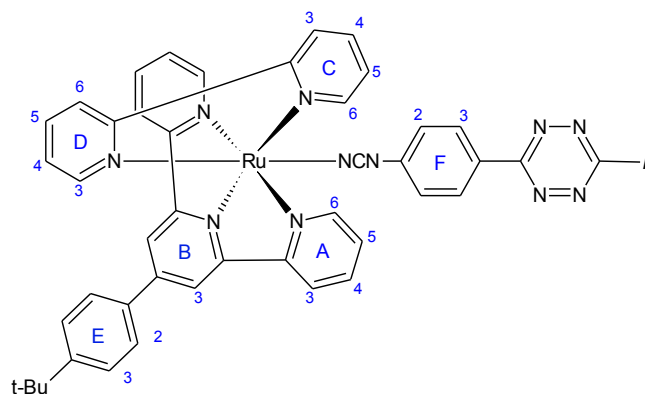


Figure 63 ¹H-NMR spectrum of H₂tdpc in DMSO-*d*₆.

B.4 $[\{\text{Ru}(\text{ttpy})(\text{bpy})\}_2(\mu\text{-tdpc})][\text{PF}_6]_2$ (**6**)



300 MHz ^1H NMR Data of (**6**) in $\text{DMSO-}d_6$.

Chemical shift (ppm) / type		
ttpy , bpy	tdpc	t-Butyl
9.68 (d, 2H) C6	8.24 (d, 4H) F3	1.38 (s, 18 H)
9.25 (s, 4H) B3	6.17 (d, 4H) F2	
9.00 (m, 6H) C3, A3		
8.72 (d, 2H) D3		
8.45 (t, 2H) C4		
8.18 (m, 6H) E2, D4		
7.94 – 7.83 (m, 6H) C5, A4		
7.77 (d, 4H) E3		
7.72 (d, 4H) A6		
7.57 (d, 2H) D6		
7.52 – 7.46 (t, 4H) A5		
7.18 (t, 2H) D5		

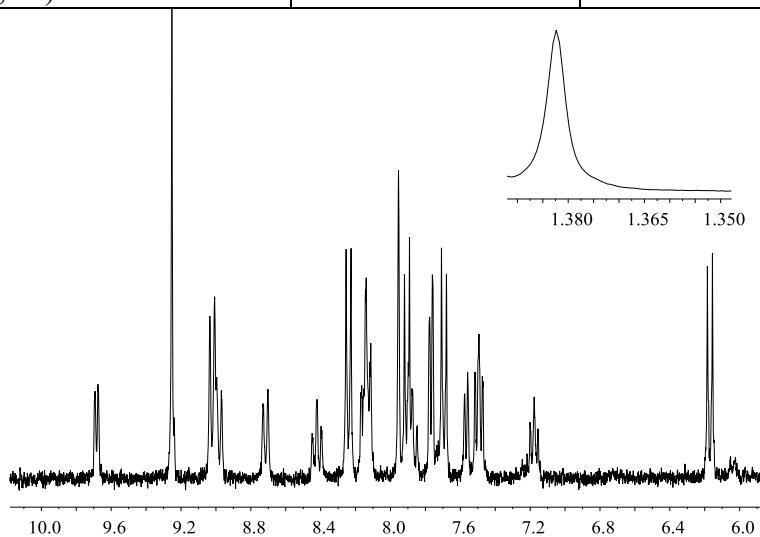
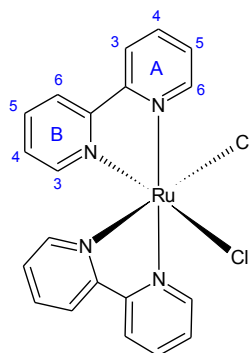


Figure 64 ^1H -NMR spectrum of $[\{\text{Ru}(\text{ttpy})(\text{bpy})\}_2(\mu\text{-tdpc})][\text{PF}_6]_2$ in $\text{DMSO-}d_6$.

B.5 $[\text{Ru}(\text{bpy})_2\text{Cl}_2]$ (**10**)



300 MHz ^1H NMR Data of (**10**) in $\text{DMSO-}d_6$.

Chemical shift (ppm) / type
bpy
9.98 (d, 2H) A6
8.65 (d, 2H) A3
8.50 (d, 2H) B3
8.07 (m, 2H) A4
7.77 (m, 2H) A5
7.68 (m, 2H) B4
7.52 (d, 2H) B6
7.10 (t, 2H) B5

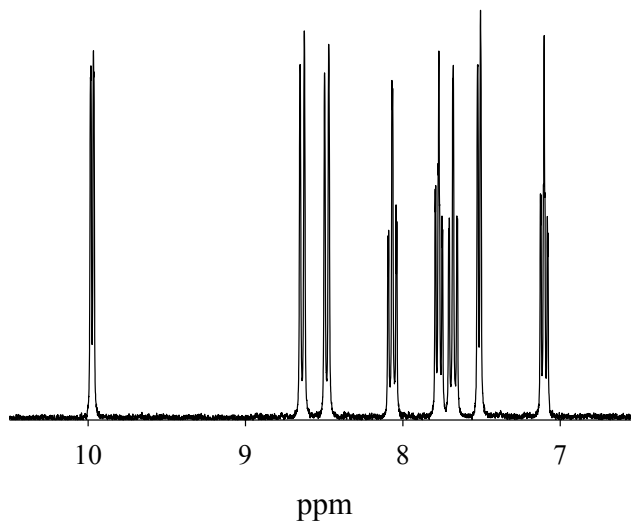
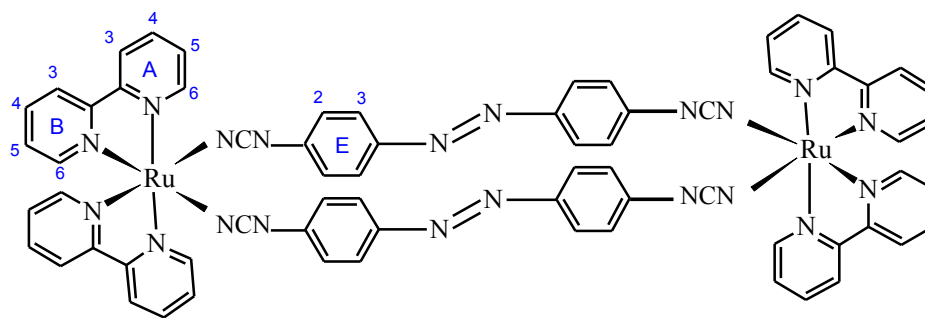


Figure 65 ^1H -NMR of $\text{cis-}[\text{Ru}(\text{bpy})_2\text{Cl}_2]$ in $\text{DMSO-}d_6$.

B.6 $[\{\text{Ru}(\text{bpy})_2\}_2(\mu\text{-adpc})_2]$ (**11**)



300 MHz ^1H NMR Data of (**11**) in $\text{DMSO-}d_6$.

Chemical shift (ppm) / type	
bpy	adpc
9.54 (d, 4H) A6	7.48 (d, 8H) F3
8.80 (d, 4H) A3	6.68 (d, 8H) F2
8.67 (d, 4H) B3	
7.95 (t, 4H) A4	
7.93 (m, 8H) A5, B4	
7.70 (d, 4H) B6	
7.29 (t, 4H) B5	

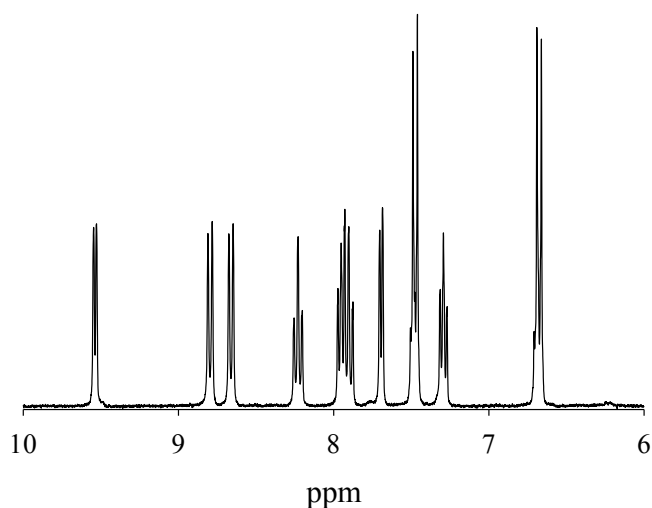


Figure 66 ^1H -NMR of $[\{\text{Ru}(\text{bpy})_2\}_2(\mu\text{-adpc})_2]$ in $\text{DMSO-}d_6$.

References:

- (1) Ariga, K.; Kunitake, T. *Supramolecular Chemistry — Fundamentals and Applications*; Springer-Verlag: Berlin/Heidelberg, 2006; pp. 7–38.
- (2) Richmond, C. J.; Parenty, A. D. C.; Song, Y.-F.; Cooke, G.; Cronin, L. *J. Am. Chem. Soc.* **2008**, *130*, 13059–13065.
- (3) Ferri, V.; Costa, E.; Biancardo, M.; Argazzi, R.; Bignozzi, C. A. *Inorganica Chim. Acta* **2007**, *360*, 1131–1137.
- (4) Bernhardt, P.; Bozoglian, F.; Macpherson, B.; Martinez, M. *Coord. Chem. Rev.* **2005**, *249*, 1902–1916.
- (5) Braun-Sand, S. B.; Wiest, O. *J. Phys. Chem. A* **2003**, *107*, 285–291.
- (6) Demadis, K. D.; Hartshorn, C. M.; Meyer, T. J. *Chem. Rev.* **2001**, *101*, 2655–2685.
- (7) Hillman, M.; Kvik, A. *Organometallics* **1983**, *2*, 1780–1785.
- (8) Ward, M. D. *Chem. Soc. Rev.* **1995**, *24*, 121.
- (9) Hage, R.; Haasnoot, J. G.; Reedijk, J.; Wang, R.; Vost, J. G. *Inorg. Chem.* **1991**, *30*, 3263–3269.
- (10) Aquino, M. A. S.; Lee, F. L.; Gabe, E. J.; Bensimon, C.; Greedan, J. E.; Crutchley, R. J. *J. Am. Chem. Soc.* **1992**, *114*, 5130–5140.
- (11) Evans, C. E. B.; Naklicki, M. L.; Rezvani, A. R.; White, C. a.; Kondratiev, V. V.; Crutchley, R. J. *J. Am. Chem. Soc.* **1998**, *120*, 13096–13103.
- (12) DeRosa, M. C.; White, C. a.; Evans, C. E. B.; Crutchley, R. J. *J. Am. Chem. Soc.* **2001**, *123*, 1396–1402.
- (13) Choudhuri, M. M. R.; Kaim, W.; Sarkar, B.; Crutchley, R. J. *Inorg. Chem.* **2013**, *52*, 11060–11066.
- (14) Mosher, P. J.; Yap, G. P.; Crutchley, R. J. *Inorg. Chem.* **2001**, *40*, 1189–1195.
- (15) Rezvani, A. R.; Crutchley, R. J. *Inorg. Chem.* **1994**, *33*, 170–174.
- (16) Naklicki, M. L.; Crutchley, R. J. *Inorganica Chim. Acta* **1994**, *225*, 123–127.
- (17) Richardson David E. *Coord. Chem. Rev.* **1984**, *60*, 107–129.

- (18) Sutton, J. E.; Sutton, P. M.; Taube, H. *Inorg. Chem.* **1979**, *18*, 1017–1021.
- (19) Barriere, F.; Camire, N.; Geiger, W. E.; Mueller-westerhoff, U. T.; Sanders, R. J. *Am. Chem. Soc.* **2002**, *124*, 7262–7263.
- (20) Hush, N. S. *Prog. Inorg. Chem.* **1967**, *8*, 391.
- (21) Creutz, C.; Newton, M. D.; Sutin, N. *J. Photochem. Photobiol. A Chem.* **1994**, *82*, 47–59.
- (22) Crutchley, R. J. *Coord. Chem. Rev.* **2001**, *221*, 125–155.
- (23) Evans, C. E. B.; Yap, G. P. a.; Crutchley, R. J. *Inorg. Chem.* **1998**, *37*, 6161–6167.
- (24) Crutchley, R. J.; Mccaw, K.; Lee, I. F. L.; Gabe, E. J. *Inorg. Chem.* **1990**, *29*, 2576–2581.
- (25) Crutchley, R. J. *Inorg. Chem.* **1993**, *32*, 5808–5812.
- (26) Harb, C.; Kravtsov, P.; Choudhuri, M.; Sirianni, E. R.; Yap, G. P. a; Lever, a B. P.; Crutchley, R. J. *Inorg. Chem.* **2013**, *52*, 1621–1630.
- (27) Mosher, P. J.; Yap, G. P.; Crutchley, R. J. *Inorg. Chem.* **2001**, *40*, 550–553.
- (28) Crutchley, R. J.; Naklicki, M. L. *Inorg. Chem.* **1989**, *28*, 1955–1958.
- (29) Naklicki, M. L.; Gorelsky, S. I.; Kaim, W.; Sarkar, B.; Crutchley, R. J. *Inorg. Chem.* **2012**, *51*, 1400–1407.
- (30) Habibagahi, F.; Crutchley, R. J. *Can. J. Chem.* **2014**, *92*, 1081–1085.
- (31) Fred F. Shetterly; C. f. Hale. *J. Am. Chem. Soc.* **1911**, *33*, 1071–1076.
- (32) Sołoducho, J.; Doskocz, J.; Cabaj, J.; Roszak, S. *Tetrahedron* **2003**, *59*, 4761–4766.
- (33) Bentiss, F.; Lagrenee, M.; Traisnel, M.; Mernari, B.; Elattari, H. *J. Heterocycl. Chem.* **1999**, *36*, 149–152.
- (34) Gennett, T.; Milner, D. F.; Weaver, M. J. *J. Phys. Chem.* **1985**, *89*, 2787–2794.
- (35) Krejeik, M.; Danek, M.; Hartl, F. *J. Electroanal. Chem.* **1991**, *317*, 179–187.
- (36) Zhang, C.-R.; Wang, Y.-L. *Synth. Commun.* **2003**, *33*, 4205–4208.

- (37) Steffen, G.; Reinen, D.; Stratemeier, H.; Riley, M. J.; Hitchman, M. A.; Matthies, H. E.; Recker, K.; Wallrafen, J. F.; Niklas, J. R. *Inorg. Chem.* **1990**, *29*, 2123–2131.
- (38) Evans, C. E. B.; Ducharme, D.; Naklicki, M. L.; Crutchley, R. J. *Inorg. Chem.* **1995**, 1350–1354.
- (39) Richardson, D. E.; Taube, H. *Inorg. Chem.* **1981**, *20*, 1278–1285.
- (40) Creutz, C. *Prog. Inorg. Chem.* **1983**, *30*, 1.
- (41) Gu, P.; Garcia, Y.; Woike, T. *Coord. Chem. Rev.* **2001**, *219*, 839–879.
- (42) Sato, O. *Acc. Chem. Res.* **2003**, *36*, 692–700.
- (43) Rack, J. J.; Winkler, J. R.; Gray, H. B. *J. Am. Chem. Soc.* **2001**, *123*, 2432–2433.
- (44) Rack, J. *Coord. Chem. Rev.* **2009**, *253*, 78–85.
- (45) Division, C. S.; Sciences, B. E.; W-, C. *Inorg. Chem.* **1982**, *21*, 2542–2545.
- (46) Choudhuri, M. M. R.; Crutchley, R. J. *Inorg. Chem.* **2013**, *52*, 14404–14410.
- (47) King, A. W.; Jin, Y.; Engle, J. T.; Ziegler, C. J.; Rack, J. *Inorg. Chem.* **2013**, *52*, 2086–2093.
- (48) McClure, B. A.; Abrams, E. R.; Rack, J. J. *J. Am. Chem. Soc.* **2010**, *132*, 5428–5436.
- (49) McClure, B. A.; Mockus, N. V.; Butcher, D. P.; Lutterman, D. a; Turro, C.; Petersen, J. L.; Rack, J. J. *Inorg. Chem.* **2009**, *48*, 8084–8091.
- (50) Nelsen, S. F. *Chem. Eur. J.* **2000**, *6*, 581–588.
- (51) Mohommad Mahbubur Rahman Choudhuri. Redox Ambi-valence of Phenylcyanamide Ligands in Ruthenium Complexes, Carleton, 2013.
- (52) Calligaris, M.; Carugo, O.; Trieste, U.; Pauia, U. *Coord. Chem. Rev.* **1996**, *153*, 83–154.
- (53) Calligaris, M. *Coord. Chem. Rev.* **2004**, *248*, 351–375.
- (54) Cotton, F. A.; Dikarev, E. V; Petrukhina, M. A.; Stiriba, S. *Inorg. Chem.* **2000**, *39*, 1748–1754.

- (55) Tanase, T. *Chem. Commun.* **1996**, 2341–2342.
- (56) Yeung, C.-T.; Lee, W.-S.; Tsang, C.-S.; Yiu, S.-M.; Wong, W.-T.; Wong, W.-Y.; Kwong, H.-L. *Polyhedron* **2010**, *29*, 1497–1507.
- (57) Garas, A.; Craig, D. C.; Vagg, R. S.; Baker, A. T. *J. Coord. Chem.* **2000**, *50*, 79–88.
- (58) Smith, M. K.; Gibson, J. A.; Young, C. G.; Broomhead, J. A.; Junk, P. C.; Keene, F. R. *Eur. J. Inorg. Chem.* **2000**, *2000*, 1365–1370.
- (59) Sens, C.; Romero, I.; Llobet, A.; Sullivan, B. P.; Benet-buchholz, J. *Inorg. Chem.* **2003**, *42*, 2040–2048.
- (60) Mari Toyama, Shinobu Iwamatsu, Ken-ichi Inoue, and N. N. *Chem. Soc. Japan* **2010**, *83*, 1518–1527.